Universitat Autònoma de Barcelona

High-resolution guiding patterns for the directed self-assembly of block copolymers

Steven Gottlieb

High-resolution guiding patterns for the directed self-assembly of block copolymers

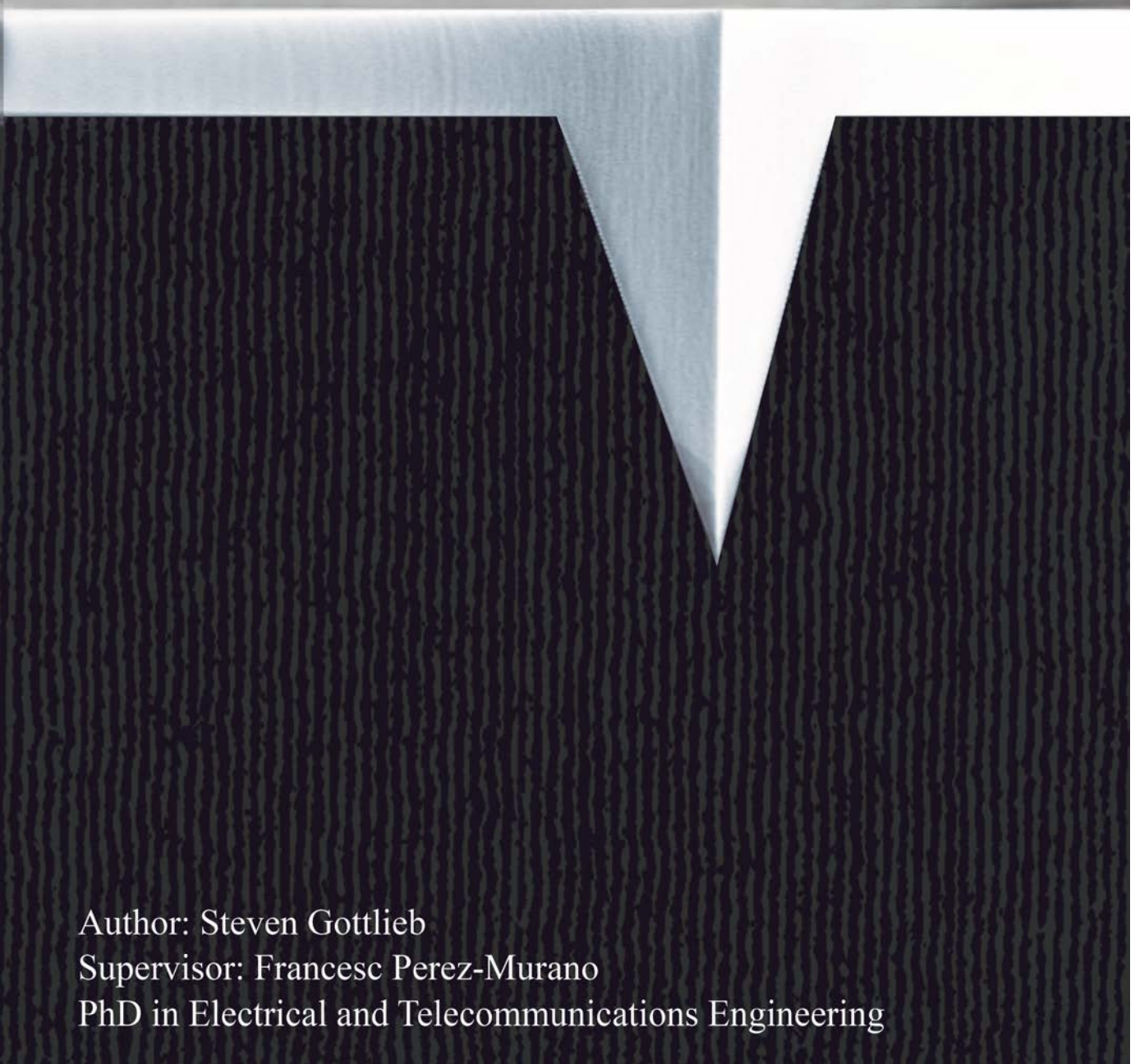

Author: Steven Gottlieb
Supervisor: Francesc Perez-Murano
PhD in Electrical and Telecommunications Engineering

High-resolution guiding patterns for the directed self-assembly of block copolymers

by

Steven Gottlieb

Dissertation

presented to the

Department of Electronic Engineering

of the

Autonomous University of Barcelona

in partial fulfillment of the requirements for the degree of

PhD in Electrical and Telecommunications Engineering

Director and tutor:

Prof. Francesc Perez-Murano

Institute of Microelectronics Barcelona (IMB-CNM, CSIC)

Cerdanyola del Vallès, 5 September 2018

(Updated 4 November 2018)

This is to certify that this thesis, entitled **"High-resolution guiding patterns for the directed self-assembly of block copolymers"**, has been written by Steven Gottlieb and is submitted to obtain the degree of Doctor of Philosophy in Electrical and Telecommunications Engineering under guidance and supervision of Prof. Dr. Francesc Perez-Murano, IMB-CNM (CSIC).

Cerdanyola del Vallès, 5th September 2018

Francesc Perez-Murano

Steven Gottlieb

"Every man's island, Jean Louise,
every man's watchman, is his conscience."

Harper Lee in *Go Set a Watchman*

Resume

The presented thesis entitled “High-resolution guiding patterns for the directed self-assembly of block copolymers” investigates strategies to introduce long-range order into block copolymer thin films for nanopatterning applications.

Structures defined by top-down lithography that enable the introduction of long-range order into an otherwise disordered thin film of block copolymers are referred to as guiding patterns. This thesis explores and develops different techniques that enable the fabrication of guiding patterns with a particular focus on methods capable of providing high-resolution and high-accuracy, because they are at the prospect of playing a crucial role in the directed self-assembly of very low-pitch block copolymer materials. We demonstrate the directed self-assembly of an 11.7 nm full-pitch *PS-b-PMMA* block copolymer with guiding patterns fabricated by means of five different top-down lithography techniques.

One strategy to fabricate guiding patterns consists in the generation of topographic structures, which is referred to as graphoepitaxy. In this case, we have used extreme-ultraviolet interference lithography to fabricate trenches with nanometer precision to study the self-assembly behavior of block copolymers under nanoconfinement with high accuracy. This system has allowed us to develop a free energy model to predict for which guiding pattern dimensions the defect-free directed self-assembly can be expected. Moreover, we have used electron beam lithography for the fabrication of sub-10 nm wide topographical guiding patterns and study the directed self-assembly of block copolymers in structures with feature sizes close to the material’s half-pitch.

Another strategy to fabricate guiding pattern consists of chemical surface modification to create areas that are selectively affine to one of the blocks. We have presented a novel approach based on thermal scanning probe lithography and adjust the patterning conditions for the fabrication of chemical guiding patterns with 10 nm line width. Due to the absence of the proximity and diffraction effects, thermal scanning probe lithography is ideal for the fabrication of dense high-resolution chemical patterns.

As a third strategy to align block copolymers, we use grain boundaries in block copolymer thin films as order-inducing surfaces. A surface modification is used to trap a grain of vertically oriented block copolymers between two grains of horizontally oriented block copolymer domains in a controlled manner. We call the developed technique “grain-boundary induced alignment”. To demonstrate its working principle we employ mechanical AFM and electron beam direct writing, and show the ordering of block copolymers on length scales of various hundreds of nanometers.

The presented thesis is complemented with the development of a probe-based imaging technique to study the thermal conductivity of polymer materials with sub-10 nm lateral

resolution. The dissipation of heat into a sample is determined at each measurement point by means of an electrical circuit that is integrated into the cantilever. We study the thermal conductivity of *PS-b-PMMA* block copolymers with different pitches and different orientations. This technique represents an advance in the investigation of polymeric surfaces due to its high resolution and good material sensitivity.

Resumen

La tesis titulada: “High-resolution guiding patterns for the directed self-assembly of block copolymers” investiga distintas estrategias para la introducción de orden de largo alcance en capas delgadas de copolímeros de bloque para aplicaciones de nano-estructuración de superficies.

Los elementos definidos por litografía top-down que permiten la introducción del orden de largo alcance en una desordenada capa delgada de copolímeros de bloque se conocen como patrón de guiado. Esta tesis explora las diferentes técnicas que permiten la fabricación de patrones de guiado y está particularmente enfocada en la fabricación de éstos en alta resolución y precisión, con la perspectiva de jugar un papel clave en el autoensamblaje dirigido de copolímeros de bloque de bajo periodo. Demostramos el autoensamblaje de un copolímero de bloque de *PS-b-PMMA* de 11.7 nm con patrones de guiado fabricados por cinco técnicas diferentes.

Una estrategia abordada se basa en la fabricación de patrones de guiado topográficos, lo que se conoce como graphoepitaxia. En particular, usamos litografía por interferencia en el ultravioleta extremo para fabricar zanjas con precisión nanométrica y estudiar el comportamiento de autoensamblaje de los copolímeros de bloque bajo nano-confinamiento. Este sistema nos permite el desarrollo de un modelo de energía libre para predecir, para que dimensiones de zanja esperamos un autoensamblaje dirigido libre de defectos. Además, utilizamos la litografía de haz de electrones para la fabricación de patrones de guiado topográficos menores de 10 nm para estudiar el autoensamblaje dirigido de copolímeros de bloque en estructuras con tamaño similar al tamaño de sus bloques.

Otra estrategia para la fabricación de patrones de guiado consiste en la modificación química de superficies para la creación de áreas selectivamente atractivas a uno de los bloques. Presentamos un nuevo método fundamentado en la litografía basada en la microscopía térmica de sondas y ajustamos las condiciones para la fabricación de patrones de guiado químicos con un ancho de línea de 10 nm. Debido a la ausencia de efectos de proximidad y de difracción, la litografía basada en sondas de escaneo térmico es ideal para la fabricación de patrones de guiado químicos densos y de alta resolución.

Como tercera estrategia para el alineamiento, usamos fronteras de grano en capas delgadas en copolimeros de bloque para inducir orden. Se usa la modificación química de la superficie para atrapar un grano de copolímeros de bloque orientado verticalmente entre dos granos orientados horizontalmente. Denominamos a esta técnica "alineamiento inducido por fronteras de granos". Para demostrar el principio de funcionamiento de esta

técnica, usamos la modificación mecánica mediante AFM y la escritura directa mediante e-beam.

La tesis presentada se complementa con el desarrollo de una técnica de obtención de imágenes basada en microscopía de sonda térmica que permite estudiar la conductividad térmica de polímeros con resolución lateral inferior a 10 nm. La disipación de calor en una muestra en cada punto se mide mediante un circuito eléctrico integrado en el fleje. Estudiamos la conductividad térmica de copolimeros en bloque autoensamblados en diferentes orientaciones y dimensiones. La técnica representa un avance en la investigación de superficies poliméricas debido a su alta resolución y la capacidad de distinguir entre materiales con alta sensibilidad.

Zusammenfassung

In der vorliegenden Arbeit mit dem Titel „High-resolution guiding pattners for the directed self-assembly of block copolymers" werden Techniken vorgestellt, die dazu dienen, Fernordnung in Block Kopolymer Dünnschichten zu induzieren.

Mittels top-down Litografie hergestellte Strukturen, mit dem Zweck Block Kopolymere zu ordnen, werden *guiding patterns* (Führungsstrukturen) genannt. Es werden verschiedene Techniken aufgezeigt, die die Herstellung von Führungsstrukturen ermöglichen. Bei der Auswahl dieser Techniken wurde ein besonderer Fokus darauf gelegt, dass diese dazu in der Lage sind, Produktionsprozess mit einer hohen Auflösung und einem größtmöglichen Maß an Exaktheit durchzuführen. Es wird erwartet, dass besonders exakte Führungsstrukturen zukünftig eine wichtige Rolle beim Induzieren von Fernordnung in Block Kopolymeren mit besonders geringer Strukturgröße einnehmen werden. In dieser Arbeit zeigen wir die gerichtete Selbstorganisation eines *PS-b-PMMA* Block Kopolymers mit einer Strukturweite von 11.7 nm induziert durch fünf verschiedenene Arten von Führungsstrukturen.

Eine Alternative, um Führungsstrukturen herzustellen besteht im Ausnutzen von topographischen Strukturen. Dieses Verfahren wird *graphoepitaxy* genannt. Wir haben Extrem-Ultraviolette Interferenz-Litografie verwendet, um Gräben mit einer Genauigkeit von wenigen Nanometern herzustellen, und die gerichtete Selbstorganisation von Block Kopolymeren in diesen mit größtmöglicher Genauigkeit zu untersuchen. Wir verwenden dieses System, um daraus ein Modell der freien Energie abzuleiten und vorhersagen zu können, in Gräben welcher Weite die gerichtete Selbstorganisation des untersuchten Materials defektfrei abläuft. Darüber hinaus stellen wir weniger als zehn Nanometer breite topographische Führungsstrukturen mittels Elektronenstrahllitografie her und untersuchen die Selbstorganisation von Block Kopolymeren in topographischen Elementen in der Grössenordenung ihrer eigenen Strukturweite.

Eine weitere Strategie zur Herstellung von Führungsstrukturen ist die chemische Oberflächenmodfikation, bei der Bereiche auf der Probeoberfläche kreiert werden, die vornehmlich von einem der beiden Blöcke benetzt werden. Wir präsentieren eine neue auf thermischer Rastersondenlitografie basierende Methode und passen deren Prozessparameter so an, dass wir chemische Führungsstrukturen mit 10 nm Linienbreite erfolgreich herstellen können. Thermische Rastersondenlithografie stellt eine sehr gute Alternative für die Herstellung chemischer Führungsstrukturen dar, weil bei ihr weder Beugungseffekte noch die Resisterwärmung durch Proximität einen limitierenden Einfluss haben.

Als eine dritte Strategie nutzen wir Korngrenzen in Block Kopolymer Dünnschichten, um Fernordnung in ihnen zu induzieren. Eine Oberflächenmanipulation dient dazu, ein Korn mit vertikal angeordneten Block Kopolymer Domänen zwischen zwei Körnern in horizontaler Ausrichtung in kontollierter Weise einzusperren. Wir nennen diese Methode „Korngrenzen-induzierte Ordnung“. Um die Wirksamkeit dieser Methode nachzuweisen, nutzen wir mechanische Rasterkraftmikroskopie und direktes Elektronenstrahlschreiben und zeigen somit, dass wir Fernordnung in Block Kopolymere auf einer Längenskala von bis zu mehreren hundert Nanometern induzieren können.

Die präsentierte Arbeit wird mit der Entwicklung einer Rastersonden-basierten Technik zum Messen von Wärmeleitfähigkeit in Polymermaterialien mit einer lateralen Auflösung besser als zehn Nanometern vervollständig. Die Menge der abgeleiteten Wärme von einer erhitzten Spitze in eine Probe an jedem Messpunkt wird durch das Auslesen eines direkt in die Spitze integrierten elektrischen Schaltkreises bestimmt. Wir untersuchen die Wärmeleitfähigkeit von *PS-b-PMMA* Block Kopolymeren in verschiedenen Orientierungen und mit verschiedenen Kettenlängen. Diese Technik trägt durch ihre hohe laterale Auflösung und die gute Materialempfindlichkeit zum Fortschritt auf dem Gebiet der Untersuchung von Polymeroberflächen bei.

Table of contents

Motivation and Scope

Motivation

The technological progress of mankind in post-industrial-revolution times is closely related to the ability to manufacture new and better goods at a fast pace. In particular, semiconductor manufacturing has been the backbone of the advance from mainframe computers occupying entire rooms to smartphones that easily fit in our pockets within only few decades time. The successful industrial use of anticipated technological revolutions, such as the Internet of Things (IoT), Artificial Intelligence (AI) and self-driving cars depend, among other factors, on improved manufacturing processes in semiconductor industry.

The miniaturization of transistors in microprocessors in the last fifty years has been closely accompanied and to some extend guided by a prediction made by Gordon Moore in 1965 [1], that has become famous under the name *"Moore's Law"*. Moore's Law states that the number of transistors per unit area in a commercial microprocessor has to double about every two years in order to maintain high volume manufacturing (HVM) in microelectronics industry profitable. Accomplishing Moore's Law has been the working horse for growth in the semiconductor industry for decades and it is at the prospect of also being it in the years to come.

Appropriate fabrication techniques for semiconductor manufacturing have to satisfy both technological and economical requisites. Accordingly, fabrication techniques in microelectronics HVM have to fulfill the market's request for higher performance microprocessors by providing improved resolution patterning at a low level of defectivity (see *figure 0.1*). Furthermore, a viable method to keep production costs low is to ensure a high fabrication throughput. Remarkably, Moore's law has been deliberately accomplished by the semiconductor industry for several decades [2].

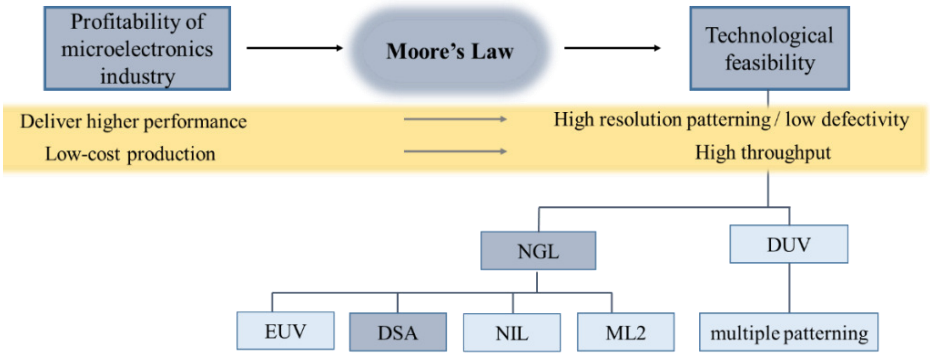

Figure 0.1: Relationship of Moore's law and the economic and technological prerequisites of patterning techniques.

High-resolution lithography techniques represent the essential step in semiconductor manufacturing to define small structures whose size ultimately defines the transistor dimensions. Currently used deep-ultraviolet immersion lithography is approaching its physical resolution limit. Pushing it towards today's resolution requirements (as dictated by Moore's Law) requires multiple patterning steps and comes therefore at increasingly high costs. For this reason, the development of innovative techniques with the capacity to enhance the resolution of lithography is one of the key points that needs to be addressed to ensure a solid base for technological progress in the forthcoming years.

A total of four next generation lithography (NGL) techniques has been identified by the International Technology Roadmap for Semiconductors (ITRS) to be capable of pushing the patterning resolution in semiconductor fabrication for the technology nodes to come. The directed self-assembly (DSA) of block copolymers (BCPs), together with extreme-ultraviolet lithography (EUV), nanoimprint lithography (NIL) and maskless techniques (ML2) forms part of this group. DSA is a hybrid patterning technique that combines bottom-up and top-down methods and is at the prospect to be used to fabricate structures far below 10 nm lateral size at an industrial scale. Besides research activities concerned with the development of novel high-χ block copolymer materials, an important part of this technology depends on the precise (commonly top-down) fabrication of structures capable of inducing long-range order in the material. These structures are referred to as guiding patterns.

Scope of the thesis

This thesis precisely aims at developing innovative guiding pattern fabrication methods to enable the directed self-assembly of block copolymers with high accuracy and consequently with a small number of defects. The scope of this thesis is schematically depicted in *figure 0.2.*

We expect that the currently available techniques are not sufficient to satisfy the needs of upcoming challenges in block copolymer lithography especially - but not exclusively - due to the significantly lower domain sizes in future high-χ block copolymer materials. For this reason, this thesis is particularly concerned with the development of high-resolution and high-precision guiding pattern fabrication techniques. In order to do so, we have collaborated with different international research groups with a particularly high profile in top-down lithography techniques.

The two most intensively studied approaches to direct the self-assembly of block copolymers are based on topographically defined features (referred to as graphoepitaxy) and chemical patterns (referred to as chemoepitaxy).

In a collaboration with the nanopatterning group at IBM Research Zurich, we have applied thermal scanning probe lithography to push the resolution of chemical guiding patterns down to 10 nm. Due to the capability of thermal scanning probe lithography to fabricate dense patterns at high resolution, the technique is perfectly fit for the fabrication of chemical guiding patterns for future small pitch block copolymers. Later on, the same nanopatterning tool has also been used to measure the thermal conductivity of block copolymers with a sub-10 nm resolution.

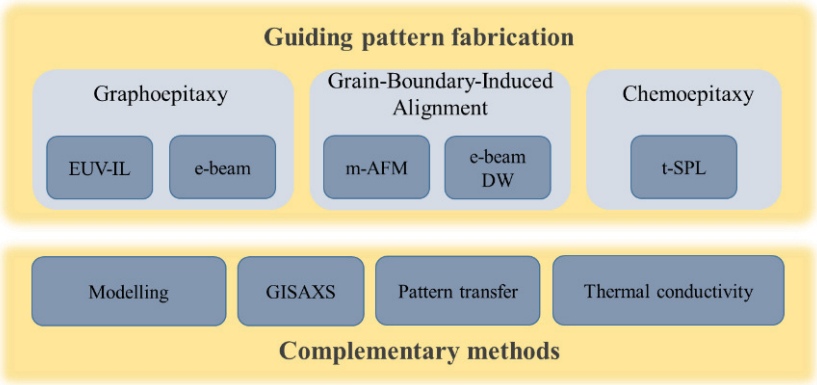

Figure 0.2: Sketch of the organization of this thesis. Departing from the core issue, namely the guiding pattern (GP) fabrication, different approaches are presented to direct the self-assembly of block copolymers. Based on these techniques, various further experiments have been conducted. These experiments represent the shell of the ellipse. The numbers in brackets behind the name of the techniques refer to the chapter, where reports on the respective experiments can be found.

We have fabricated sub-10 nm topographical guiding patterns using e-beam lithography in collaboration with the Laboratory of Micro and Nanotechnology (LMN) at the Paul Scherrer Institut (PSI), and identified an alternative self-assembly morphology of block copolymers when deposited in guiding patterns with feature dimensions close to the block copolymer half-pitch. Here, the analysis of the structures by GISAXS (executed at the P03 Micro- and Nanofocus X-ray Scattering beamline at Deutsches Elektronen-Synchrotron DESY) plays an important role to identify a new design rule for high-resolution topographical guiding patterns. In a second collaboration with the LMN at PSI, we use extreme-ultraviolet interference lithography (EUV-IL) to study the self-assembly of block copolymers in trenches whose width is controlled with nanometer precision. The

exceptionally high accuracy of the guiding pattern fabrication by EUV-IL has been used as the basis to improve current free energy models for confined block copolymers.

Apart from the use of chemical and topographical guiding patterns, we have developed an alternative approach referred to as grain-boundary-induced alignment, which represents an interesting alternative to direct the self-assembly of block copolymers with significantly lower resolution requirements in the lithography step. This work is especially concerned with the fundamental understanding of how grain boundaries may be used to fabricate arrays of parallel nanowires in block copolymer thin films. Pattern transfer techniques have been tested on block copolymer samples without long-range order, and afterwards been applied to structures aligned by grain boundaries.

Structure of the thesis

After an introduction to state-of-the-art lithography, to next generation lithography techniques, and in particular to block copolymer lithography and its underlying principles in *chapter 1*, we present the results of this PhD thesis in a total of four more chapters (*chapters 2 - 5*) and one annex *(annex 1).*

Chapter 2 is about the fabrication of topographical guiding patterns and therefore divided in two parts. Part 2*A* refers to the results using extreme ultraviolet interference lithography, while the experiments concerning sub-10 nm guiding patterns *via* e-beam are presented in part 2*B*.

The results of the experiments regarding the fabrication of chemical guiding patterns *via* thermal scanning probe lithography are presented in *chapter 3.*

In *chapter 4* the principle of grain-boundary-induced alignment is explained and applied to the alignment of block copolymers using mechanical AFM and e-beam direct writing.

The sub-10 nm resolution measurement of the thermal conductivity of block copolymers is presented in *chapter 5*.

Results of pattern transfer processes of block copolymer structures into silicon are presented in *annex 1.*

Contributions to projects

Research activities presented in this manuscript have been conducted in the framework of three different European projects. In the following section, we will briefly introduce

the scope of the projects and make reference to the results that have been obtained in the framework of the respective project.

NFFA (Nanoscience Foundries and Fine Analysis)

The aim of NFFA Europe is to establish a network of state-of-the-art research facilities that offer access to academia and industry. The access to the participating laboratories is organized in a free-of-charge transnational access concept that is based on proposals that undergo an evaluation process. Apart from offering transnational access, the project includes networking activities and original research activities conducted by the partners with the aim to solve current bottlenecks in nanoscience. These activities are organized in joint research activities (JRAs). The experiments presented in the *chapters 2A and 2B* (both graphoepitaxy), *chapter 4* (grain-boundary-induced alignment) and *annex 1* (pattern transfer) of this thesis are realized in the framework of the NFFA JRA2 "High precision manufacturing". Particularly, the experiments presented in *chapters 2A and 2B* are the outcome of a collaboration with the LMN at PSI. The GISAXS analysis discussed in *chapter* 2A *and 4* have been conducted in the course of beamtime facilitated via the NFFA transnational access framework in Petra III in Hamburg. The NFFA project receives funding from the EU's H2020 framework program for research and innovation under grant agreement no. 654360 starting 01/09/2015 ending 31/08/2019 [3,4].

SNM (Single Nanometer Manufacturing for Beyond CMOS Devices)

The objective of the SNM project to extend the limits of nano-device fabrication through the use of novel lithography techniques with sub-10 nm resolution. The approaches that have been considered within this project are scanning probe lithography (SPL) and focused electron beam induced processing (FEBIP).

The directed self-assembly of block copolymers presented in *chapter 3* (chemoepitaxy *via* t-SPL) is the result of a research stay at IBM Research Zurich conducted in the framework of SNM. The work presented in *chapter 5* (thermal conductivity of block copolymers) is not financially related to the funding received through the SNM project, but is the result of another visit at IBM Research Zurich after the end of the SNM funding period. SNM has been funded from the EU's FP7-ICT (Very advanced nanoelectronic components: design, engineering, technology and manufacturability) 01/01/2013 - 31/03/2017. The project ID is 318804 [5,6].

Ions4SET (Ion-irradiation-induced Si Nanodot Self-Assembly for Hybrid SET-CMOS Technology)

Ions4SET aims at developing low-energy-consumption single electron transistors that can be operated at room-temperature. Therefore, the fabrication of nanopillars is crucial. A part of the results presented in *annex 1* are the outcome of activities related to etch processes to enable the fabrication of nanopillars based on the directed self-assembly of

block copolymers. Ions4SET is funded by EU's H2020 framework program and forms part of the sub-section "Generic micro-and nano-electronic technologies". The funding period is 02/01/2016 – 31/01/2020 [7,8]. The grant agreement no. of Ions4SET is 688072.

References

[1] Moore G E 1965 Cramming more components onto integrated circuits *Electronics* **38** 114–7

[2] Waldrop M M 2016 More than Moore *Nature* **530** 144–7

[3] NFFA http://www.nffa.eu/ *Inf. retrieved 04/12/2017*

[4] NFFA http://cordis.europa.eu/project/rcn/198072_en.html *Inf. retrieved 04/12/2017*

[5] SNM https://www.tu-ilmenau.de/snm-project/ *Inf. retrieved 04/12/2017*

[6] SNM http://cordis.europa.eu/project/rcn/104931_de.html *Inf. retrieved 04/12/2017*

[7] IONS4SET http://www.ions4set.eu/ *Inf. retrieved 04/12/2017*

[8] IONS4SET http://cordis.europa.eu/project/rcn/199592_de.html *Inf. retrieved 04/12/2017*

Chapter 1:

Introduction

Table of contents: Chapter 1

1.1 Overview of lithography techniques

A large part of the advance in semiconductor manufacturing in the last decades has been due to the capacity to fabricate smaller and smaller features. The impressive improvement in manufacturing resolution has been made possible by major research activity in the field of photolithography.

1.1.1 Lithography principles

Photolithography is a widely-used method to replicate structures in a photo-sensitive resist with a resolution down to few tens of nanometers. To expose the resist selectively, a photo-mask with opaque and transparent regions is placed in the light path. In semiconductor manufacturing, high-resolution topographies composed of different materials may be fabricated by combining lithography with etching and deposition steps as depicted in *figure 1.1*.

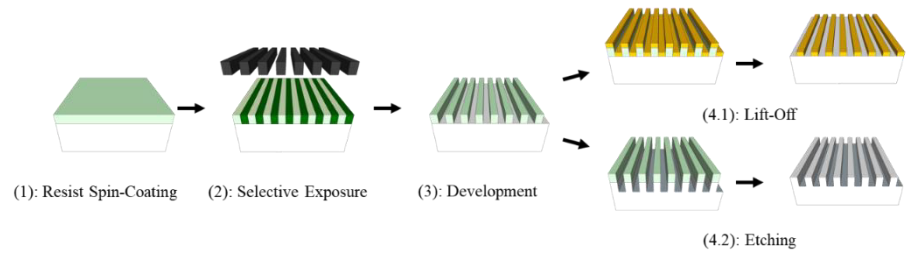

Figure 1.1: Typical work-flow of a lithography step with subsequent lift-off or etching step.

Depending on the resist material, the light exposure *(2)* may either induce cross-linking or lead to a degradation of the resist material in irradiated areas. Resists that cross-link upon exposure are referred to as negative tone resist, whereas resists that are degraded upon interaction with radiation are called positive tone resist. *Figure 1.1* shows the work-flow using a positive tone resist, where the exposed areas are modified and subsequently removed. For the development step *(3)*, the sample is rinsed in a liquid that dissolves either the exposed (positive resist) or the non-exposed (negative resist) part of the resist. As a result, the substrate is revealed in those areas, while the rest of the substrate is still covered by the resist layer. The exposed areas of the substrate may subsequently be subject to a (commonly metal-) deposition step. The thin layer that is deposited on top of the resist stripes is removed by a rinsing in a liquid that dissolves the resist layer *(4.1)*. Alternatively, the exposed substrate can be structured *(4.2)* by means of a (wet or dry) chemical etching step, while the resist protects the substrate from being attacked. In that way, material can be added and removed in lithographically defined areas.

The resolution of the lithography step *(2)* is the principal limiting factor of the size of the structures that can be fabricated by means of lithography. The capacity to print smaller and smaller features into the resist layer has been the driving force to sustain Moore's law for many years. Therefore, pushing (photo-)lithography towards an always higher resolution is of great interest for the advance in the field of computer technology, storage techniques and many more.

1.1.2 DUV lithography and resolution enhancing techniques

As for photolithography, one usually distinguishes between contact lithography, proximity lithography and projection lithography. The minimum printable resolution for contact lithography and proximity lithography is approximately $b_{con,prox} \approx \sqrt{\lambda * (d_{res} + d_{s/m})}$, where λ is the wavelength used during the exposure, d_{res} is the thickness of the resist and $d_{s/m}$ is the sample-mask distance.

Upon using complex optics, projection lithography is capable of reducing the size of the printed features with respect to their size on the mask. The minimum resolution in that case is given by $b_{proj} = \frac{k_1 * \lambda}{NA}$, where *NA* is the numerical aperture of the optical system and k_1 is a process and instrumental parameter. Projection lithography is currently used in HVM processes. Without further process improvements, the use of 193 nm wavelength light sources, as currently used in DUV lithography would, however, preclude the fabrication of sub-100 nm features. The key limiting factor is the light diffraction by the mask features.

Some of the strategies that have been considered to push the resolution of DUV lithography below this value include the enhancement of the numerical aperture *NA*, the reduction of k_1 and the reduction of the wavelength λ. The latter is discussed in the section about EUV lithography.

Particular measures that have been taken to reduce the value of k_1 are off-axis illumination, phase shifting masks and proximity corrections, which manipulate the wave direction, phase and amplitude [1].

Furthermore, an important step to enhance the resolution of DUV lithography has been the development of immersion lithography, which introduces a medium with a refractive index $n > 1$ (such as water) between the mask and the substrate. In this way, the effective wavelength inside the medium and thus diffraction mechanism are reduced [2]. Structure sizes below 30 nm have been demonstrated [3].

To fabricate even smaller feature sizes it is necessary to employ multiple (self-aligned) patterning steps (see *figure 1.2*). This is a combination of a common lithography step and a uniformly covering coating step *(1 / 2)*. After the etch-back of the coating *(3 / 4)* and

resist stripping *(5)*, the former side-walls of the deposited layer are used as template for the etching or lift-off step [4]. Three out of four major players in semiconductor manufacturing currently use self-aligned quadruple patterning (e.g. two consecutive self-aligned double patterning steps) in their 10-nm-node processes. Counterintuitively, the number in the node name does not refer to the half-pitch of the lithography step used to fabricate the features, but rather to the width of the electrical channel. The full-pitch of Intel's 2017 10-nm-node process is 34 nm [5].

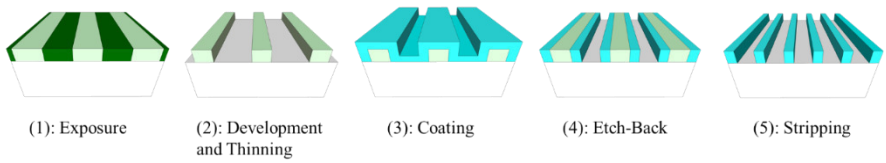

Figure 1.2: Self-aligned double-patterning work-flow.

1.1.3 Next generation lithography techniques

Despite of the very good results obtained by DUV immersion lithography and multiple patterning, the use of 193 nm-wavelength-light-based lithography for cutting-edge HVM is most likely come to an end in the next years, whether because the cost of multiple patterning is too high to maintain profitability or because multiple patterning makes the patterning process be too complex. Four techniques that are at the prospect of being capable of accomplishing Moore's Law in the next years are briefly introduced in this section [6].

1.1.3.1 Extreme ultraviolet lithography

Extreme-ultraviolet lithography follows the apparently obvious approach of reducing the wavelength in photolithography to 13.4 nm in order to improve the resolution of the technique. The development of this technique is, however, very challenging, because the need for reflective instead of transparent optics [7] and masks [8] leads to a substantially increased process complexity [9]. The major issues to be solved in EUV lithography are the currently insufficient light source power and line width roughness (LWR) in the printed features [10]. Recent progress has been sufficiently promising that Samsung has announced it will use extreme-ultraviolet lithography in its 7-nanometer node test production [11,12].

1.1.3.2 Maskless technologies

One generally refers to maskless lithography techniques as those that inherently lack the necessity of using a mask to define the shape of structures. Well-known examples for this group are probe-based techniques and e-beam lithography, which are usually serial techniques. Nanofabrication by means of serial techniques is usually several orders of

magnitude slower than by parallel techniques. A possible solution for this issue is given by the development of a parallel e-beam lithography system with up to 650,000 simultaneously exposing beams [13] to meet a throughput target of 5-10 wafers per hour [14]. Maskless techniques have been under discussion to represent a cost-effective alternative for the fabrication of mature nodes [7].

1.1.3.3 Nanoimprint lithography

The printing of features based on the plastic deformation of a patterning medium (polymer, resist, etc.) with nanometer resolution [15] is referred to as nanoimprint lithography (NIL) [16]. Most of the process variations of nanoimprint lithography can be grouped in either thermal NIL [17] or UV-NIL [18]. Unlike in photolithography where the printed features may be significantly smaller than the features fabricated on the mask, NIL is a contact method where the stamp actually touches the wafer and hence reproduces the mask features with a 1:1 size ratio. Therefore, the major challenges in NIL are both contamination and defects arising from the physical contact between stamp and sample, but also the difficulty to achieve an exact overlay [6].

1.1.3.4 Directed self-assembly of block copolymers

Block copolymers are two or more chemically different polymer chains covalently bonded together to one single macromolecule [19]. Driven by the repulsive force between chemically different molecules, the chains self-assemble in periodic structures in the size-range between few nanometers and few tens of nanometers. The periodic structures defined in that way can be used as bottom-up templates for nanofabrication processes that require very high resolution, such as bit patterned media for hard disk drives [20–22], finFETs [23] and contact holes [24]. Guiding patterns that are usually defined by top-down lithography are required to induce long-range order in the material [25–28]. One of the principal problems to date is the insufficiently low defect density for the integration of block copolymer lithography in HVM processes [6].

1.2 Block copolymer physics

As mentioned before, block copolymers are macromolecules that consist of two or more polymer chains connected by a covalent bond.

The chemically different blocks can either be merged in a linear or in a branched manner. In that sense, a great variety of different block copolymer structures may be thought of [19]. The most widely studied, and at the same time the block copolymer type that has been used in the experiments conducted in the course of this thesis, is the linear AB block copolymer, denoted A-*b*-B.

1.2.1 Molecular interaction and phase separation in block copolymers

The chemical difference between the two blocks *A* and *B* leads to a repulsive interaction between them and thus acts as driving force for microphase separation. This microphase separation process leads to the formation of periodic domains predominantly consisting of only one component *A* or *B*. This concept is sketched in *figure 1.3 a)*. The covalent bond between the chains inhibits their separation into two phases as we would observe it in a blend of two immiscible homopolymers. A quantification of the repulsive interaction between two blocks is given by the Flory-Huggins interaction parameter χ, based on works of Flory and Huggins [29,30]:

$$\chi_{AB} = {}^{Z}/_{k_B T}\left[\varepsilon_{AB} - {}^{1}/_{2}\left(\varepsilon_{AA}+\varepsilon_{BB}\right)\right], \qquad (0.1)$$

where Z is the number of nearest neighbours of a unit and ε_{ij} is the interaction energy between two monomers i and j. In this thesis, block copolymers based on *polystyrene* and *poly(methyl methacrylate)* (*PS-b-PMMA*) (see *figure 1.3 b)* for scheme of the molecule) have been employed. Their mutually repulsive forces are inherently low. As the interaction parameter scales inversely proportional to temperature, mixing of the two phases is enhanced as the temperature of the material increases. Experimental results [31,32] yield an interaction parameter for *PS-b-PMMA* as a function of the temperature T [K] of

$$\chi_{PS/PMMA} = 0.028 + \frac{3.9}{T\,[K]} \qquad (0.2)$$

This formula yields $\chi = 0.041$ at room temperature and 0.037 at 160 °C.

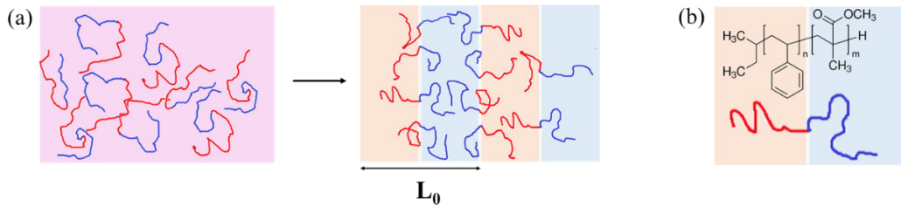

Figure 1.3: Influence of microphase separation in block copolymers on the molecular order of block copolymers. a): Difference between molecular order in a diblock copolymer in disordered state (left) and the microphase separated state (right), b): molecular architecture of a PS-b-PMMA polymer.

In general, the microphase separation in block copolymers is achieved in two different ways [33]. At one hand, thermal annealing can be used to heat the block copolymers above their glass transition temperature, enhance their chain mobility in this way [34] and to provoke microphase separation. Besides the substrate-block copolymer-interaction, an

important aspect for the success of the thermal annealing procedure is the difference in surface energy $\Delta\gamma$ between the two blocks. In case $\Delta\gamma$ is very large, the block copolymer will self-assemble such that it forms a wetting layer of the material with lower surface energy at the block-copolymer-air-interface. Interestingly, for *PS-b-PMMA* we find that $\Delta\gamma < 1$ % at 170 ºC [35], and that $\Delta\gamma$ decreases even more for larger temperatures [36]. This converts thermal annealing in an easy way to induce microphase separation in *PS-b-PMMA*. Solvent annealing, on the other hand, is the second strategy used to induce the self-assembly of block copolymers [37]. The selectivity of the solvent plays a role in the orientation of the block copolymer domains with respect to the substrate [38–40]. Solvent annealing has not been used in the course of the experiments presented in this thesis.

1.2.2 Phase diagram of AB diblock copolymers

The most studied block copolymer architecture is A-b-B block copolymers, which at the same time represents the only type of block copolymer that is used in this thesis. A-b-B block copolymers show a well-studied phase behaviour as a function of the product of the polymerization N and the Flory-Huggins interaction parameter χ, and the relative chain lengths of its components f_A and f_B [41,42]. The theoretical phase diagram of A-b-B diblock copolymers has been determined by the mean of Monte Carlo simulations in ref. [43] (*see figure 1.4 a)*).

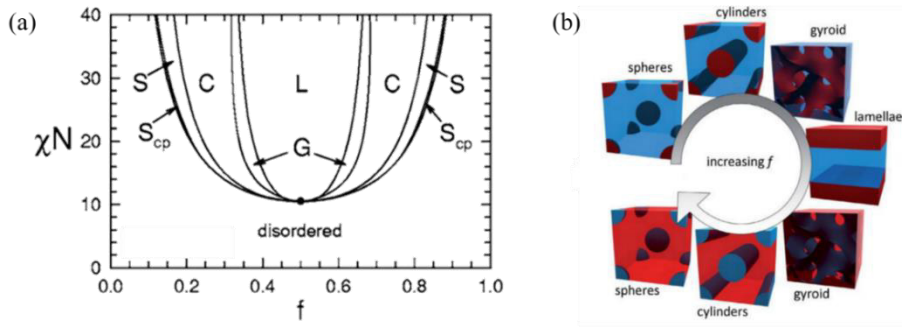

Figure 1.4: Phase behavior of diblock copolymers. a): Phase diagram of diblock copolymers according to Monte Carlo simulations taken from [43]. *The parameter f (x-axis) indicates the weight fraction of the chain of one of the blocks, for example PS. The term χN (y-axis) represents the product of the Flory-Huggins interaction parameter χ and the chain polymerization N. Lamellar self-assembly is expected in the areas denoted "L" and the cylindrical morphology in the areas denoted "C". Less frequently used morphologies are the spherical and the gyroid phase, denoted "S" and "G", respectively, b): sketches of the block copolymer self-assembly morphologies upon changing f. Illustration taken from ref.* [44].

A symmetric block copolymer self-assembles in lamellar structures (denoted *L*), whereas upon increasing the fraction of one polymer f_a, the material will first pass to a gyroid

morphology and then to cylinders in a matrix of material *B*, before it will finally self-assemble in spheres in a matrix of material *B* (see *figure 1.4 b)*). Microphase separation occurs for all materials that are above the order-disorder transition line in the phase diagram. The curve indicating the order-disorder transition in the phase diagram is parabolic with a global minimum at $\chi N = 10.4$ for perfectly symmetric block copolymers. Based on that, microphase separation for *PS-b-PMMA* block copolymers at 160 °C is a priori precluded for materials consisting of less than 251 monomers. The smallest reported full pitches obtained by *PS-b-PMMA* are 17.5 nm [45] and 19 nm [46], although the utility of sub-22 nm full pitch *PS-b-PMMA* materials for pattern transfer processes is questioned by some authors [47].

In a microphase separated block copolymer melt, its periodicity is determined by the minimization of the free energy of the block copolymer chains. A free energy model for block copolymers minimizes the sum of an entropic term and an enthalpic term. The entropic component of this minimization problem originates from the stretching of the chains, whereas the enthalpic component of the free energy takes the repulsive force between monomers into account.

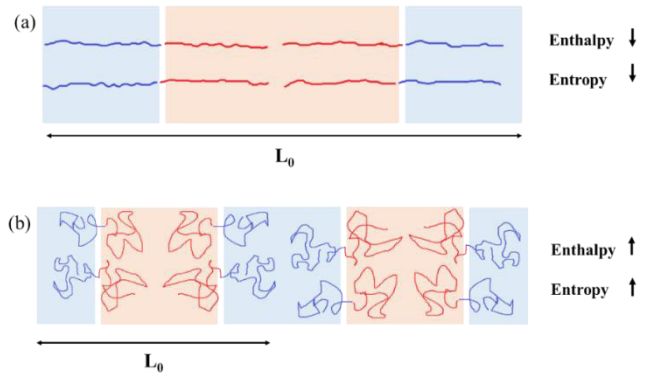

Figure 1.5: Correlation between chain stretching and periodicity of block copolymer lamellae. a): Large chain stretching reduces the entropy of the system, but also reduces the enthalpy because of a smaller number of A/B interfaces, b): Large chain compression increases both the enthalpy and the entropy of the system.

According to Ohta and Kawasaki [48], this yields a free energy per chain of

$$F = {}^{3}/_{8}\,\frac{kT}{Na^2}L^2 + \frac{2kTNa}{L}\sqrt{\frac{\chi}{6}}, \qquad (0.3)$$

where *a* is the monomer length, *N* is the chain polymerization and *L* is the period of the system.

Comparing this equation with the free energy equation according to Gibbs

$$G = H - TS, \qquad (0.4)$$

we state that the enthalpy of this system can be described as

$$H = \frac{2kTNa}{L}\sqrt{\frac{\chi}{6}}, \qquad (0.5)$$

while the other summand describes the entropy and corresponds to

$$S = -{}^{3}/_{8}\,\frac{k}{Na^2}L^2 \qquad (0.6)$$

As we can see from this equation, the free energy of the chain deformation term scales with the periodicity to the power of two, originating from a deformation similar to Hooke's law. The stretching of polymer chains contributes a decrease in entropy, because the stretched chains represent a more ordered system. In contrast to that, the enthalpic term scales with L^{-1} representing the decrease of the density of *A*-*B* interfaces as the layer spacing increases. This concept is graphically represented in *figure 1.5*.

The periodicity of the resulting features proportional both to the Flory-Huggins interaction parameter and the chain polymerization can be calculated by the minimization of the Ohta-Kawasaki formula with respect to the lamellar period L_0, so that $L_0 \propto \chi_{ab}^{1/6} \cdot N^{2/3}$ [49].

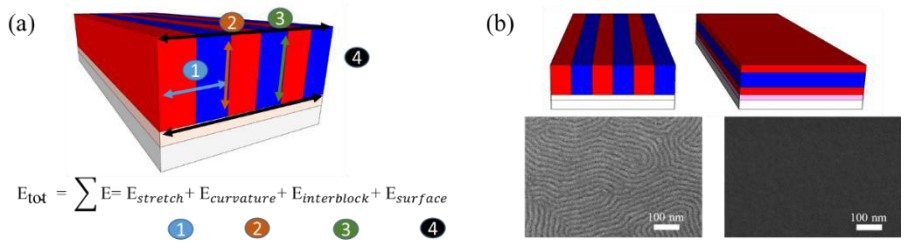

Figure 1.6: Free energy in block copolymer thin films. a): Sketch providing an overview of free energy contributions to the total free energy in a block copolymer thin film, b): difference between horizontally and vertically aligned block copolymer thin films as controlled by different block copolymer brushes.

1.2.3 Controlling surface interactions of block copolymers

For the energy minimization process in block copolymer thin films, in general four energy components are taken into account [50] (see *figure 1.6 a)*), namely *(1)* the energy stored in the chain stretching/compression other than the radius of gyration, *(2)* the A-B interface curvature, which contributes a negligibly low amount of free energy, *(3)* the interface free energy between the blocks *A* and *B* and *(4)* the surface energy at the block copolymer-air and the block copolymer-substrate interface. The self-assembly morphology is always

such that the sum of the four free energy components is minimal. For the self-assembly of thin films in unconfined states (e.g. on energetically homogenous, non-patterned substrates) the chain will stretch such that pattern pitch is L_0 and therefore minimize the chain extension and the total surface energy between the blocks *A* and *B*.

In case of lamellar block copolymers, the decision about whether the material self-assembles in vertical or horizontal lamellae (see *figure 1.6 b)*) depends on the interface energy between the substrate and the material the two blocks consist of Mansky et al. have found that the energy at the block copolymer-substrate interface of *PS-b-PMMA* can be managed by using *PS-r-PMMA* random copolymer brushes [35]. Random copolymer brushes whose monomer ratio is similar to the one of the block copolymer in question can be used as neutral brush layers and promote upright standing features. If one of the blocks, however, wets the random copolymer brush layer in an energetically clearly favorable manner, the block copolymer is assembled in horizontal features.

1.3 Enabling lithography with block copolymers

1.3.1 From self-assembly to directed self-assembly

Self-assembly is referred to as "the autonomous organization of components into patterns or structures without human intervention" [51] and is generally subdivided in static self-assembly and dynamic self-assembly. The microphase separation of block copolymers requires an initial energy input to the system, but is subsequently stable. For this reason, the self-assembly of block copolymers belongs to the category of static self-assembly. Another example for static self-assembly is the formation of molecular crystals.

A key condition that has to be fulfilled for self-assembly to take place is the ability of the building blocks to move with respect to one another [51]. For this reason, self-assembly mechanisms are usually observed in liquids or on smooth surfaces. Particularly, this is the reason why block copolymers are heated above their glass transition temperature in thermal annealing. Equilibrating forces are usually required to *(i)* avoid uncontrolled agglomeration when attractive forces are too high, and *(ii)* the decomposition of the material, when repulsive forces are too large. In case of block copolymers, the repulsive force is the chemical incompatibility described by the Flory-Huggins interaction parameter χ and the attractive force is due to the covalent bond between the two chains of a single molecule.

Lamellar phase A-b-B block copolymers naturally *self-assemble* in a patterns that are similar to line-and-space pattern required in semiconductor manufacturing. They exhibit, for example precisely defined line widths and periods. Self-assembled block copolymer patterns have already been identified as an excellent platform to develop applications in

nanotechnology [52]. The well-defined self-assembled block copolymer patterns are furthermore suitable to improve the resolution of lithography techniques, the line edge roughness and the line width roughness of current patterning techniques [27,53] and represent for this reason an excellent bottom-up technique for etch mask fabrication.

The absence of long-range order and placement accuracy precludes, however, any lithography application of the material in semiconductor industry in its as-spin-coated-and-annealed state. It is therefore crucial to induce long-range order in a controlled manner. This process is referred to as *"directing"* the self-assembly of block copolymers. In the following we will briefly refer to the most commonly used techniques to direct the self-assembly of block copolymers. The features that are fabricated by means of top-down lithography techniques to introduce long-range order in the thin film are called guiding patterns.

1.3.2 Graphoepitaxy

Directing the self-assembly of block copolymers with topographical patterns is referred to as graphoepitaxy. The technique aims at fabricating topographical structures in such a way that they energetically favor the block copolymer to self-assemble in the desired structures as depicted in *figure 1.7 a)*. The energetic advantage of ordered (e.g. directed) self-assembly in the created trenches with respect to a disordered self-assembly is in the preferential wetting of guiding pattern walls by one of the blocks. Furthermore, the creation of defects in block copolymers assembled in commensurate trenches imposes a free energy penalty, which converts the self-assembly in lamellae parallel to the guiding pattern walls into the minimum-free-energy state. The probability to from defects increases with the distance between the guiding pattern features because of the finite correlation length of the block copolymers far away from the order-inducing surface.

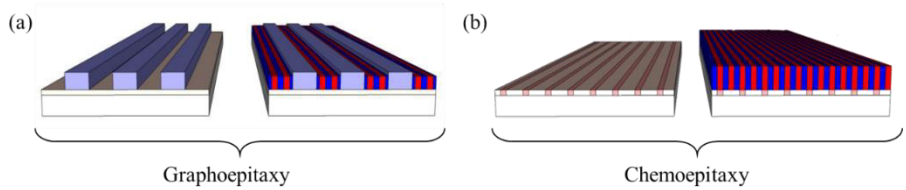

Figure 1.7: Scheme of most common techniques to direct the self-assembly of block copolymers. a): Graphoepitaxy, b): chemoepitaxy.

This principle has been successfully employed by a number of authors, as for example reported in refs. [54–58]. The best results are obtained when the width of the confining trench is exactly or close to an integer multiple of the natural pitch of the block copolymer [59]. A suitable guiding pattern design permits it, for example, to direct the self-assembly of block copolymers in device-oriented features [23] and induce long-range order in sub-

10 nm half-pitch block copolymers [60] and sub-5 nm half-pitch liquid crystals [61]. Another widely used approach to make use of cylindrical block copolymers are contact-hole shrink applications [24].

1.3.3 Chemoepitaxy

The chemoepitaxy approach relies on the introduction of chemical patterns into an underlying substrate (see *figure 1.7 b)*). In this thesis, we work with the chemical modification of grafted random copolymers [62–65]. Nevertheless, the orientation of block copolymers can also be successfully controlled by the use of self-assembled monolayers [66] and crosslinked polymer mats [67]. A lithographic process is applied to locally modify the interface free energy between the block copolymer and the underlayer in such a way, that certain regions are more attractive to one of the blocks than to the other. The most widely known approach to direct the self-assembly of block copolymers on chemically pre-patterned surfaces is the so called LiNe process [67], named after its inventors Liu and Nealey. There, a cross-linked polymer mat is patterned by means of photolithography and the space between the defined stripes is subsequently refilled with a neutral brush layer.

A common path to manipulate the surface free energy of a *PS-r-PMMA* random copolymer brush layer is the combination of a lithography step with its exposure to UV light [68] or an oxygen plasma [65]. A characteristic feature of the chemoepitaxy approach is that the guiding pattern must have a pitch close to η-times larger than the natural pitch of the block copolymer. The factor η is an integer referred to as density multiplication factor of the guiding pattern. The critical dimension of the guiding pattern features has to correspond to the half-pitch of the block copolymer [69] or 1.5 times the block copolymer pitch [63].

1.3.4 Other techniques

Long-range order has also been induced into cylindrical block copolymers by means of an electric field [70]. The orientation of self-assembled block copolymer cylinders in thin films takes place perpendicular to the electric field direction [71]. The self-assembly of cylindrical block copolymers has also been directed by the use of minimal topographic patterns [72,73]. A third interesting alternative alignment technique has been developed in the course of this thesis and uses the energy minimization of block copolymer thin films in grain boundaries. The underlying theoretic principles have been developed by Gido et al. [74–77] and Duque et al. [78].

1.4 References

[1] Schellenberg F M 2005 A History of Resolution Enhancement Technology *Opt.*

Rev. **12** 83–9

[2] Sanders D P 2010 Advances in Patterning Materials for 193 nm Immersion Lithography *Chem. Rev.* **110** 321–60

[3] Totzeck M, Göhnermeier A, Totzeck M, Ulrich W and Göhnermeier A 2007 Pushing deep ultraviolet lithography to its limits *Nat. Photonics* **1** 629–31

[4] Nakayama K, Kodama C, Kotani T, Nojima S, Mimotogi S and Miyamoto S 2017 Self-asligned double and quadruple patterning layout principle *SPIE Proc.* **8327** 83270V1-9

[5] Auth C and et al. 2018 A 10nm high performance and low-power CMOS technology featuring 3rdgeneration FinFET transistors, Self-Aligned Quad Patterning, contact over active gate and cobalt local interconnects *Tech. Dig. - Int. Electron Devices Meet. IEDM* 29.1.1-29.1.4

[6] Neisser M and Wurm S 2015 ITRS lithography roadmap: 2015 challenges *Adv. Opt. Technol.* **4** 235–240

[7] Fay A, Thiam N A, Cordini M-L, Servin I, Constancias C, Lattard L and Pain L 2015 “Fast” and “thick” e-beam resists exposed with multi-beam tool at 5 keV for implants and mature nodes: experimental and simulated model study *Proc. SPIE* **9423** 94231Q–1–15

[8] Jonckheere R 2017 EUV mask defectivity – a process of increasing control toward HVM *Adv. Opt. Technol.* **6** 203–20

[9] Mochi I, Helfenstein P, Mohacsi I, Rajeev R, Kazazis D, Yoshitake S and Ekinci Y 2017 RESCAN: an actinic lensless microscope for defect inspection of EUV reticles *J. Micro/Nanolithography, MEMS, MOEMS* **16** 041003

[10] Stokes H, Harumoto M, Tanaka Y, Kaneyama K, Pieczulewski C and Asai M 2017 EUV process improvement with novel litho track hardware *Proc. SPIE* **10143** 101431Z–1–5

[11] N/A 2018 https://news.samsung.com/global/samsung-electronics-announces-second-quarter-2018-results *Samsung Electron. Announc. Second Quart. 2018 Results*

[12] Jeong W and et al. 2018 True 7nm Platform Technology Featuring Smallest FinFET and Smallest SRAM Cell by EUV, Special Constructs and 3rd Generation Single Diffusion Break *2018 Symposia on VLSI Technology and Circuits, Honolulu, USA*

[13] Servin I, Thiam N A, Pimenta-Barros P, Pourteau M-L, Mebiene A-P, Jussot J, Pradelles J, Essomba P, Lattard L, Brandt P and Wieland M 2015 Ready for multi-beam exposure at 5kV on MAPPER tool: lithographic and process integration performances of advanced resists/stack *Proc. SPIE* **9423** 94231C–1–12

[14] Servin I, Pourteau M, Pradelles J, Essomba P, Lattard L, Brandt P and Wieland

M 2017 Progress and process improvements for multiple electron-beam direct write *Jpn. J. Appl. Phys.* **56** 06GC03-1-6

[15] Chou S Y and Krauss P R 1997 Imprint lithography with sub-10 nm feature size and high throughput *Microelectron. Eng.* **35** 237–40

[16] Schift H 2008 Nanoimprint lithography: An old story in modern times? A review *J. Vac. Sci. Technol. B Microelectron. Nanom. Struct.* **26** 458

[17] Chou S Y, Krauss P R and Renstrom P J 1996 Imprint Lithography with 25-Nanometer Resolution *Science.* **272** 85–7

[18] Haisma J, Herheijen M, van den Heuvel K and van den Berg J 1996 Mold-assisted nanolithography: A process for reliable pattern replication *J. Vac. Sci. Technol. B* **14** 4124–8

[19] Bates F S and Fredrickson G H 1999 Block copolymers-designer soft materials *Phys. Today* **52** 32–8

[20] Yang X, Xiao S, Hu W, Hwu J, Van De Veerdonk R, Wago K, Lee K and Kuo D 2014 Integration of nanoimprint lithography with block copolymer directed self-assembly for fabrication of a sub-20 nm template for bit-patterned media *Nanotechnology* **25** 1–11

[21] Ruiz R, Dobisz E and Albrecht T R 2011 Rectangular Patterns Using Block Copolymer Directed Assembly for High Bit Aspect Ratio Patterned Media *ACS Nano* **5** 79–84

[22] Griffiths R A, Williams A, Oakland C, Roberts J, Vijayaraghavan A and Thomson T 2013 Directed self-assembly of block copolymers for use in bit patterned media fabrication *J. Phys. D. Appl. Phys.* **46** 1–29

[23] Tsai H, Pitera J W, Miyazoe H, Bangsaruntip S, Engelmann S U, Liu C C, Cheng J Y, Bucchignano J J, Klaus D P, Joseph E A, Sanders D P, Colburn M E and Guillorn M A 2014 Two-dimensional pattern formation using graphoepitaxy of PS-b-PMMA block copolymers for advanced FinFET device and circuit fabrication *ACS Nano* **8** 5227–32

[24] Yi H, Bao X Y, Tiberio R and Wong H S P 2015 A general design strategy for block copolymer directed self-assembly patterning of integrated circuits contact holes using an alphabet approach *Nano Lett.* **15** 805–12

[25] Garner G, Williamson L, Seidel R, Rincon Delgadillo P, Hur S-M, Gronheid R, Nealey P F and de Pablo J J 2015 The effects of geometry and chemistry of nanopatterned substrates on the directed self-assembly of block-copolymer melts *Proc. SPIE* **9423** 94231K–1–9

[26] Claveau G, Hazart J, Posseme N, Chevalier X, Claveau G, Quemere P, Argoud M, Hazart J, Barros P P, Sarrazin A, Posseme N, Tiron R, Chevalier X, Nicolet C and Navarro C 2016 Surface affinity role in graphoepitaxy of lamellar block copolymers *J. Micro/Nanolithography, MEMS, MOEMS* **15** 031604-1–11

[27] Cheng J Y, Rettner C T, Sanders D P, Kim H-C and Hinsberg D 2008 Dense Self-Assembly on Sparse Chemical Patterns: Rectifying and Multiplying Lithographic Patterns Using Block Copolymers *Adv. Mater.* **20** 3155–8

[28] Blachut G, Sirard S M, Maher M J, Asano Y, Someya Y, Lane A P, Durand W J, Bates C M, Dinhobl A M, Gronheid R, Hymes D, Ellison C J and Willson C G 2016 A Hybrid Chemo-/Grapho-Epitaxial Alignment Strategy for Defect Reduction in Sub-10 nm Directed Self-Assembly of Silicon-Containing Block Copolymers *Chem. Mater.* **28** 8951–61

[29] Flory P J 1942 Thermodynamics of High Polymer Solutions *J. Chem. Phys* **10** 51–61

[30] Huggins M L 1941 Solutions of Long Chain Compounds *J. Chem. Phys.* **9** 440

[31] Russell T P, Hjelm R P and Seeger P A 1990 Temperature Dependence of the Interaction Parameter of Polystyrene and Poly (methyl methacrylate) *Macromolecules* **23** 890–3

[32] Freed K F and Dudowicz J 1992 On the large entropic contribution to the effective interaction parameter of polystyrene – poly (methyl methacrylate) diblock copolymer systems On the large entropic contribution to the effective interaction parameter of polystyrene-poly (methyl methac *J. Chem. Phys.* **97** 2105–9

[33] Ji S, Wan L, Liu C and Nealey P F 2016 Directed self-assembly of block copolymers on chemical patterns : A platform for nanofabrication *Prog. Polym. Sci.* **54**–**55** 76–127

[34] Solak H H, Edwards E W, Stoykovich M P, Mu M, Pablo J J D E and Nealey P F 2005 Mechanism and Kinetics of Ordering in Diblock Copolymer Thin Films on Chemically Nanopatterned Substrates *J. Polym. Sci. Part B* **43** 3444–59

[35] Mansky P, Liu Y, Huang E, Russell T P and Hawker C 1997 Controlling Polymer-Surface Interactions with Random Copolymer Brushes *Science.* **275** 1458–60

[36] Mansky P, Russell T P, Hawker C J, Mays J, Cook D C and Satija S K 1997 Interfacial segregation in disordered block copolymers: Effect of tunable surface potentials *Phys. Rev. Lett.* **79** 237–40

[37] Jung Y S and Ross C A 2009 Solvent-vapor-induced tunability of self-assembled block copolymer patterns *Adv. Mater.* **21** 2540–5

[38] Bosworth J K, Paik M Y, Ruiz R, Schwartz Ḱ E L, Huang J Q, Ko A W, Smilgies D, Black C T and Ober C K 2008 Control of Self-Assembly of Lithographically Patternable Block Copolymer Films *ASC Nano* **2** 1396–402

[39] Bang J, Kim B J, Stein G E, Russell T P, Li X, Wang J, Kramer E J and Hawker C J 2007 Effect of humidity on the ordering of PEO-based copolymer thin films *Macromolecules* **40** 7019–25

[40] Guo R, Huang H, Chen Y, Gong Y, Du B and He T 2008 Effect of the nature of annealing solvent on the morphology of diblock copolymer blend thin films *Macromolecules* **41** 890–900

[41] Bates F S and Fredrickson G H 1990 Block Copolymer Thermodynamics: Theory and Experiment *Annu. Rev. Phys. Chem.* **41** 525–57

[42] Leibler L 1980 Theory of microphase separation in block copolymers *Macromolecules* **13** 1602–17

[43] Matsen M W, Griffiths G H, Wickham R A and Vassiliev O N 2006 Monte Carlo phase diagram for diblock copolymer melts *J. Chem. Phys.* **124** 024904-1–9

[44] Tseng Y C and Darling S B 2010 Block copolymer nanostructures for technology *Polymers (Basel).* **2** 470–89

[45] Anastasiadis S H, Russell T P, Satija S K and Majkrzak C F 1989 Neutron Reflectivity Studies of the Surface-Induced Ordering of Diblock Copolymer Films *Phys. Rev. Lett.* **62** 1852–5

[46] Chevalier X, Nicolet C, Tiron R, Gharbi A, Argoud M, Pradelles J, Delalande M, Cunge G, Fleury G, Hadziioannou G and Navarro C 2013 Scaling-down lithographic dimensions with block-copolymer materials: 10-nm-sized features with poly(styrene)- *block* -poly(methylmethacrylate) *J. Micro/Nanolithography, MEMS, MOEMS* **12** 031102

[47] Wan L, Ruiz R, Gao H, Patel K C and Albrecht T R 2015 The Limits of Lamellae-Forming PS-b-PMMA Block Copolymers for Lithography *ASC Nano* **9** 7506–14

[48] Ohta T and Kawasaki K 1986 Equilibirum Morphology of Block Copolymer Melts *Macromolecules* **19** 2621–32

[49] Bates F S and Fredrickson G H 1999 Block Copolymers—Designer Soft Materials *Phys. Today* **52** 32–8

[50] Wang Z-G G 1994 Response and instabilities of the lamellar phase of diblock copolymers under uniaxial stress *J. Chem. Phys.* **100** 2298–309

[51] Whitesides G M and Grzybowski B 2002 Self-Assembly at All Scales *Science.* **295** 2418–21

[52] Park C, Yoon J and Thomas E L 2003 Enabling nanotechnology with self assembled block copolymer patterns *Polymer (Guildf).* **44** 6725–60

[53] Stoykovich M P, Daoulas K C, Müller M, Kang H, De Pablo J J and Nealey P F 2010 Remediation of line edge roughness in chemical nanopatterns bythe directed assembly of overlying block copolymer films *Macromolecules* **43** 2334–42

[54] Yoshida A, Yoshimoto K and Ohshima M 2016 Effect of wall potential on morphology of symmetric diblock copolymers in nanotrench *Jpn. J. Appl. Phys.* **55** 06GE01-1-6

[55] Chen W, Luo J, Shi P, Li C, He X, Hong P, Li J and Zhao C 2014 Self-assembling morphologies of symmetrical PS b-PMMA in different sized confining grooves *RSC Adv.* **4** 50393–400

[56] Han B E, Kang H, Liu C, Nealey P F and Gopalan P 2010 Graphoepitaxial Assembly of Symmetric Block Copolymers on Weakly Preferential Substrates *Adv. Mater.* **22** 4325–9

[57] Borah D, Rassapa S, Shaw M T, Hobbs R G, Petkov N, Schmidt M, Holmes J D and Morris M 2013 Directed self-assembly of PS-b-PMMA block copolymer using HSQ lines for translational alignment *J. Mater. Chem. C* **1** 1192–6

[58] Ilievski F and Ross C A 2010 Graphoepitaxy of block copolymers using selectively removable templates *J. Vac. Sci. Technol. A Vacuum, Surfaces, Film.* **28** 42–4

[59] Walton D, Kellogg G and Mayes A 1994 A free energy model for confined diblock copolymers *Macromolecules* **27** 6225–8

[60] Borah D, Shaw M T, Holmes J D and Morris M A 2013 Sub-10 nm Feature Size PS - b - PDMS Block Copolymer Structures Fabricated by a Microwave-Assisted Solvothermal Process *ACS Appl. Mater. Interfaces* **5** 2004–12

[61] Nickmans K, Murphy J N, Waal B De, Leclère P, Doise J, Gronheid R, Broer D J and Schenning A P H J 2016 Sub-5 nm Patterning by Directed Self-Assembly of Oligo (Dimethylsiloxane) Liquid Crystal Thin Films *Adv. Mater.* **28** 10068–72

[62] Gottlieb S, Lorenzoni M, Evangelio L, Fernández-Regúlez M, Ryu Y K, Rawlings C, Spieser M, Knoll A W and Perez-Murano F 2017 Thermal scanning probe lithography for the directed self-assembly of block copolymers *Nanotechnology* **28** 1–9

[63] Evangelio L, Fernández-Regúlez M, Borrisé X, Lorenzoni M, Fraxedas J and Perez-Murano F 2015 Creation of guiding patterns for directed self-assembly of block copolymers by resistless direct e-beam exposure *J. Micro/Nanolith. MEMS MOEMS.* **14** 033511-1-033511-6

[64] Fernández-Regúlez M, Evangelio L, Lorenzoni M, Fraxedas J and Perez-Murano F 2014 Sub-10 nm resistless nanolithography for directed self-Assembly of block copolymers *ACS Appl. Mater. Interfaces* **6** 21596–602

[65] Ruiz R, Kang H, Detcheverry F A, Dobisz E, Kercher D S, Albrecht T R, de Pablo J J and Nealey P F 2008 Density Multiplication and Improved Lithography by Directed Block Copolymer Assembly *Science.* **321** 936–9

[66] Kim S, Solak H, Stoykovich M, Ferrier N, de Pablo J and Nealey P 2003 Epitaxial self-assembly of block copolymers on lithographically defined nanopatterned substrates *Nature* **424** 411–4

[67] Liu C C, Han E, Onses M S, Thode C J, Ji S, Gopalan P and Nealey P F 2011

Fabrication of lithographically defined chemically patterned polymer brushes and mats *Macromolecules* **44** 1876–85

[68] Evangelio Araujo L 2017 *Directed self-assembly of block copolymers on chemically nano-patterned surfaces (PhD thesis)* (Universitat Autònoma de Barcelona)

[69] Garner G, Williamson L, Seidel R, Rincon Delgadillo P, Hur S-M, Gronheid R, Nealey P F and de Pablo J J 2015 The effects of geometry and chemistry of nanopatterned substrates on the directed self-assembly of block-copolymer melts *Proc. SPIE* **9423K** 1–9

[70] Xu T, Zvelindovsky A V, Sevink G J A, Lyakhova K S, Jinnai H and Russell T P 2005 Electric Field Alignment of Asymmetric Diblock Copolymer Thin Films *Macromoelcules* **38** 10788–98

[71] Elhadj S, Woody J W, Niu V S and Saraf R F 2003 Orientation of self-assembled block copolymer cylinders perpendicular to electric field in mesoscale film *Appl. Phys. Lett.* **82** 871–3

[72] Choi J, Huh J, Carter K R and Russell T P 2016 Directed Self-Assembly of Block Copolymer Thin Films Using Minimal Topographic Patterns *ACS Nano* **10** 7915–25

[73] Choi J, Gunkel I, Li Y, Sun Z, Liu F, Kim H, Carter K R and Russell T P 2017 Macroscopically ordered hexagonal arrays by directed self-assembly of block copolymers with minimal topographic patterns *Nanoscale* **9** 14888–96

[74] Gido S P and Thomas E L 1997 Lamellar Diblock Copolymer Grain Boundary Morphology. 3. Helicoid Section Twist Boundary Energy *Macromolecules* **30** 3739–46

[75] Gido S P and Thomas E L 1994 Lamellar Diblock Copolymer Grain Boundary Morphology. 2. Scherk Twist Boundary Energy Calculations *Macromolecules* **27** 849–61

[76] Gido S P and Thomas E L 1994 Lamellar Diblock Copolymer Grain Boundary Morphology. 4. Tilt Boundaries *Macromolecules* **27** 6137–44

[77] Gido S P, Gunther J, Thomas E L and Hoffman D 1993 Lamellar diblock copolymer grain boundary morphology. 1. Twist boundary characterization *Macromolecules* **26** 4506–20

[78] Duque D, Katsov K and Schick M 2002 Theory of T junctions and symmetric tilt grain boundaries in pure and mixed polymer systems *J. Chem. Phys.* **117** 10315–20

Chapter 2A:

High-accuracy topographical guiding patterns by EUV-IL to study the nanoconfinement of block copolymers

Abstract:

We study the nanoconfinement of block copolymers in topographical guiding patterns and extend current free energy models by estimating the free energy of a defect-loaded state. The defect-loaded state appears as a consequence of the mismatch between the guiding pattern separation and the block copolymer natural pitch. We determine the relation between trench width and the emergence of defects with nanometer precision. This allows us to us to predict the process window for guiding pattern fabrication to achieve a low level of defects. Extreme-ultraviolet interference lithography (EUV-IL) is used to manufacture topographical guiding patterns that direct the self-assembly of an 11.7 nm half-pitch *PS-b-PMMA* block copolymer. High-accuracy silicon oxide-like patterns with trench widths ranging from 68 nm to 117 nm are fabricated by exposing a *hydrogen silsesquioxane* (*HSQ*) resist layer with EUV light at different exposure doses. The excellent line width roughness of the fabricated guiding patterns enables us to minimize the influence of defect formation in the self-assembly due to guiding pattern inaccuracies and to model the emergence of the formation of defects due to guiding pattern incommensurability.

Table of contents: Chapter 2A

2A.1 Introduction

Recent developments in the field of high-volume manufacturing forecast that extreme-ultraviolet (EUV) lithography will play a significant role in semiconductor manufacturing because of its capacity to fabricate features with high throughput and high resolution [1]. EUV interference lithography (EUV-IL) has emerged as a promising nanolithography technique for research, which is inherently capable of producing single digit (sub-10 nm) periodic and quasiperiodic dense nanostructures (lines/spaces, dots, holes etc.), with record resolutions down to 6 nm [2]. Transmission diffraction gratings on thin Si_3N_4 membranes are used to create interference of mutually coherent beams, which, in turn, results in the desired interference patterns recorded in a photosensitive material, as schematically shown in *figure 2A.1*. Depending on the number and configuration of the transmission gratings, several periodic structures can be produced, such as lines and spaces, square and hexagonal arrays of dots and holes, Kagome lattices etc. [3]. The scheme in *figure 2A.1 a)* shows a two-grating configuration, such as the one used in this work that is used to create lines and spaces. The incident beam gets diffracted by each one of the two gratings whose angles of diffraction are given by:

$$sin\theta_m = \frac{m\lambda}{P_g} \qquad (2A.1),$$

where m is the order of diffraction, λ is the wavelength of the light, and P_g is the grating periodicity (pitch). When the illumination of the two gratings is identical, the resulting interference pattern has a periodicity given by:

$$P = \frac{\lambda}{2\sin\frac{\theta}{2}} \qquad (2A.2),$$

where $\theta = 2\theta_m$ is the angle between the two diffracted beams in the case of the two-grating mask. Combining the two equations and taking $m = 1$ for first-order diffraction one finally obtains:

$$P = \frac{P_g}{2} \qquad (2A.3).$$

In this case, the pitch on the resist is half of the pitch of the transmission gratings, enabling frequency multiplication by a factor of 2. The EUV-IL setup used throughout our experiments is located at the XIL-II beamline of the Swiss light source (SLS) synchrotron of the Paul Scherrer Institut in Switzerland. The EUV radiation comes from an undulator (insertion device) tuned at a wavelength of 13.5 nm, which is the wavelength for next-generation EUV lithography.

One important bottleneck for the implementation of EUV lithography in high-volume manufacturing is the still large line edge roughness (LER) and line width roughness

(LWR) of the features at high resolution, which improves when the technique is combined with DSA [4]. Moreover, achieving sub-10 nm half-pitches with EUV lithography will be challenging. On the other hand, the weak point of DSA is the still too large defect density, which is potentially attributed to an insufficient guiding pattern quality [5]. The fabrication of guiding patterns for the directed self-assembly of block copolymers far below 10 nm full-pitch will, therefore, require techniques with high resolution, high precision and at low LER/LWR [5] for DSA to meet the defect density required of semiconductor manufacturing requirements. Here, we investigate the use of topographical guiding patterns fabricated by EUV-IL to guide the self-assembly of block copolymers and the potential to obtain DSA patterns with a low density of defects.

The use of EUV-IL for the creation of guiding patterns is highly adequate. The aerial image formed by IL is a sinusoidal function, independent of the pitch [3]. Line-edge roughness or point defects in the diffraction gratings merely generate incoherent scattering which can add a few percent background to the aerial image. The exact structure of the diffraction gratings defines the diffraction efficiency but has no influence on the aerial image. Compared to e-beam lithography, EUV-IL therefore enables the fabrication of denser and smoother nanostructures.

EUV-IL has been used before for the fabrication of chemical guiding patterns to direct the self-assembly of block copolymers [6,7], but to our best knowledge there are no works combining graphoepitaxy and EUV-IL. Other authors have presented graphoepitaxial guiding patterns defined by an EUV micro-exposure tool [8] using a positive tone resist to analyze the behavior of *PS-b-PLA* under confinement [9], however with relatively low guiding pattern accuracy and a significant guiding pattern LWR. DSA has moreover been used to shrink holes defined by EUV [10,11]. A very good candidate for the fabrication of smooth guiding patterns is *hydrogen silsesquioxane* (*HSQ)* [12], that has recently been used to direct the self-assembly of block copolymers in combination with e-beam lithography [13,14]. *HSQ* is particularly interesting, because the cross-linking of *HSQ* induced by EUV-IL has been demonstrated to provide high resolution patterns with excellent LWR [15]. The LWR of the guiding pattern features represents an important parameter in the generation of defects in the directed self-assembly of block copolymers. This has been shown both in theoretical [16] and in experimental [5,17] works. In order to analyze the behavior of block copolymers in topographical guiding patterns with highest-possible accuracy and free of effects due to guiding pattern roughness, we chose EUV-IL as a guiding pattern fabrication technique.

We present a complete study of the directed self-assembly of an 11.7 nm half-pitch *PS-b-PMMA* block copolymer in trenches fabricated by the selective exposure of *HSQ* with EUV-IL. Extensive optimization of the process is carried out to achieve that block

copolymers self-assemble in structures relevant for the fabrication of finFETs [18,19]. We conducted an in-depth study of the effect of the trench width on the emergence of defects and tested different approaches of neutral *PS-r-PMMA* brush layer deposition. The accurate control of the space between two guiding pattern ridges allows us to analyze the behavior of the block copolymer chains under confinement with nanometer precision. We have developed a free energy model that successfully describes, how to design topographical guiding patterns to direct the self-assembly of block copolymers to obtain patterns with low defect levels. The model describes the free energy of a system with a non-zero density of defects on a semi-empirical basis.

2A.2 Experimental Section

The work-flow for the fabrication of aligned block copolymer template in topographical guiding patterns fabricated by EUV-IL is depicted in *figure 2A.1 a)*.

2A.2.1 HSQ deposition, exposure and development

We used flowable oxide *FOX 16* by Dow Corning Corporation diluted 1:6 in *methyl isobutyl ketone (MIBK)*. Spin coating this solution at 2000 rpm for 1 min on 2×2 cm^2 Si chips yield a film thickness of 70 nm. After spin coating, the chips are transferred in the EUV-IL exposure chamber and pumped down to a pressure of 10^{-7} mbar. Upon exposure to EUV radiation, a cross-linking process [12,20] is initiated and the exposed areas are converted into a SiO_2-like material. The non-cross-linked, unexposed *HSQ* is consequently developed away in an alkaline developer (Microposit 351 developer diluted 1:3 in water) for 30 s and then rinsed in deionized water, yielding the desired line/space guiding patterns. The guiding patterns are fabricated using transmission gratings of 300 nm pitch to create a fixed 150 nm pitch interference pattern on the chips. The transmission mask has been fabricated by e-beam lithography by the exposure of an *HSQ* film spun on an Si_3N_4 membrane, which is transparent for EUV radiation [1,21]. The mask used in this work is optimized to produce 50 % duty cycle (75 nm half pitch) line/space patterns. By varying the exposure dose below and above the nominal dose, one can reduce or increase the duty cycle of the line/space patterns with great accuracy. This nanometer precision over the width of the guiding pattern is essential to help us better understand the mechanism of directed self-assembly of block copolymers in our system. In this study, the exposure dose (i.e. dose on the mask) has been varied from 350 $^{mJ}/_{cm^2}$ to 1050 $^{mJ}/_{cm^2}$ in a step and repeat manner. The achieved duty cycles are between 23 % - 67 % which correspond to trench widths of 115 and 35 nm respectively.

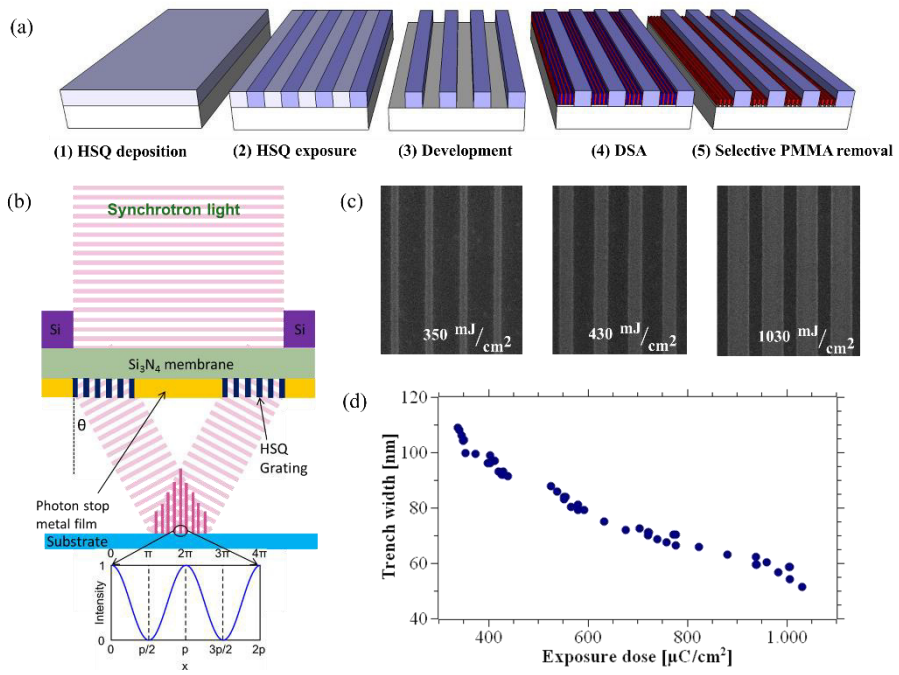

Figure 2A.1: Work-flow and guiding pattern fabrication. a): The work-flow used to fabricate the guiding patterns and to direct the self-assembly of block copolymers in EUV-IL fabricated patterns consists of the exposure and development of HSQ, the deposition and self-assembly of block copolymers and the subsequent removal of PMMA, b): a scheme showing the principle of EUV-IL, where the diffracted beams create and interference pattern that is recorded in a photoresist-covered substrate, c): guiding patterns exposed at different exposure doses yield different guiding pattern widths, d): the amount of cross-linked HSQ can be increased by raising the exposure dose. For this reason, we are capable of tailoring the trench width with nanometer precision with slight variations of the exposure maintaining the pitch of the features constant at 150 nm.

2A.2.2 Deposition of neutral brush layer

In order to deposit a brush layer that grafts both to the guiding pattern walls and to the guiding pattern bottom, a solution of 1.5 % neutral

l brush layer in *PGMEA* is spin-coated for 30 s at 4000 rpm. For the deposition of a thin brush layer grafting only to the bottom of the trench, a 0.25 % solution in *PGMEA* is also spin-coated at 4000 rpm for 30 s.

Due to the strongly diluted solution, the deposited film is thin enough to be deposited exclusively on the bottom of the trench [22]. In both cases, the sample undergoes a 5 min annealing step at 230 ºC. This step is required to initiate the brush layer grafting to the

underlying surface. The residual, non-grafted material is removed by a rinsing step in *PGMEA*. The neutral brush layer is a *PS-r-PMMA* random copolymer containing 58 wt% *PS* and 42 wt% *PMMA* at a molecular mass $M_{brush} = 7.9\ ^{kg}/_{mol}$ and a polydispersity index $PDI_{brush} = 1.85$.

2A.2.3 Deposition and self-assembly of block copolymer

We work with a *PS-b-PMMA* block copolymer with a molecular mass $M_{BCP} = 42.3\ ^{kg}/_{mol}$. It consists of 43 wt% *PS* and 57 wt% *PMMA* with a polydispersity index $PDI_{BCP} = 1.1$. When deposited on a neutral brush layer, it self-assembles in a lamellar structure with a natural pitch of 23.4 nm. The spin coating of a 1.5 % solution in *PGMEA* at 2000 rpm for 30 s yields a 28-nm-thick film in free surface. To initiate the microphase separation process, the material is annealed in a nitrogen environment for 10 min at 230 ºC.

2A.2.4 Selective PMMA removal

In order to fabricate technologically useful etching masks, one of the block copolymer domains has to be removed selectively. In this work, we design a selective reactive ion etching (RIE) step in an Oxford 80Plus RIE applying a gas mixture of 5 sccm O_2 and 40 sccm CHF_3 at 50 mTorr pressure. At a power of 40 W, this process etches *PMMA* at 46 $^{nm}/_{min}$ and *PS* at 18 $^{nm}/_{min}$. This means that the selectivity between the two materials is 2.5.

2A.3 Results

2A.3.1 Guiding pattern fabrication

Examples of guiding patterns resulting from three different exposure doses are depicted in *figure 2A.1 c)*. *Figure 2A.1 d)* shows a plot of the variation of the trench width *w* as a function of the exposure dose. The curve that relates the exposure dose with the trench width has a negative slope, since the trench width corresponds to the non-cross-linked area. The trench width is the key parameter in this work, because it defines the space that confines the block copolymer lamellae laterally.

As we have mentioned before, defects in DSA usually originate from rough or incommensurate guiding patterns. *Table 2A.1* depicts the results of an LRW/LER analysis of four representative guiding patterns from this study confirming their extraordinarily low roughness. Image pre-processing included the bi-cubic interpolation, rotation of the image and Gaussian filtering. The threshold for the edge detection was set to 0.5 of the maximum signal of the image. The numbers displayed in *table 2A.1* represent the 3σ-values of the analyzed image. We observe better results for LWR and LER as the exposure dose is increased, finally yielding sub-nm line edge roughness for duty cycles larger than 50 %.

Exposure dose [$^{mJ}/_{cm2}$]	Trench width [nm]	LWR [nm]	Std. error (LWR) [nm]	LER [nm]	Std. error (LER) [nm]
950	58.5	1.20	0.069	0.88	0.79
680	70.2	1.90	0.056	1.84	0.26
430	93.6	2.26	0.128	2.24	0.30
350	105.3	3.00	0.037	2.16	0.63

Table 2A.1: Overview of analysis of four representative guiding patterns depicting the respective 3σ-LWR/LER values and their standard error.

2A.3.2 Control over interface energy by surface neutralization

The deposition of an intermediate neutral brush layer allows it to control the interaction between the block copolymer and the substrate. We considered the deposition of the neutral brush layer only after the EUV-IL step, because EUV radiation interacts strongly with *styrene* and *methyl(methacrylate)* [23,24]. The chemical integrity of the neutral brush is absolutely required [25] to study the effect of different ways to deposit the neutral brush layer.

The deposition of the 1.5 wt% *PS-r-PMMA* solution yields a neutral layer that is thick enough to cover both the bottom of the trench, and also the walls, so that during the self-assembly both *PS* and *PMMA* wet the guiding pattern walls *and* bottom of the trench. The block copolymer self-assembles consequently in short aligned lamellae perpendicular to the guiding pattern, as depicted in *figure 2A.2 a)*. In the present study, this behavior is not desired and for this reason we discard this result for further analysis.

The deposition of the 0.25 wt% brush layer solution yields a 3 nm thick film on a non-patterned surface both before and after the rinsing step. After depositing and annealing the block copolymer, we observe self-assembly in lamellae parallel to the guiding pattern walls (see *figure 2A.2 b)*). This orientation can be explained by the absence of *PS-r-PMMA* macromolecules grafted to the guiding pattern walls. For this reason, the block copolymer interacts directly with the *PMMA*-attractive SiO_2 walls. A top view of the block copolymer self-assembly configurations using 0.25 wt% brush layer solution is depicted in the scanning electron micrographs of *figure 2A.2 b)*.

In the complete absence of a neutral brush layer (see *figure 2A.2 c)*) the block copolymer self-assembles as depicted in the sketches on the top of the structure [26]. Similar to the guiding pattern walls, the silicon substrate is preferentially wetted by the *PMMA* domain. For this reason, we expect a wetting layer on the bottom of the trench interrupting the morphological integrity of the 3-D structure and making a pattern transfer more difficult.

A more detailed comparison between the two aforementioned morphologies is provided later.

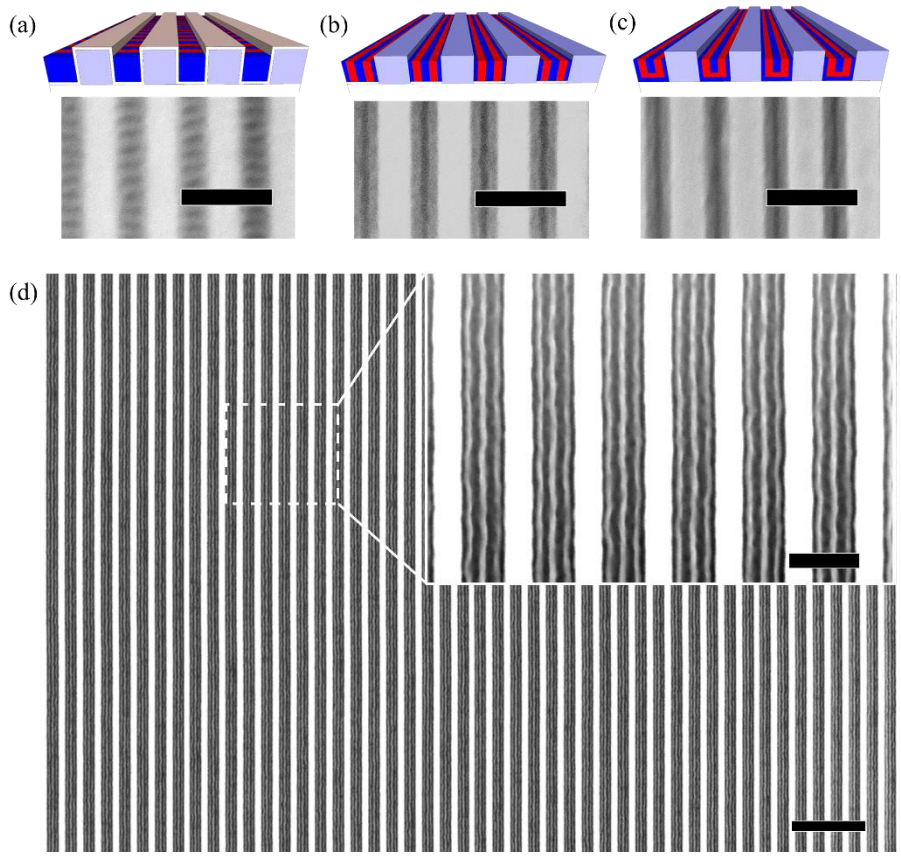

Figure 2A.2: Self-assembly modes and example of successful DSA in commensurate guiding pattern a)-c): Three different block copolymer assembly modes in graphoepitaxy as a function of neutral brush layer deposition conditions: thick, i.e. covering top and side walls of guiding pattern features, thin, i.e. covering only the space between the guiding pattern features and none; scale bars are 100 nm, d): large-area defect-free self-assembly of block copolymers in topographical guiding pattern fabricated by EUV-IL. The trench width is 109 nm and reduced the block copolymer pitch about 6.5 % with respect to an assembly in free surface; scale bar: 650 nm, scale bar in-set: 150 nm.

Comparing the deposition modes with respect to their capability to direct the self-assembly of block copolymers into lithographically relevant structures (i.e. ordered and in ideal shape for pattern transfer), we conclude that the 0.25 wt% brush solution yields the best results, because the observed morphology demonstrates structural integrity over

the whole film thickness. A detailed comparison between the two morphologies is provided in the *results* section.

We have achieved a defect-free directed self-assembly over several tens of square micrometers after depositing and annealing of the block copolymer in a commensurate guiding pattern. *Figure 2A.2 d)* shows an SEM image of the directed self-assembly of block copolymers in guiding pattern trenches of 109 nm. To increase contrast and facilitate the acquisition of SEM images, the *PMMA* domains have been removed before the analysis. Throughout this *chapter* the number of *PS* domains per trench is used as a reference to categorize the guiding patterns. In total we count five *PS* domains in the configuration depicted in *figure 2A.2 d)*. Two of these domains remain almost unseen in the SEM images because of the large signal originating from the edges of the guiding pattern features. To transfer three fins into the substrate, we hence need trenches to be wide enough for the self-assembly of five *PS* domains, because experiments have shown that the two outermost *PMMA* domains do not take part in the pattern transfer process since they are not removed in the selective dry etching step [14,18].

2A.4 Discussion

2A.4.1 Influence of brush layer thickness on self-assembly

In the following, we experimentally assess the effect of the brush layer deposition mode and describe its influence on the morphology of the self-assembly below the surface. Information about the three dimensional structure was obtained by a controlled selective dry etching step as introduced in the experimental section. Due to the etching selectivity of the *PS* domain with respect to the *PMMA* domain, SEM imaging of the structures after the etching step provides useful information about the morphology of the respective structure below the surface.

Figure 2A.3 a) and *figure 2A.3 b)* depict the directed self-assembly in a guiding pattern before the RIE process without and with a neutral brush layer. *Figure 2A.3 c)* and *figure 2A.3 d)* show top view SEM images of the same structures after the RIE process. The reconstructed morphology in cross-section is sketched in the respective in-sets.

For samples with a thin underlying brush layer, we observe that the number of *PS* domains on the surface and below the surface is the same. We deduce that the block copolymer in direction normal to the substrate self-assembles in continuous vertical lamellae. In absence of the brush layer the number of *PS* domains decreases after the dry etching. This

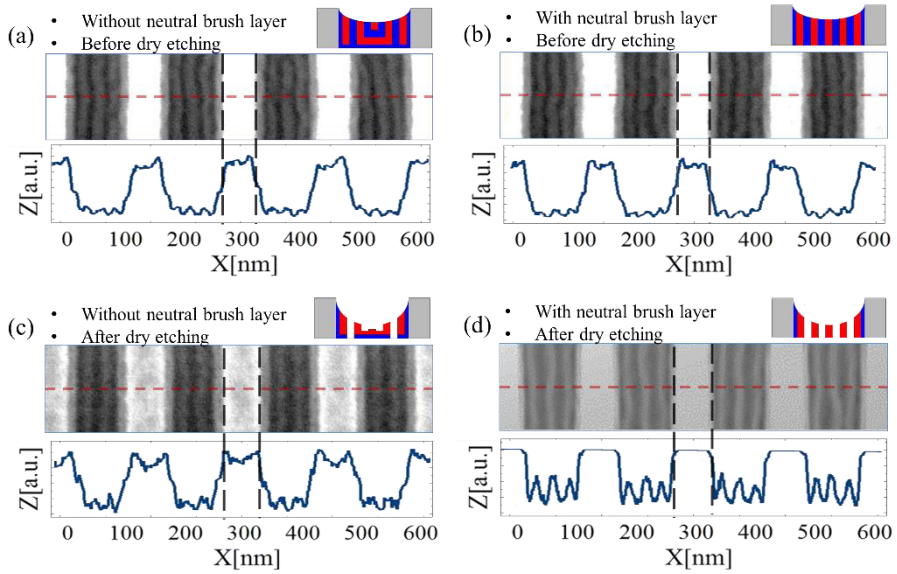

Figure 2A.3 Comparison of different self-assembly modes assessed by reactive ion etching. a): SEM top-view image and single line intensity profile of DSA for onion-shape morphology before RIE, b): SEM top-view image and single line intensity profile of DSA for vertical lamella morphology before RIE, c): SEM top-view image and single line intensity profile of DSA for onion-shape morphology after RIE, d): SEM top-view image and single line intensity profile of DSA for vertical lamella morphology after RIE.

indicates that the domains are not continuous vertical lamella and the block copolymer is arranged in a U-shape caused by the *PMMA* wetting both the guiding pattern walls and the bottom of the trench. These results are consistent with previous studies [22,27].

2A.4.2 Influence of the trench width on self-assembly

Another interesting question for further scrutiny is how the defectivity for block copolymers self-assembled in topographical guiding patterns differs as a function of the guiding pattern width *w* and the brush layer deposition mode.

We compare the vertical lamellae with the U-shaped morphology in terms of the capability of guiding patterns of different trench widths *w* to direct the self-assembly. We have grouped together guiding patterns with similar trench widths that yield similar self-assembly results. In particular for samples with a thin brush layer, we identify certain periodically recurring guiding pattern width areas that yield a large number of imperfections in the self-assembly. We show representative SEM images for the groups denoted 1-5 (*figure 2A.4 a)*). All the images were taken from samples with thin brush layer and after the removal of *PMMA*.

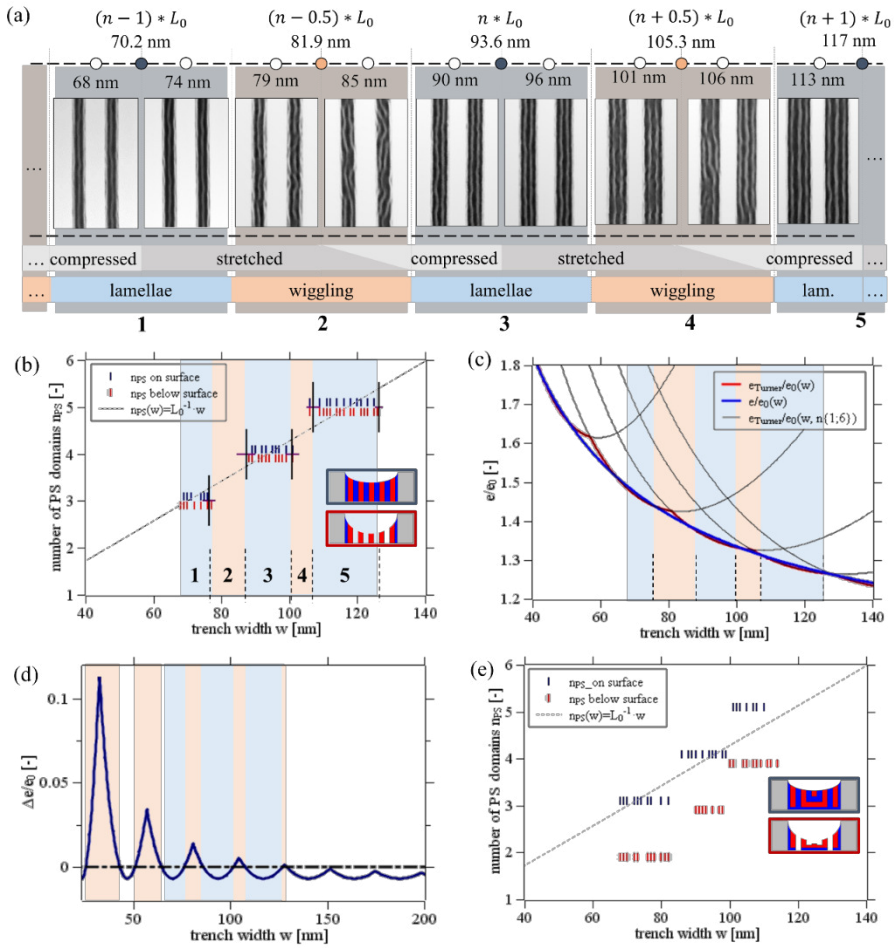

Figure 2A.4: Groups of self-assembly and 3-D morphology of the domains. a): Representative SEM images of the groups as shown in figure 2A.4 b), b): graphics showing the number of PS domains n_{PS} deposited as a function of the guiding pattern trench width comparing the deposition in trenches with a thin neutral brush layer as shown in the inset. The colored areas refer to experimentally accessible trench widths, where the blue shaded areas represent those trench widths with defect-free self-assembly and the yellow areas refer to areas with a high defectivity, c): free energy per block copolymer chain in units of the free energy in unconfined state as a function of the trench width as predicted by Turner [28] *(red curve, based on grey curves) and according to the calculation presented in this paper (blue curve), d): curve showing the energy difference between the two models presented in panel c), e:) graphics showing the number of PS domains deposited as a function of the guiding pattern trench when no neutral brush layer is deposited, as shown in the inset.*

Figure 2A.4 b) relates the number of *PS* domains on the surface and the number of *PS* domains under the surface to the trench width for the two different self-assembly

morphologies. Trench widths are assigned to groups according to the number of *PS* domains that fit into the trench. For the vertical lamellar morphology, self-assembly with a low defectivity is only observed in the groups 1, 3 and 5 (see *figure 2A.4 a)*). It is not possible to assign a discrete number of *PS* domains to the block copolymer patterns self-assembled in incommensurate guiding patterns of groups 2 and 4 in *figure 2A.4 b)*, because both *n* and *n+1* domains coexist in this area. The patterns that are capable of directing the self-assembly in practically defect-free fashion are characterized by trench widths close to integer multiples of the natural pitch of the block copolymer. The expected number of *PS* domains as a function of trench width is indicated by the grey dashed line in *figure 2A.4 b)*). This curve merely serves as guidance for the reader, given the fact that the number self-assembled block copolymer domains has to be an integer number.

By determining the trench widths at which the block copolymers change their self-assembly morphology from defect-free to defect-loaded (or vice versa), we can extract the maximum stretch / compression that the chains sustain before it becomes energetically more favorable to form defects.

We refer to the defective state as each morphology in which the block copolymer domains are not oriented perfectly parallel to the guiding pattern walls [29], as shown in the representative images of group 2 and group 4 (see *figure 2A.4 a)*). We observe that the block copolymer domain wiggles, which is known to be an effect to reduce chain deformation at the expense of augmenting the area of the intermaterial dividing surface (IMDS) [30]. This phenomenon is also known from the behavior of liquid crystals under strain [31].

We observe domain-wiggling (see *figure 2A.4 a), group 2*) with a wavelength of few tens of nanometers in the case of chain stretching. We refer to chain stretching, when the number of domains self-assembled in the trench *n* multiplied with the equilibrium domain spacing L_0 is smaller than the trench width *w*, i.e. when $n\ L_0 < w$. The appearance of domain wiggling has been predicted by Wang as a stable state for block copolymer patterns confined in patterns exceeding a determined incommensurability [30] and explains our observation of the abrupt occurrence of domain wiggling.

For large pattern incommensurability (characterized by $w > (n +/- 0.5)\ L_0$), the system partially changes its self-assembly morphology from *n* domains to *n+1* domains, giving rise to a high density of point-like defects. We observe the coexistence of the assembly of *n* domains characterized by large chain stretching (and expressed by domain wiggling) at one hand, and domains where *n+1* domains are self-assembled (characterized by chain compression) on the other hand. Point-like defects are observed in the transition areas from *n* to *n+1* domains. The coexistence of *n* and *n+1* domains in highly incommensurate

guiding patterns has, furthermore, previously been observed and reported [32]. The effect that the system does not self-assemble in a pure *n+1* domain morphology for trench widths $w > (n +/- 0.5) L_0$ is due to a difference between the compression modulus and the stretching modulus in block copolymers. It requires more energy to compress a block copolymer system perpendicular to its domains than to stretch it in the same direction. Although the spring model of polymer chains predicts that the energy stored in a chain compressed by a factor *f* is the same as the energy stored in a chain that is stretched by a factor *f,* in the particular system of block copolymers chain stretching contributes to a reduction of the IMDS and the compression leads to an increase of the IMDS.

The defects observed in the transition zones between *n* domains (stretched chains, defined by wiggling) and *n+1* domains (compressed chains) can neither be clearly identified as dislocation nor as disclination point defects. In the following, we will therefore refer to theses defects as point-like defects. Recent results on the analysis of defects in the directed self-assembly using chemical guiding patterns suggest that point defects represent a metastable state that would disappear in case of an infinitely large annealing time, suggesting that the system has not yet reached its equilibrium state.[33]

In contrast to our observations of the self-assembly morphology in the groups 2 and 4, the defect density of the aligned block copolymers inside the pattern of groups 1, 3 and 5 is very low. In particular, group 3 includes guiding patterns with trench width ranging from 86 nm to 100 nm. The energetically most beneficial trench width for this morphology is 93.6 nm, because this is four times the natural pitch of the block copolymer. The number of IMDS (i.e. *PS/PMMA* interfaces) equals the number of block copolymer chains across the trench, so that we can state that eight macromolecules assemble in group 3. The maximum compression per chain at the moment when the assembly mode changes is 0.78 nm and the maximum stretching per chain is 0.9 nm. The same calculus for group 5 yields an average compression per chain of 1 nm and 0.94 nm respectively. The average stretching per chain for group 1 is estimated to be 1 nm. These values correspond to the capability of the chains to compress on average 8.1 % and to stretch 7.6 % with respect to their expansion at natural pitch, before a defective self-assembly state occurs. The occurrence of the domain wiggling – previously referred to as buckling instability – has previously been associated with the yield point of block copolymers in macroscopic samples [34,35]. Coarse-grained modelling has determined the onset of the buckling instability for a critical strain of 6 % [36], which is in excellent agreement with the values we have determined in our nanoscale system.

Furthermore, we analyzed our system using the free energy model developed by Turner [28] that has already been successfully employed by a number of other authors [9,13,37] to explain the block copolymer self-assembly. The underlying principle is the energy

balance between formation of interfaces between *PS* and *PMMA*, and the deformation of the chains taking the interaction between the guiding pattern walls and the preferentially wetting polymer domain into account. The natural pitch L_0 of the block copolymer is the result of an energy minimization process. If the block copolymer chains are stretched so that the pitch is increased, the number of IMDS per unit length along the trench width is reduced. This is one way to reduce the enthalpy of the system. Stretching the polymer chains leads on the other hand to a reduction of the entropy of the system [38]. The black parabolas in *figure 2A.4) c)* represent the normalized free energy per chain $\frac{e_T}{e_0}$ according to Turner for the self-assembly of $n = \{1;6\}$ domains in trenches of width w, given by the following equation:

$$\frac{e_T}{e_0} = \frac{1}{3}\left(\left(\frac{w}{n*L_0}\right)^2 + \frac{2*n*L_0}{w} + \frac{2*\Gamma*L_0}{w}\right) \qquad (2A.4)$$

where Γ is a measure for the energy penalty induced through the polymer-wall interaction, which represents the incommensurability $w/(n\ L_0)$ of the trench. The surface tensions required to estimate Γ have been extracted from works of different authors [39–41]. The red curve in *figure 2A. 4 c)* represents the minimum of these parabolas and thus predicts a determined number n of domains for each trench width characterized by the least free energy. The free energy e_T is normalized to the bulk free energy per chain e_0.

We always observe the creation of a high defect density in the close vicinity of those trench widths, where the guiding pattern incommensurability reaches its maximum and Turner's model predicts a crossover from n domains to $n+1$ domains. These areas are represented by the beige boxes in figure *2A.4 b), 2A.4) c)* and *2A.4 d).* Neither the formation of domain wiggling nor the formation of metastable point-like defects can be explained by the Turner model. In the following, we will provide an extension of the model to quantify the free energy of the defective state.

The blue curve in *figure 2A.4 c)* shows a semi-empirical function describing the free energy of the defect-loaded state. Although the physical origin of wiggling and the metastable point-like defects at the transition from n to $n+1$ domains is fundamentally different, here it makes sense to join the both effects together to the "defect-loaded state", and henceforth only to distinguish between the defect-free and defect-loaded state. This blue curve is later used to identify those trench widths where the self-assembly in the defect-loaded state is energetically favorable. To find this curve, we have assumed that the formation of defects and wiggling leads to the relaxation of the chains to their bulk energy level, and in return adds an unknown, but constant energy penalty per chain e_p/e_0 that accounts for the average free energy per chain that exceeds the bulk free energy. Hence, the relaxation of the chains to bulk energy level can be implemented in Turner's

formula assuming that the incommensurability is 1. After adding the constant energy penalty term, the modified formula to describe the free energy of the observed morphology, called $^{e}/_{e_0}$, is of the form:

$$\frac{e}{e_0} = 1 + \frac{2*\Gamma*L_0}{3*w} + \frac{e_p}{e_0} \qquad (2A.5)$$

A more detailed derivation of this formula is presented in the sections *2A4.5 – 2A.4.8*. We can now estimate $^{e_p}/_{e_0}$ by fitting the curve to the position of crossover points between the defect-free and the defect-loaded state. *Section 2A.4.4* is dedicated to the accurate determination of the crossover points. The fitting process yields $^{e_p}/_{e_0} = 0.00704$ with a coefficient of correlation $R^2 = 0.9989$. Assuming that the system self-assembles in the morphology that is characterized by the minimum free energy, we may simply calculate $\frac{\Delta e}{e_0} = \frac{e_T}{e_0} - \frac{e}{e_0}$. The result of this operation is plotted in *figure 2A.4 d)*. The defect-loaded state is energetically favorable for values $\frac{\Delta e}{e_0}(w) > 0$, while the defect-free state according to Turner is energetically favorable for $\frac{\Delta e}{e_0}(w) < 0$. We can conclude that the observed defect-loaded state is energetically unstable for trench widths larger than 130 nm. We thus derive that the change from the defect-free to the wiggling state occurs as soon as the energy penalty induced through the deformation of the chains exceeds 0.7 % of the bulk free energy level. The reason why this state for increasing trench width successively disappears is that incommensurability is compensated by a steadily increasing number of chains yielding a smaller amount of energy stored in the chain stretching to compensate for the same absolute incommensurability. A more detailed explication of this analysis can be found in the *sections 2A.4.4 - 2A.4.7*. We may not forget at this point that this estimation is only true as long as the trench width is smaller or close to the correlation length of the block copolymer, which represents the limit of the directed self-assembly of block copolymers by topographical guiding patterns. For very large multiplication factors the formation of defects similar to self-assembly in free surface will play a successively larger role. Despite of the observation of two different defect formation mechanisms (i.e. domain wiggling and point-like defects), we find that the free energy of the defect-loaded state can be described with one single function. The energy reduction in the wiggling morphology can be qualitatively explained by a partial release of the energy stored in chain stretching through the introduction of additional IMDS.

Figure 2A.4 e) depicts the results of the analysis of the number of *PS* domains n_{PS} as a function of the trench width w on the surface and below the surface for the directed self-assembly in trenches without depositing any neutral brush layer. We observe that the number of *PS* domains after etching is lower than before the etching step for all investigated trench widths. The conclusions we draw from this observation is that there

is no trench width that enables the directed self-assembly of block copolymers in perfectly vertical lamellae unless there is a neutral brush layer deposited. We do not observe the self-assembly in a morphology that displays a massive formation of defects as observed in case of the neutral brush layer deposition. A plausible explanation for this observation is that the U-shaped organization of the block copolymer in the trench (i.e. the combination of vertical and horizontal lamellae) facilitates the relaxation of the chains and reduces the stretching of the domains as a result of incommensurability.

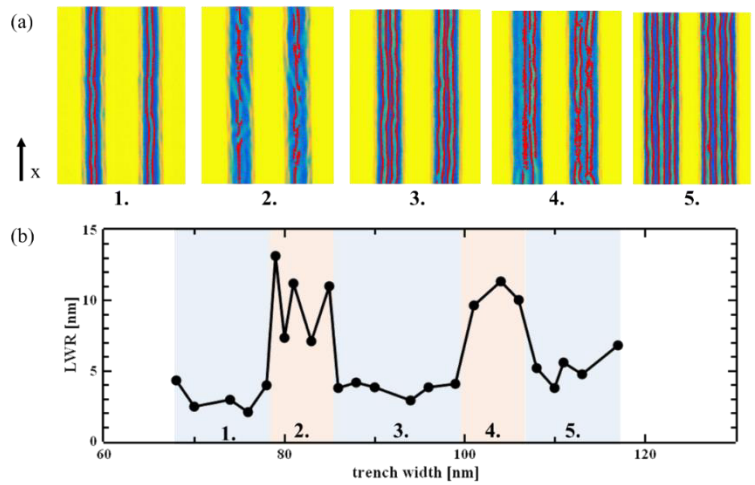

Figure 2A.5: LWR as a function of the trench width. a) Representative results of LWR analysis for the groups 1-5, b) LWR as a function of the trench width w yields significantly higher values for trench widths far away from the commensurate guiding patterns.

2A.4.3 Line width roughness as a function of the trench width

The LWR of an object is defined as the standard deviation of its width, defined as the distance between a right and a left border. Representative LWR measurements for each of the groups are depicted in *figure 2A.5 a).* We observe that the LWR increaseses for high-defect-density block copolymer patterns. This is not the case because the LWR of the block copolymer actually increases by such a large factor, but because the measurement direction is defined in one determined direction *x* indicated by the black arrow in *figure 2A.5 a)*. A deviation from this direction is expressed by a larger measured line width at this position.

2A.4.4 Determination of crossover points

One challenging part of this work is the accurate determination of the trench width *w*, at which the block copolymer system changes from the defective morphology to the defect-free morphology and vice versa. We take advantage of the finit length of the mask

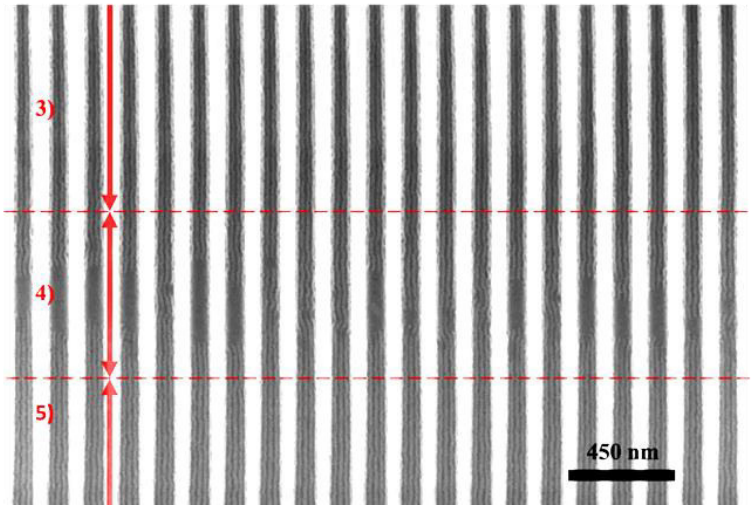

Figure 2A.6: Examples of how to determine the cut-off values for each group. The numbers in the images indicate, which group this part of the guiding pattern belongs to. The dashed line indicates the approximate location of the crossover point.

transmission gratings and therefore of the interference pattern. We observe that the feature width becomes successively smaller towards the border of the pattern. In these last micrometres towards the border of the guiding pattern width decreases at a rate of roughly 1 nm per 100 nm. For this reason, the borders of the guiding pattern are ideal to determine the specific trench widths, at which the self-assembly mode changes from one morphology to the other. Examples of this part of the guiding pattern is depicted in *figure 2A.6*.

To minimize measurement uncertainties, we extracted the trench widths from 49 morphology changes. The results of this analysis are summarized in *table 2A.2* below.

x → y	Mean [nm]	Std. Dev. [nm]	$^{e}/_{e0}$ [-]	$n\,L_0$ [nm]	$\#_{Chains}$ [-]	Chain Length [nm]	ΔChain Length [nm]	ΔChain Length [%]
1 → 2	76.25	1.75	1.413	70.2	6	12.7	1.00	8.6
2 → 3	87.3	2.49	1.369	93.6	8	10.9	0.78	6.7
3 → 4	100.8	1.74	1.316	93.6	8	12.6	0.90	7.7
4 → 5	107	1.80	1.299	117	10	10.7	1.00	8.5
5 → 6	126.4	0.89	1.253	117	10	12.6	0.94	8.0

Table 2A.2: Determination of the crossover points between defective and non-defective state in block copolymer self-assembly

2A.4.5 Analyzing the system according to Turner

According to Turner, the free energy per block copolymer chain in a system confined between two parallel plates normalized to the bulk free energy per chain e_0 can be written as [9,28]:

$$\frac{e_T}{e_0} = \frac{1}{3}\left(\lambda^2 + \frac{2}{\lambda} + \frac{2}{n}\frac{*\Gamma}{*\lambda}\right) \qquad (2A.6)$$

The energy per chain in this system is a function of the parameter λ (which indicates the incommensurability of the trench with respect to an integer multiple of the natural pitch of the block copolymer; see *formula 2A.7)* and Γ (which balances the interface energy between one of the blocks and the confining wall, and the interface energy between the two blocks; see *formula 2A.8*):

$$\lambda = \frac{w}{n*L_0} \qquad (2A.7)$$

and

$$\Gamma = \frac{\gamma_{SiO_2-PMMA}}{\gamma_{PS-PMMA}} \qquad (2A.8)$$

The interface free energy between two materials can be calculated by an extension of Young's equation, as presented by Owens and Wendt [39]. The parameters required to do the calculus are the dispersive (γ_D) and polar (γ_P) contributions to the surface free energy of the respective materials.

$$\gamma_{A-B} = \left(\sqrt{\gamma_{P,A}} - \sqrt{\gamma_{P,B}}\right)^2 + \left(\sqrt{\gamma_{D,A}} - \sqrt{\gamma_{D,B}}\right)^2 \qquad (2A.9)$$

Using literature values, this calculation yields $\Gamma = 2.1$ [40–42]. Here, material *A* is *PMMA* and material *B* is SiO_2. Filling this result into *formula 2A.6*, we can determine the curves for the free energy per chain as a function of *w* for *n = {1; 2; 3; ...},* where *n* corresponds to the number of *PS/PMMA* repeat units. This calculation provides us with the free energy per chain, when a number of *n* repeat units is confined in a trench with width *w*. The corresponding curves are depicted in *figure 2A.7* in pink *(n = 2)*, brown *(n = 3)*, green *(n = 4)*, blue *(n = 5)* and cyan *(n = 6)*. The preferred self-assembly mode is always the one that exhibits the minimum free energy per chain, which is symbolized by the black dashed line. The light blue shaded area in *figure 2A.7* represents the trench widths that we have worked with in the course of our experiments and the beige boxes represent those zones, where we observe the defect-loaded state, which cannot be explained with Turner's formula.

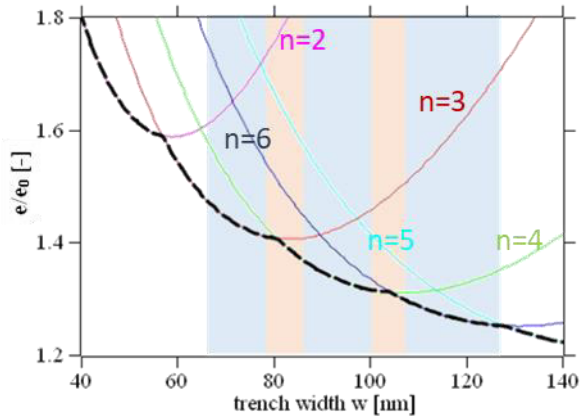

Figure 2A.7: Free energy per chain according to Turner. Colored parabolas: free energy per chain as a function of trench width w for n = {2;6} PS and PMMA domains. Black dashed curve: Minimum of all colored curves. Blue shaded area: Process window in this work. Light-orange-shaded areas: Defect-loaded self-assembly.

2A.4.6 The influence of Γ on the determination of crossover points in Turner model

Reliable information about the polar and the dispersive surface free energy of SiO_2 (crosslinked *HSQ* is chemically very similar to amorphous SiO_2) is somehow hard to find and we would like to probe the justifiable concern that inaccuracy has been introduced to the calculation of the crossover points due to that. Filling *formula 2A.7* into *formula 2A.6*, yields

$$\frac{e_T}{e_0} = \frac{1}{3}\left(\left(\frac{w}{n*L_0}\right)^2 + \frac{2*n*L_0}{w} + \frac{2*\Gamma*L_0}{w}\right) \qquad (2A.10)$$

Furthermore,

$$\frac{\partial\left(\frac{e_T}{e_0}\right)}{\partial w} = 0 \qquad (2A.11)$$

yields

$$w_0 = \sqrt[3]{\frac{n+2*\Gamma}{n^2*L_0}} \qquad (2A.12)$$

Therefore, we can tell that the location of the minimum free energy in a confined system for constant n is proportional to the cube root of Γ. Looking closely at *figure 2A.7*, we observe surprisingly that the minima of the parabolas do not necessarily form part of the free energy curve. The defect-loaded morphology of the block copolymers always occurs

in the vicinity of crossover points between two of minimum free energy curves c_n and c_{n+1}. Accordingly, the crossover points have the mathematical property

$$\left(\frac{e_{vert}}{e_0}\right)_n = \left(\frac{e_{vert}}{e_0}\right)_{n+1} \qquad (2A.13)$$

, which by using *formula 2A.7* becomes

$$\frac{1}{3}\left(\left(\frac{w}{n*L_0}\right)^2 + \frac{2*n*L_0}{w} + \frac{2*\Gamma*L_0}{w}\right) = \frac{1}{3}\left(\left(\frac{w}{(n+1)*L_0}\right)^2 + \frac{2*(n+1)*L_0}{w} + \frac{2*\Gamma*L_0}{w}\right) \qquad (2A.14)$$

Here, the term containing Γ easily cancels out. This means that an inaccurate estimation of the wall/polymer interaction Γ does not affect the position of the crossover points and is therefore no essential parameter for our analysis.

2A.4.7 Extension of Turner's model to predict the self-assembly mode

In this section we will explain, why block copolymers in certain trench width regimes abruptly change their morphology from stretched vertical lamellae with no or almost no defects to a state with a very high defect density (i.e. the regime where the block copolymer shows wiggling or forms point-lik defects). To do so, we will derive a mathematical expression that allows us to describe the free energy per chain normalized to e_0 in the defect-loaded state (i.e. the morphology that is not explained by Turner's model), fit it to our experimental data and compare it to the model presented by Turner. Therefore, we assume that the block copolymer always self-assembles in the morphology with the minimum free energy.

Let us now assume that the free energy of the system we investigate is the sum of four energy components E_{tot} with

$$E_{tot} = E_{S,L0} + E_{AB,L0} + E_{AW} + E_P \qquad (2A.15)$$

The components introduced above are defined as follows:

> *$E_{S,L0}$: Energy stored in the stretching of the chains in bulk conditions, i.e. when the block copolymer pitch equals the equilibrium pitch L_0. Here, one single chain is stretched to the length of $L_0/2$*
>
> *$E_{AB,L0}$: Energy contribution due to the interface between the blocks A and B of the block copolymer in bulk conditions*
>
> *E_{AW}: Energy contribution due to the interaction between the block A and the walls (we assume that only one block, namely PMMA, interacts with the wall* [9,28]*)*
>
> *E_P: An energy penalty that covers every possible energy component in our system that is not included in the first three terms, including mainly the*

formation of defects, but possibly also energetic components related to stretching and the increase of interface area. This term does not appear in any way in the model of Turner, because it does not consider any defects in his system.

As our system consists of a total number of *b* chains, we state that the total free energy of the system E_{tot} equals the product of *b* chains and their respective free energy *e*, such that *formula 2A.15* can also be written as:

$$E_{tot} = b * e = b * (e_{S,L0} + e_{AB,L0} + e_{AW} + e_P) \qquad (2A.16)$$

Minuscule letters refer to one chain, while capital letters refer to the energy of the entire system.

As Turner's model analyzes the energy per chain normalized to the bulk free energy, we will have to divide *formula 2A.16* by the number of chains and the energy of a single block copolymer chain in bulk configuration $(b * e_0)$, which yields:

$$\frac{e}{e_0} = \frac{e_{S,L0}+e_{AB,L0}+e_{AW}+e_P}{e_0} = \frac{e_{S,L0}+e_{AB,L0}}{e_0} + \frac{e_{AW}}{e_0} + \frac{e_P}{e_0} \qquad (2A.17)$$

The sum of free energy due to chain stretching and the creation of *PS/PMMA* interfaces in bulk configuration $e_{S,L0}+e_{AB,L0}$ is precisely defined as e_0, so that *formula 2A.17* can be simplified to:

$$\frac{e}{e_0} = 1 + \frac{e_{AW}}{e_0} + \frac{e_P}{e_0} \qquad (2A.18)$$

Now, let us have a closer look at the energy formula derived by Turner*:*

$$\frac{e_T}{e_0} = \frac{1}{3} * \left(\lambda^2 + \frac{2}{\lambda} + \frac{2*\Gamma*L_0}{3*w}\right) \qquad (2A.19)$$

The first summand in brackets accounts for the chain stretching, the second term accounts for the interface energy between the blocks and the third term corresponds to the energy contribution caused by the interaction between one of the block copolymer blocks and the wall. Assuming that $\lambda = 1$ (the chains are perfectly commensurate), as defined in *formula 2A.7,* yields

$$\frac{e_T}{e_0} = \frac{1}{3} + \frac{2}{3} + \frac{2*\Gamma}{3*n} = 1 + \frac{2*\Gamma*L_0}{3*w} \qquad (2A.20)$$

After clarifying this, we are capable of isolating the interaction term between the wall and the block copolymer, and estimate the contribution of the wall/block copolymer interaction to the free energy per chain in the system (using $\Gamma = 2.1$ and $L_0 = 23.4$):

$$\frac{2*\Gamma*L_0}{3*w} = \frac{e_{AW}}{e_0} = \frac{32.76\ nm}{w\ [nm]} \qquad (2A.21)$$

Filling in this term into *formula 2A.18* yields:

$$\frac{e}{e_0} = 1 + \frac{32.76}{w} + \frac{e_P}{e_0} \qquad (2A.22)$$

Let us furthermore assume that the term $\frac{e_P}{e_0} = const. \neq f(w)$.This term is likely to contain contributions from stretching energy and an additional energy component due to the formation of additional IMDS. It accounts for all the additional free energy components that the macromolecule may be subject to. We know that the curve we search for intersects with the curve derived by Turner exactly in the crossover points, where we observe the self-assembly morphology to change from the defect-free state to the defect-loaded state, and vice versa.

For this reason, we fit the curve

$$\frac{e}{e_0} = 1 + \frac{32.76}{w} + C \qquad (2A.23)$$

to the five experimentally determined crossover points as presented in *table 2A.2*, 2nd and 3rd column. This analysis yields $C = 0.007074$ with a coefficient of determination of $R^2 = 0.9989$. The curve represents the given data therefore excellently.

The curve that describes the free energy of the self-assembly of block copolymers in a state with many defects is thus:

$$\frac{e}{e_0}(w) = 1 + \frac{32.76}{w} + 0.007074 \qquad (2A.24)$$

To fulfil the objective of this work and to find an expression that helps us predict, in which morphology the block copolymer self-assembles as a function of the trench width w, we will have to take a look at the energy difference between the two models denoted $\frac{\Delta e}{e_0}$, which is defined as follows:

$$\frac{\Delta e}{e_0} = \frac{e_T}{e_0} - \frac{e}{e_0} = \min\left\{\frac{1}{3}\left(\left(\frac{w}{n_0*L_0}\right)^2 + \frac{2*n_0*L_0}{w} + \frac{2*\Gamma*L_0}{w}\right)\right\}_{n_0=\in\{1;j\}} - \left\{1 + \frac{32.76\ nm}{w} + 0.007074\right\} \qquad (2A.25)$$

This function is plotted in *figure 2A.4 d)* for the trench width $w = \{23.4\ nm;\ 200\ nm\}$ and $n = \{1;9\}$. Whenever the free energy of Turner's model is larger than the free energy of the model that we have developed here, the function is positive, which predicts that the block copolymer self-assembles in defect-free lamellar morphology. For those trench

widths where $\frac{\Delta e}{e_0}(w) > 0$, the block copolymer self-assembles with a large number of defects. The light blue box represents those trench widths that have been experimentally accessible for us. The yellow boxes indicate those trench widths, where the defect-loaded state is energetically preferable. These areas become consistently narrower and disappear for trench widths larger than 130 nm. On a molecular basis this is mainly due to the fact that upon stretching, the energy required to stretch a molecular chain increases in a quadratic manner. For this reason, in case of an incommensurable trench, the energy penalty is smaller if the system must stretch many chains a little bit, than if it has to stretch few chains a lot.

2A.4.8 Free energy contributions under confinement

Let us now understand which energy contributions play a role in the two models that we work with in this *chapter*. This will also help us deepen the understanding of the parameter *C*, i.e. $\frac{e_p}{e_0}$ This is a good opportunity to bear in mind, that in neither one of the models we included the interface energy contributions between the substrate and the block copolymer, and the surface tension of the block copolymer. As the two models we investigate are a form of upright-standing lamellae (even though the one has defects), the two contributions are considered to be the same for both models.

Turner's model takes chain stretching (e_S), the inter-block interface (e_{AB}) and the block-wall interaction (e_{AW}) into account (see *formula 2A.19*). The energy contributions of the chain stretching and inter-block interface in bulk conditions $(e_{S,L0};\ e_{AB,L0})$ can be understood as the sum of a bulk condition contribution $(e_{S,L0}+e_{AB,L0} = e_0)$. Moreover, two additional contributions account for the stretching (/compression) $(e_{S,\lambda})$ and the resulting reduction (/increase) of interfaces $(e_{AB,L0})$ due to the incommensurability λ.

$$\frac{e_T}{e_0} = \frac{e_S + e_{AB} + e_{AW}}{e_0}$$
$$= \frac{(e_{S,L0}+e_{S,\lambda}) + (e_{AB,L0}+e_{AB,\lambda}) + e_{AW}}{e_0} = \frac{e_0 + e_{S,\lambda} + e_{AB,\lambda} + e_{AW}}{e_0} \qquad (2A.26)$$

The respective energy contributions are sketched in *figure 2A.8*. From this plot we learn that a great proportion of the free energy of the system originates from the bulk free energy $e_{S,L0} + e_{AB,L0} = e_0$ (blue curves, where $e_{S,L0} = {}^1/_3$ *and* $e_{AB,L0} = {}^2/_3$).

Another important, but strictly monotonically declining part of the free energy comes from the interaction of the A block (i.e. *PMMA*) and the wall (green curve). The characteristic ${}^1/_w$-dependence of this curve can be explained by the fact that wall free energy E_{PMMA-W}, is not a function of the trench width, but rather equivalent to $2 * A * \gamma_{PMMA-W}$. In this equation, *A* stands for the area of the guiding pattern wall which is in contact with the *PMMA* block and γ_{PMMA-W} is the respective interface free energy. As

the trench width increases, this energy contribution is to be distributed among a consistently increasing number of chains. For an infinitely wide trench, this energy would be zero.

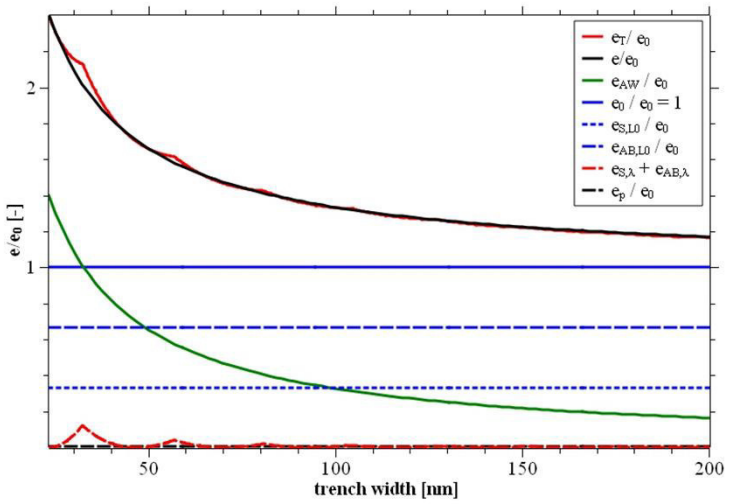

Figure 2A.8: Different energy components that contribute to the calculation of the free energy according to Turner and according to the model derived in this work.

The characteristic spikes in Turner's curve originate from additional increase in stretching and interface energy due to the incommensurability ($e_{S,\lambda}+e_{AB,\lambda}$) with the trench. It is only natural that this curve is always positive, because the bulk free energy is defined as the minimum free energy, so that any deviation from the equilibrium point at L_0 leads to an energy penalty. Here, we only plot the sum of both contributions represented through the red dashed line. The interface energy term, however, becomes negative in case of chain stretching, because the density of interface areas is reduced. In case of a chain compression, the interface energy term is positive, because the density of interfaces is reduced. This effect is the principle source of the different moduli for block copolymer compression and stretching.

Based on that, let us now repeat this analysis for the model we have developed to describe the defect loaded system. Exactly like Turner's model, our analysis takes the bulk energy as a starting point and analyzes the energetic deviation of the system from the bulk energy. Therefore, we include both the bulk free energy ($e_{S,L0}+ e_{AB,L0} = e_0$) and the wall interaction energy e_{AW} exactly like in the previous section. In contrast to that, our approach does not take the stretching of chains and the change in interface energy due to incommensurability ($e_{S,\lambda} + e_{AB,\lambda}$) into consideration, and replaces it by a constant penalty term $\frac{e_P}{e_0}$. This term primarily accounts for the increase in free energy due to the creation

of defects. Here, the term "defect" refers both to the formation of wiggling and to the formation of point-defect like artifacts in crossover from *n* domains to *n+1* domains.

$$\frac{e}{e_0} = \frac{e_{S,L0} + e_{AB,L0} + e_{AW} + e_P}{e_0} = \frac{e_0 + e_{AW} + e_P}{e_0} \qquad (2A.27)$$

If we now subtract *formula 2A.27* from *formula 2A.26*, we determine out that $\frac{\Delta e}{e_0}$ (plotted in *figure 2A.4 d)*) can also be written as:

$$\frac{\Delta e}{e_0} = \frac{(e_{S,\lambda} + e_{AB,\lambda}) - e_P}{e_0} \qquad (2A.28)$$

This confirms once again, but on a more general level, that our results are independent from the interaction energy of the block copolymer and the guiding pattern wall, and are therefore not a function of *Γ*. This finding is well recieved, given the fact that one of the major sources of uncertainty of our method is the estimation of *Γ*.

Previously, we have found that $\frac{e_P}{e_0} = 0.00704$ which corresponds to a value of 0.704 % of e_0.

To set this value in a relation, let us now calculate the bulk free energy per chain as proposed by Ohta and Kawasaki [38,43] normalized to *kT*, which is given by:

$$\frac{e_0}{kT} = \frac{3}{8} * \frac{L_0^2}{N*a^2} + \frac{2*N*a}{L_0} * \sqrt{\frac{\chi}{6}} = 2.99 \qquad (2A.29)$$

In this calculation, we set the block copolymer periodicity $L_0 = 23.4\ nm$, the polymerization $N = 424$ and the Flory-Huggins interaction parameter $\chi = 0.037$ [44]. For the determination of the average Kuhn segment length *a* of our block copolymer, we use $a = 6.6\ Å$ [45].

Based on this calculus we estimate that

$$e_p = 0.00704 * e_0 = 0.021\ kT \qquad (2A.30)$$

We can thus conclude that the additional energy induced in the system compared to the bulk energy quantitatively only accounts for a relative small fraction of the total free energy of the system. Seen it the other way around, the energy difference per chain between the defective and the non-defective state in the directed self-assembly in topographical guiding patterns is even at the point of maximum free energy difference for perfectly commensurate guiding patterns characterized by an energy penalty of a small fraction of kT. The value we estimate here is in surprisingly good agreement with the energy difference other authors have calculated for the defective and the non-defective state in the directed self-assembly of block copolymers in chemical guiding

patterns [46]. This very small quantity demonstrates that the directed self-assembly of block copolymers relies on the system to accommodate to state that has a very small energy advantage with respect to other states, that are lithographically not useful.

2A.5 Conclusions

We have shown that EUV-IL brings the possibility of manufacturing highly accurate topographical guiding patterns for the directed self-assembly of block copolymers. EUV-IL combines high resolution, low line edge roughness and high throughput, which makes it an advantageous method compared to other lithography approaches. We have demonstrated the alignment of patterns of *PS-b-PMMA* of 11.7 nm pitch in perfectly vertical lamellae when a neutral brush layer is grafted to the bottom of the trenches.

We have taken advantage of the accurate control of the dimensions of the guiding patterns that EUV-IL can achieve to investigate the creation of defects as a function of the trench width while minimizing the influence of defects due to guiding pattern imperfections. We conclude that the maximum stretch/compression that the block copolymer chain can sustain is 8 % of the of the chain length in free surface. We extend the commonly used free energy models by adding the description of free energy of the self-assembly morphology that includes defects. The model successfully predicts the window of the pattern process observed experimentally.

To conclude, the experimental proof of the advantage of using EUV-IL for creation of guiding patterns in directed self-assembly of block copolymers, together with the methodology to predict the process window that provides aligned patterns without defects, will help to design process conditions for DSA using new materials, and in particular high-χ materials, to reliably obtain sub-10 nm resolution patterns.

2A.6 References

[1] Päivänranta B, Langner A, Kirk E, David C and Ekinci Y 2011 Sub-10 nm patterning using EUV interference lithography *Nanotechnology* **22** 375302-1-375302–7

[2] Fan D 2016 Photolithography reaches 6 nm half- pitch using extreme ultraviolet light *J. Micro/Nanolith. MEMS MOEMS.* **15** 033505-1-033505-7

[3] Mojarad N, Gobrecht J and Ekinci Y 2015 Interference lithography at EUV and soft X-ray wavelengths: Principles, methods, and applications *Sci. Rep.* **143** 55–63

[4] Cheng H, Keen I, Yu A and Blakey I 2012 EUVL compatible LER solutions

using functional block copolymers *Proc. SPIE* **8323** 1O–1–11

[5] Nickmans K, Murphy J N, Waal B De, Leclère P, Doise J, Gronheid R, Broer D J and Schenning A P H J 2016 Sub-5 nm Patterning by Directed Self-Assembly of Oligo (Dimethylsiloxane) Liquid Crystal Thin Films *Adv. Mater.* **28** 10068–72

[6] Edwards B E W, Montague M F, Solak H H, Hawker C J and Nealey P F 2004 Precise Control over Molecular Dimensions of Block-Copolymer Domains Using the Interfacial Energy of Chemically Nanopatterned Substrates *Adv. Mater.* **16** 1315–9

[7] Kim S O, Solak H H, Stoykovich M P, Ferrier N J, De Pablo J J and Nealey P F 2003 Epitaxial self-assembly of block copolymers on lithographically defined nanopatterned substrates. *Nature* **424** 411–4

[8] Roberts J M, Bacuita T, Bristol R L, Cao H B, Chandhok M, Lee H, Panning E M, Shell M, Zhang G and Rice B J 2005 One small step: World's first integrated EUVL process line *Proc. SPIE* **5751** 64–77

[9] Keen I, Cheng H, Yu A, Jack K S, Younkin T R, Leeson M J, Whittaker A K and Blakey I 2014 Behavior of Lamellar Forming Block Copolymers under Nanoconfinement: Implications for Topography Directed Self- Assembly of Sub-10 nm Structures *Macromolecules* **47** 276–83

[10] Gronheid R, Boeckx C, Doise J, Karageorgos I, Ryckaert J, Chan B T, Lin C and Zou Y 2017 EUV Patterned Templates with Graphoepitaxy DSA at the N5/N7 Logic Nodes *Proc. SPIE* **9776** 1W–1–9

[11] Chi C, Liu C, Meli L, Guo J, Parnell D, Mignot Y, Schmidt K, Sanchez M, Farrell R, Singh L, Furukawa T, Lai K, Xu Y, Sanders D, Hetzer D, Metz A, Burns S, Nelson F, Arnold J and Corliss D 2017 Electrical Study of DSA shrink process and CD rectification effect at sub-60nm using EUV test vehicle *Proc. SPIE* **10146** Q1–8

[12] Junarsa I, Stoykovich M P, Nealey P F, Yyuansheng M and Solak H H 2005 Hydrogen silsesquioxane as a high resolution negative-tone resist for extreme ultraviolet lithography *J. Vac. Sci. Technol. B* **23** 138–43

[13] Chen W, Luo J, Shi P, Li C, He X, Hong P, Li J and Zhao C 2014 Self-assembling morphologies of symmetrical PS b-PMMA in different sized confining grooves *RSC Adv.* **4** 50393–400

[14] Borah D, Rassapa S, Shaw M T, Hobbs R G, Petkov N, Schmidt M, Holmes J D and Morris M 2013 Directed self-assembly of PS-b-PMMA block copolymer using HSQ lines for translational alignment *J. Mater. Chem. C* **1** 1192–6

[15] Mojarad N, Gobrecht J and Ekinci Y 2015 Beyond EUV lithography: A comparative study of efficient photoresists' performance *Sci. Rep.* **5** 1–7

[16] Kim B, Laachi N, Delaney K T and Fredrickson G H 2014 Directed self-

assembly of diblock copolymers in laterally confining channels: line-edge-roughness and defectivity *Proc. SPIE* **9049** 1D–1–9

[17] Park B S, Stoykovich M P, Ruiz R, Zhang Y, Black C T and Nealey P F 2007 Directed Assembly of Lamellae-Forming Block Copolymers by Using Chemically and Topographically Patterned Substrates *Adv. Mater.* **19** 607–11

[18] Tsai H, Pitera J W, Miyazoe H, Bangsaruntip S, Engelmann S U, Liu C C, Cheng J Y, Bucchignano J J, Klaus D P, Joseph E A, Sanders D P, Colburn M E and Guillorn M A 2014 Two-dimensional pattern formation using graphoepitaxy of PS-b-PMMA block copolymers for advanced FinFET device and circuit fabrication *ACS Nano* **8** 5227–32

[19] Cummins C, Bell A and Morris M 2017 Creating Active Device Materials for Nanoelectronics Using Block Copolymer Lithography *Nanomaterials* **7** 304

[20] Caster A G, Kowarik S, Schwartzberg A M, Nicolet O, Lim S and Leone S R 2009 Observing hydrogen silsesquioxane cross-linking with broadband CARS *J. Raman Spectrosc.* **40** 770–4

[21] Solak H H, David C, Gobrecht J, Golovkina V, Cerrina F and Kim S O 2003 Sub-50 nm period patterns with EUV interference lithography **68** 56–62

[22] Claveau G, Hazart J, Posseme N, Chevalier X, Claveau G, Quemere P, Argoud M, Hazart J, Barros P P, Sarrazin A, Posseme N, Tiron R, Chevalier X, Nicolet C and Navarro C 2016 Surface affinity role in graphoepitaxy of lamellar block copolymers *J. Micro/Nanolithography, MEMS, MOEMS* **15** 031604-1–11

[23] Sun Y, Wang C and Liou J 2016 Tuning polymer-surface chemistries and interfacial interactions with UV irradiated polystyrene chains to control domain orientations in thin films of PS- b -PMMA *Soft Matter* **12** 2923–31

[24] Bartnik H, Fiedorowicz A, Jarocki R, Kostecki R J and Szczurek M 2010 PMMA and FEP surface modifications induced with EUV pulses in two selected wavelength ranges *Appl. Phys. A* **98** 61–5

[25] Mansky P, Liu Y, Huang E, Russell T P and Hawker C 1997 Controlling Polymer-Surface Interactions with Random Copolymer Brushes *Science.* **275** 1458–60

[26] Erdmann A, Michalak P, Ismail M, Fühner T, Argoud M, Claveau G, Tiron R, Müller M and Cayrefourcq C 2016 Modeling study of 3D morphologies for a line multiplication process *Talk 2nd DSA Symp. Grenoble*

[27] Han B E, Kang H, Liu C, Nealey P F and Gopalan P 2010 Graphoepitaxial Assembly of Symmetric Block Copolymers on Weakly Preferential Substrates *Adv. Mater.* **22** 4325–9

[28] Turner M S 1992 Equilibrium Properties of a Diblock Copolymer Lamellar Phase Confined between Flat Plates *Phys. Rev. Lett.* **69** 1788–91

[29] Takahashi H, Laachi N, Delaney K T, Hur S, Weinheimer C J, Shykind D and

Fredrickson G H 2012 Defectivity in Laterally Con fi ned Lamella-Forming Diblock Copolymers : Thermodynamic and Kinetic Aspects *Macromolecules*

[30] Wang Z-G G 1994 Response and instabilities of the lamellar phase of diblock copolymers under uniaxial stress *J. Chem. Phys.* **100** 2298–309

[31] Delaye M, Ribotta R and Durand G 1973 Buckling instability of the layers in a smectic-A liquid crystal *Phys. Lett. A* **44** 139–40

[32] Ruiz R, Ruiz N, Zhang Y, Sandstrom R L and Black C T 2007 Local Defectivity Control of 2D Self-Assembled Block Copolymer Patterns *Adv. Mater.* **19** 2157–62

[33] Hur S-M, Thapar V, Ramírez-Hernández A, Khaira G, Segal-Peretz T, Rincon-Delgadillo P A, Li W, Müller M, Nealey P F and de Pablo J J 2015 Molecular pathways for defect annihilation in directed self-assembly *Proc. Natl. Acad. Sci.* **112** 14144–9

[34] Cohen Y, Albalak R J, Dair B J, Capel M S and Thomas E L 2000 Deformation of oriented lamellar block copolymer films *Macromolecules* **33** 6502–16

[35] Read D J, Duckett R A, Sweeney J and McLeish T C B 1999 Chevron folding instability in thermoplastic elastomers and other layered materials *J. Phys. D. Appl. Phys.* **32** 2087–99

[36] Makke A, Perez M, Lame O and Barrat J-L 2012 Nanoscale buckling deformation in layered copolymer materials *Proc. Natl. Acad. Sci.* **109** 680–5

[37] Cheng J O Y Y, Mayes A M and Ross C A 2004 Nanostructure engineering by templated self-assembly of block copolymers *Nat. Mater.* **3** 823–8

[38] Walton D, Kellogg G J, Mayes A, Lambooy P and Russell T P 1994 A Free Energy Model for Confined Diblock Copolymers *Macromolecules* **27** 6225–8

[39] Owens D K and Wendt R C 1969 Estimation of the Surface Free Energy of Polymers *J. Appl. Polym. Sci.* **13** 1741–7

[40] Carriere C J and Sammler R L 2000 Temperature dependence of the interfacial tension of PS/PMMA , PS/PE, and PMMA/PE blends *Rheol. Acta* **39** 476–82

[41] Suzuki T and Yamada Y 2015 Dispersion and Polar Component of Specific Surface Free Energy of NaCl (100), KCl (100), and KBr (100) Single Crystal Surfaces *J. Cryst. Process Technol.* **5** 43–7

[42] N/A Solid surface energy data (SFE) for common polymers *12/06/18* http://www.surface-tension.de/solid-surface-energy

[43] Ohta T and Kawasaki K 1986 Equilibirum Morphology of Block Copolymer Melts *Macromolecules* **19** 2621–32

[44] Russell T P, Hjelm R P and Seeger P A 1990 Temperature Dependence of the Interaction Parameter of Polystyrene and Poly (methyl methacrylate) *Macromolecules* **23** 890–3

[45] Helfand E and Tagami Y 1971 Theory of the interface between immiscible

polymers *Polym. Lett.* **9** 741–6

[46] Garner G P, Rincon Delgadillo P, Gronheid R, Nealey P F and De Pablo J J 2017 Design of surface patterns with optimized thermodynamic driving forces for the directed self-assembly of block copolymers in lithographic applications *Mol. Syst. Des. Eng.* **2** 567–80

Chapter 2B:

Directed self-assembly of block copolymers in sub-10 nm topographical guiding patterns

Abstract:

In this chapter we investigate the directed self-assembly of block copolymers in topographical guiding patterns with feature sizes in the range of the block copolymer half-pitch. In particular, we present the self-assembly of an 11.7 nm half-pitch block copolymer in sub-10 nm resolution guiding patterns fabricated by the direct e-beam exposure of *hydrogen silsesquioxane* (*HSQ*). One result of this analysis is that the block copolymer self-assembles in such a way that the guiding pattern features form part of the 3-D architecture of the film. We are capable of determining a shift in the block copolymer pitch as a function of the guiding pattern pitch with sub-nanometer accuracy by means of both real-space imaging techniques (AFM, SEM) and reciprocal-space imaging techniques (GISAXS). An interesting, result is that the block copolymer self-assembly in the studied structures depends on the guiding pattern pitch rather than on the trench width as in standard graphoepitaxy.

The extended free energy model we have developed in *chapter 2A* is successfully adjusted for the system we discuss in this chapter.

Table of contents: Chapter 2B

2B.1 Introduction

The fabrication of chemical guiding patterns requires patterning techniques with excellent resolution because the chemically modified areas need to be in the size range of the block copolymer domains. Works concentrating on very high-resolution topographical guiding patterns are, in turn, sparse [1]. This may be because one of the principal advantages of the use of graphoepitaxy [2] is the low required resolution for the guiding pattern fabrication.

Nevertheless, investigating the behavior of block copolymers in high-resolution topographical guiding patterns is of technological interest for at least two reasons. On one hand, the need for high-resolution topographical guiding patterns will increase substantially as soon as new high-χ block copolymers or other self-assembling materials with significantly smaller pitches are developed [3]. On the other hand, the space on the chip occupied by guiding pattern features represents non-utilizable space for the fabrication of electronic devices on the chip. Therefore, the use of high-resolution topographical guiding patterns represents a noticeable increase in patterning efficiency with respect to systems using large guiding pattern features. To our best knowledge there is no work published that analyzes the behavior of block copolymers in topographical guiding patterns whose critical feature size has been pushed below the block copolymer domain size.

Besides standard real-space nanocharacterization methods like SEM and AFM, in this *chapter*, we rely on the use of grazing-incidence small-angle X-ray scattering (GISAXS), which is a destruction-free contact-less characterization technique frequently used to analyze the nanostructure of polymer films [4]. A significant advantage of GISAXS over common real-space techniques is that the relatively large sampling volume permits the investigation of a statistically meaningful area both on the sample surface and below [5]. Low incidence angles (usually few tenths of degrees), however, lead to significantly elongated beam foot prints. In the last years GISAXS has been used to analyze gratings to determine their basic geometric properties [6], but also more advanced parameters like the line-edge-roughness [7].

In this chapter we report on the self-assembly of a 23.4 nm full-pitch lamellar diblock *PS-b-PMMA* block copolymer with a low defect-density in sub-10 nm resolution topographical guiding patterns fabricated by the direct exposure of *HSQ* to an electron beam. The material is found to exhibit a self-assembly morphology that is different from the one observed for the directed self-assembly of block copolymers in wide guiding patterns (as for example discussed in *chapter 2A*), which we confirm by GISAXS, SEM and AFM measurements. We apply a free-energy model and compare the fabricated

structures with regard to the free energy difference between the defect-free self-assembly and the defective self-assembly.

2B.2 Experimental

The substrates used in the experiments are pieces of 2 x 2 cm^2 cleaved from a p-doped <100> oriented *silicon* wafer (4-40 Ω cm resistance).

2B.2.1 HSQ deposition, exposure and development

The chip is cleaned in an O_2 plasma at 100 W for 20 s. We used flowable oxide FOX 16 by Dow Corning Corporation diluted 1:6 in *methyl isobutyl ketone (MIBK)* and spin coated this solution at 1000 rpm for 1 min. This yields a film thickness of 42 nm. The exposure of *HSQ* by electron beam induces a cross-linking process [8–11], which converts the exposed areas into an SiO_2-like amorphous material.

The exposure takes place with *Vistec EBPG 5000+* tool using a 100 kV electron beam with a beam current of 2 nA. The exposure dose for the fabrication of sub-10 nm lines varies from 7400 $^{\mu C}/_{cm^2}$ to 8800 $^{\mu C}/_{cm^2}$ as a function of the pattern pitch, which in this work is between 80 nm and 250 nm. The patterns are 512 µm wide and 10 mm long.

After the exposure the non-cross-linked *HSQ* is removed in a development step using an alkaline developer (*Microposit 351 diluted 1:3 in water*) for 5 min. Subsequently the sample is dipped in H_2O for one minute and air-dried.

2B.2.2 Deposition of neutral brush layer

A neutral brush layer is spun from a 0.25 wt% solution of *PS-r-PMMA* (58 wt% *PS* and 42 wt% *PMMA* at a molecular weight $M_{brush} = 7.9\ ^{kg}/_{mol}$ and a polydispersity index $PDI_{brush} = 1.85$) dissolved in *PGMEA*. The spin coating conditions are 4000 rpm for 30 s, leading to a film thickness of 4 nm in free surface. An annealing step at 230 ºC for 5 min initiates a grafting process of the random copolymers to the activated *silicon* surface. The non-grafted brush layer is removed by a *PGMEA* rinsing step.

2B.2.3 Deposition and self-assembly of block copolymers

All the experiments in this work are done with a lamellar *PS-b-PMMA* diblock copolymer ($M_{PS\text{-}b\text{-}PMMA} = 42.3\ ^{kg}/_{mol}$; 43 wt% *PS*, 57 wt% *PMMA*, $PDI_{BCP} = 1.1$). The natural pitch in free surface is 23.4 nm. Spin-coating of a 1.8 wt% solution in *PGMEA* at 2000 rpm yields a 34 nm thick film in free surface. Microphase separation is induced by an annealing step at 230 ºC for 10 min.

2B.2.4 Analysis

The samples are inspected by tapping mode AFM using the *Dimension Icon / Nanoscope V* by *Bruker*. The amplitude set-point is 50 % of the drive amplitude. The SEM inspection is done with a *Zeiss Auriga* using the *InLens* detector. GISAXS, using synchrotron radiation, of representative samples are conducted at the P03 Micro- and Nanofocus X-Ray Scattering Beamline at PETRA III in Hamburg, Germany [12]. The sample-detector distance is set to $L = 5800\ mm$ and the radiation wavelength to $\lambda = 0.107\ nm$. The incidence angle of the beam is $\alpha_i = 0.4^o$. The detector that has been used for these experiments is a PILATUS 300k pixel detector with a readout time below 3 ms and a pixel size of 172 µm x 172 µm.

The estimated uncertainty in lateral size determination according to the procedure proposed by Smilgies [13] is 0.3 nm. Here, the most important contribution to the measurement uncertainty originates from the beam divergence, while the contribution of the beam band width and geometric smearing only contribute to a negligible extend.

2B.3 Results

In the following, we compare the typical graphoepitaxy work-flow characterized by relatively large guiding pattern features with a work-flow where the guiding pattern features have been minimized to sub-10 nm size.

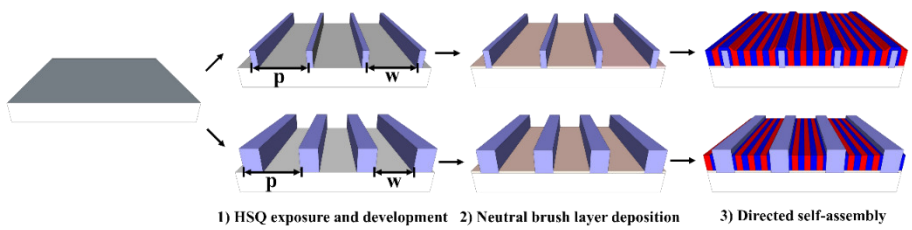

Figure 2B.1: Sketches comparing the self-assembly morphology in topographical guiding patterns with sub-10 nm guiding pattern width (top part) with the self-assembly morphology in guiding patterns with a width significantly above 10 nm (bottom part). In both rows the parameter p indicates the guiding pattern pitch, and w the separation between the guiding pattern features, so that the trench width is p-w.

The work-flow pursued to fabricate the guiding patterns is depicted in the top part of *figure 2B.1* and compared to wide guiding pattern fabrication work-flow, which is sketched in the bottom part of the same *figure*. The principal difference between the two work-flows is in the guiding pattern feature width. The work-flow sketched in the top images is characterized by a guiding pattern feature width below 10 nm, which is in the

size range of the block copolymer domain. The lower row of images, in turn depicts a work-flow using guiding patterns with a feature width significantly above the block copolymer domain size. For both alternatives it is particularly important to deposit a thin 4 nm neutral brush layer to avoid grafting of random copolymers to the guiding pattern walls, because otherwise the self-assembly morphology would no longer be lamellar parallel to the guiding pattern direction, but rather convert into lamellae perpendicular to the guiding pattern direction (see *chapter 2A* and ref. [1]). The fundamentally different self-assembly morphologies originate from differences in the guiding pattern width. The origin of this difference is depicted in *figure 2B.1* and explained in the forthcoming paragraphs.

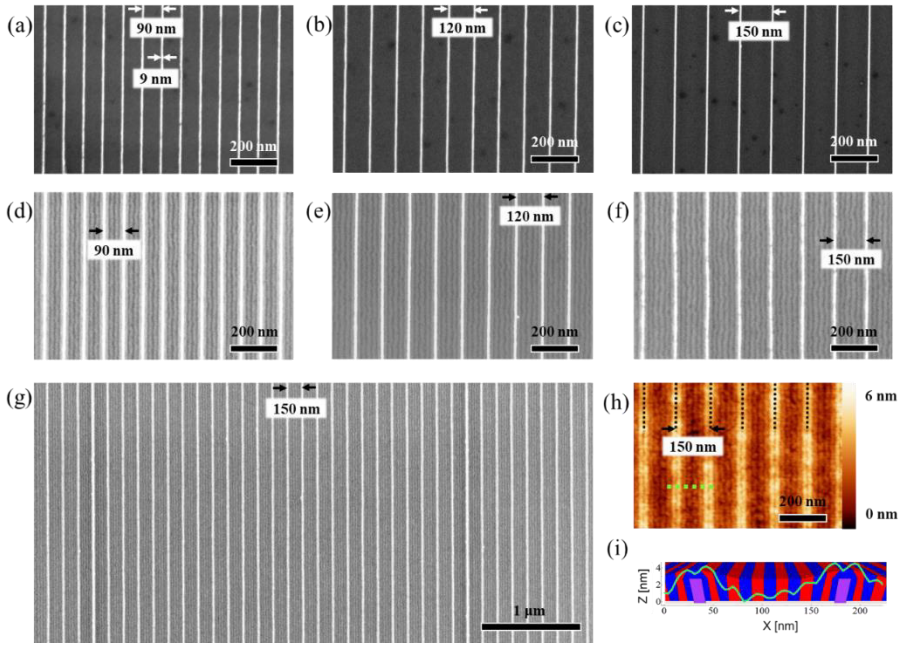

Figure 2B.2: SEM images of patterns with different pitches before and after self-assembly. a) - c): SEM images of 90 nm, 120 nm, 150 nm guiding patterns, d) - f): SEM images of 90 nm, 120 nm, 150 nm guiding patterns with self-assembled block copolymer, g): SEM image of defect-free assembly on large scale, h): AFM height image of the 150 nm structure, i): single line scan along the green dotted line in h) with a sketch of the self-assembly morphology in the background.

2B.3.1 Directed self-assembly characterization by real-space imaging

On the forthcoming pages, we analyze results obtained using sub-10 nm guiding pattern with nominal pitches of 90 nm, 120 nm and 150 nm, as depicted in the *figures 2B.2 a)-c)*. The SEM images depicted in *figure 2B.2 d)-f)* demonstrate the excellent ability of the guiding patterns to direct the self-assembly of block copolymers. The guiding patterns

are capable of directing the self-assembly of block copolymers without the formation of defects over areas of various tens of square micrometers. The example shown in *figure 2B.2 g)* is an SEM image that demonstrates the defect-free self-assembly in trenches with a 150 nm pitch. The multiplication factor is $n = 6$ for this pattern. That means that the density of the block copolymer features in this pattern is six times higher than the guiding pattern feature density.

Figure 2B.2 h) represents a tapping mode AFM height image of the 150 nm pattern after DSA. Interestingly, we observe that the entire surface is a sequence of *PS* and *PMMA* domains, indicating that the guiding pattern features are entirely covered by block copolymer molecules. Based on our observations, we conclude that the block copolymer surrounds the guiding pattern features rather than occupying exclusively the space between the features, as it is the case for wide guiding patterns (see sketch in *figure 2B.2 i)*). A similar self-assembly morphology has been observed in a study analyzing the directed self-assembly of block copolymers based on a chemoepitaxy-graphoepitaxy hybrid process [14] , however, other than in the present study, only with a few nanometers of topography [15,16]. It is, moreover, well known that the cross-linked *HSQ* is preferentially wetted by *PMMA* [17,18]. Based on that, we conclude that the recessed line in the middle of the area above the guiding patterns indicated by the black dashed lines corresponds to *PMMA*. It is known that the exposure of *PS* with ionizing radiation promotes cross-linking [19], while it leads to the degradation of *PMMA* [20]. The results presented in ref. [21] confirm these findings for GISAXS experiments that have been conducted under conditions that are very similar to the ones used in our experiments. The complete degradation / cross-linking of *PS* and *PMMA* thin films is in the range of various tens of seconds. Since the accumulated exposure time per guiding pattern in our experiment is well below 5 s, we expect the respective cross-linking / degradation process to have started, but by far not to be completed.

Another interesting observation we make concerns the different degrees of visibility of the guiding patterns in the AFM height image compared to the SEM image. Although the AFM analysis reveals that the guiding patterns are entirely covered with block copolymers, the guiding pattern lines, produce a strong SEM signal. This observation suggests that the block copolymer layer covering the guiding patterns is only few nanometers thick. The coverage of the guiding pattern thus results most likely from an energy minimization process during the self-assembly.

These observations confirm the self-assembly morphology depicted in *figure 2B.1* and demonstrate that the self-assembly in these patterns differs significantly from the directed self-assembly when the guiding pattern feature width is notably larger than the block copolymer domain.

2B.3.2 Analysis of the structures with GISAXS

An important parameter for the understanding the behavior of block copolymers under confinement is the strain / compression with respect to their equilibrium spacing L_0 which can be determined by measuring the block copolymer pitch. Although we get an excellent qualitative understanding of how the block copolymers self-assemble in our system, it is difficult to determine deviations in the block copolymer pitch with high accuracy by the exclusive use of real-space techniques.

For this reason, we conduct GISAXS measurements to study the block copolymer pitch as a function of the guiding pattern pitch. The geometry of the GISAXS experiment is sketched in *figure 2B.3 a).* The samples depicted in *figure 2B.2 a)-f)* have been analyzed by GISAXS. The elongated shape of the guiding pattern (512 µm x 10 mm) is necessary to avoid that a large part of the measured signal originates from block copolymers oriented in fingerprint morphology. At the chosen incidence angle of 0.4 º, the 50 µm beam has a footprint of slightly more than 7 mm in length, which is shorter than the pattern length and therefore allows us to detect scattered photons originating exclusively from the block copolymer in the guiding pattern.

The GISAXS measurement of the samples with guiding patterns before the deposition of block copolymer shows the characteristic scattering features for such gratings [6]. The patterns depicted in *figures 2B.3 b)-d)* represent the results of the analysis of the guiding patterns with a nominal pitch of 90 nm, 120 nm and 150 nm. The GISAXS patterns consist of a superposition of the Ewald sphere leading to an arc, and a number of grating truncation rods (GTRs), whose separation indicates the pitch of the real space lattice in reciprocal space. We can easily extract the lattice pitch with the Bragg equation, which yields a pitch $p_1 = 89.9 \pm 0.3$ *nm* for *figure 2B.3 b)*, $p_2 = 120.3 \pm 0.3$ nm for *figure 2B.3 c)* and $p_3 = 150.1 \pm 0.3$ nm for *figure 2B.3 d)*. These values are mean values of the position of two GTRs in each pattern and demonstrate the excellent precision of the guiding pattern fabrication.

The semicircular shape of the intersection of the Ewald sphere with the detector is very sensitive to the orientation of the pattern with respect to the incident beam [22,23]. The nearly perfectly semicircular shape of the arc in the observed pattern suggests a deviation from perfect parallelism of merely few thousandths of a degree. The semicircle has its center in the sample horizon (at $\alpha = 0^o$; $\omega = 0^o$) and its radius corresponds to the incidence angle of the beam [24].

In *figure 2B.3 e)-g)* we depict the scattering patterns of block copolymers after the directed self-assembly. In comparison to the measurements shown before, these patterns show a number of scattering effects in addition to the GTRs and the semicircle we observe

in the guiding pattern. These scattering features are consequently due to the self-assembled block copolymer. In general terms, the signal intensity in the patterns decreases notably after the deposition of the block copolymer. The reason for this effect is that the scattering probability at the interface between two materials is proportional to the difference in their electron density. The difference in the electron density between air and SiO_2 in case of the guiding pattern sample, is larger than the difference in electron density between the SiO_2 and block copolymer. In each GISAXS pattern there is one GTR that stands out of the rest due to its enhanced intensity. For *figure 2B.3 e)*, the high-intensity GTR can be found in the 4th order, for *figure 2B.3 f)*, in the 5th order and for *figure 2B.3 g)* in the 6th order GTR. While this effect is important in the GISAXS pattern of the 90 nm grating, it is rather weak in the 120 nm and the 150 nm grating. An important conclusion from this observation is that the order of the GTR that shows this phenomenon corresponds to the multiplication factor *n* we observed in the SEM and AFM analysis of our structures *(figure 2B.2)*. Additional features that distinguish the GISAXS patterns after block copolymer deposition from those before deposition is the existence of satellite arcs that other authors have previously interpreted as a result of line edge roughness in the analyzed pattern [25] but will not be made a further subject of discussion in this paper. Finally, we notice an intensity modulation in the range of $\alpha = \{0.1\ º;\ 0.15\ º\}$ which is related to the different material composition of the sample with block copolymer compared to the one without block copolymer [26].

The overall aspect of the GISAXS pattern is similar to those that have been taken from block copolymers directed by chemical guiding patterns [27,28]. In these works, the authors also observe the effect of intensity enhancement of the *n-th* GTR for guiding patterns with a multiplication factor *n*. The similarity between GISAXS measurements of our patterns and on samples with block copolymer self-assembly directed by chemoepitaxy supports our thesis that *(i)* the intensification of determined GTRs is due to the presence of block copolymers, *(ii)* we can draw conclusions about the block copolymer structure based on the position of the intensified GTR and *(iii)* the topographical guiding pattern actually forms part of the 3D morphology of the block copolymer pattern.

In the following, we will analyze specific transverse cuts through the GISAXS pattern of the 90 nm pitch grating sample before and after the deposition of block copolymers and in particular investigate the origin of the enhanced intensity of the 4th order GTR.

In *figure 2B.4 a)* we compare cuts at $\alpha = \{0.125º \pm 0.025\}$ (i.e. around the Yoneda peak [26] of the block copolymer constituents) of the guiding pattern (red curve), the guiding pattern with block copolymer (black curve) and a block copolymer in free surface (blue curve). Small versions of the respective patterns are depicted in the panel as in-sets and

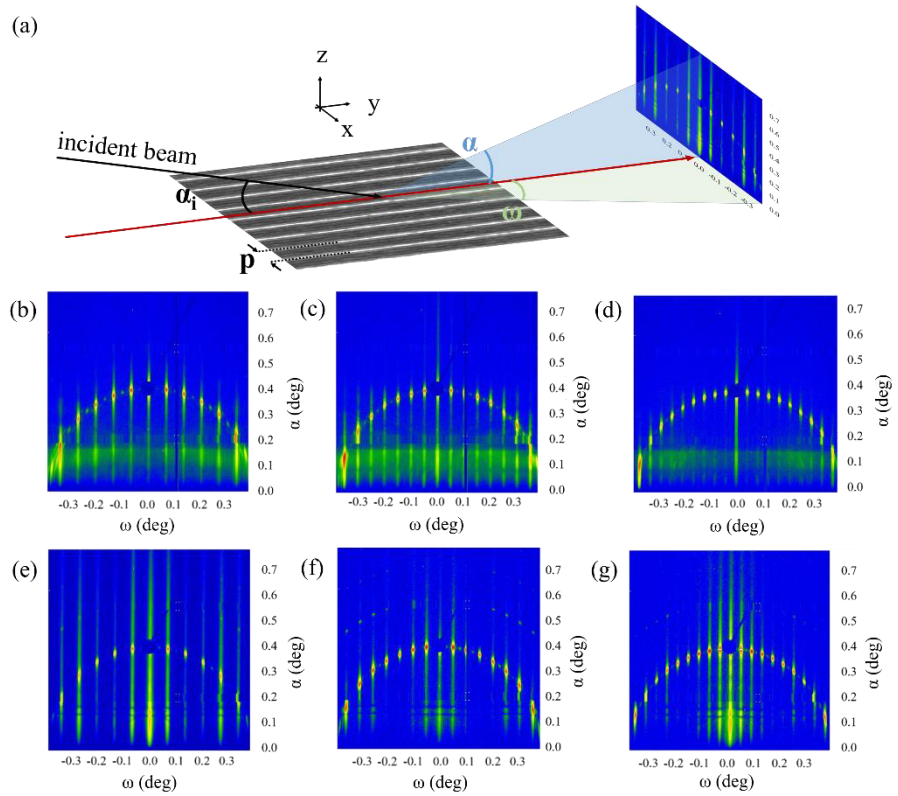

Figure 2B.3: GISAXS analysis of structures with and without block copolymer. a): Geometry of GISAXS experiments, b): GISAXS pattern for 90 nm pitch guiding pattern, c): GISAXS pattern for 120 nm pitch guiding pattern, d): GISAXS pattern for 150 nm pitch guiding pattern, e): GISAXS pattern for 90 nm pitch guiding pattern with self-assembled block copolymer, f): GISAXS pattern for 120 nm pitch guiding pattern with self-assembled block copolymer, g): GISAXS pattern for 150 nm pitch guiding pattern with self-assembled block copolymer.

the approximate position of the cut is indicated by the white dotted line. The color of the respective inset's frame corresponds to the color of the curve.

The GISAXS analysis of the fingerprint pattern sample yields only one peak ($\omega = 0.267°$), that corresponds to the periodicity of the block copolymer pattern. The peak position suggests a natural block copolymer pitch $L_0 = 23.4 \pm 0.3$ *nm*. In addition to that, the block copolymer fingerprint pattern produces a remarkable scattering intensity at small diffraction angles ω, causing a large background intensity in the blue curve. For the black and the red curve, we observe GTRs at the same diffraction angles ω before and after the block copolymer deposition. The absence of a peak at $\omega = 0.267°$ confirms that the amount of illuminated material outside the guiding pattern (i.e. material self-assembled in fingerprint morphology) in this experiment is negligible. Although the overall signal

declines after the deposition of the block copolymer, we observe that the black curve has a background intensity whose shape is very similar to the one measured in the fingerprint sample. This phenomenon seems to be an effect caused by block copolymers and results in the misleading impression that low-order GTRs have a significantly higher scattering intensity than the higher-order GTRs.

The conversion from scattering angle ω into the q-space is done with Bragg's law using

$$q = \frac{4*\pi}{\lambda} \sin(\frac{\omega}{2}) \qquad (2B.1),$$

where the radiation wavelength λ for our experiments is 0.107 nm. In *figure 2B.4 b)* we transform the pattern in the q-space and compare the 3rd and the 4th order GTR of the 90 nm guiding pattern sample after the deposition of the block copolymer. Interestingly, the 4th order GTR needs to be fitted with two Gaussians, while for the 3rd order GTR it is sufficient to fit it with one Gaussian. The center of the two Gaussians (drawn in grey dashed lines) is $q_\alpha = 0.28\ nm^{-1}$ indicating a block copolymer pitch of *22.4 ± 0.3 nm.* For the conversion from q to real space periodicity d, we use

$$d = \frac{2*\pi}{q} \qquad (2B.2).$$

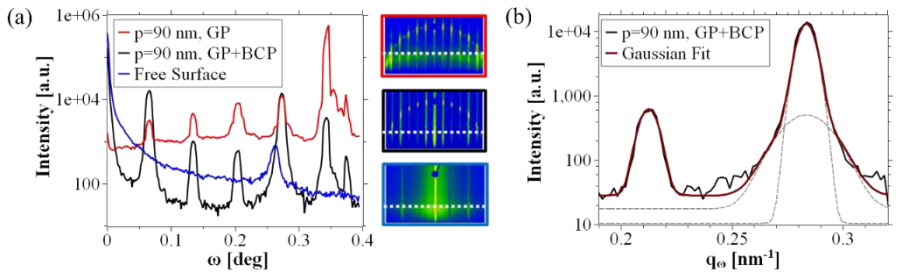

Figure 2B.4: Determination of the block copolymer pitch with sub-nm resolution. a): Cuts through GISAXS patterns depicted at the right at exit angle α = 0.125° ± 0.025° (see white dashed lines and zoomed into the relevant area, b): 3rd order peak of 90 nm pitch guiding pattern peak and its single-peak fit, and 4th order peak of 90 nm pitch guiding pattern and its double peak fit.

Based on this observation, on the AFM/SEM analysis presented in *figure 2B.2* and on the similarity of this system to the chemoepitaxy system analyzed in refs. [27,29], we deduce that this peak represents a superposition of the 4th guiding pattern GTR and the 1st order block copolymer GTR. This implies that the pitch of the block copolymer that is deposited in the 90 nm guiding pattern area differs from its natural pitch $L_0 = 23.4\ nm$ by approximately 4.2 % (corresponding to a pattern compression to 22.5 nm full-pitch). The

distortion of cylindrical block copolymers due to guiding pattern incommensurability has been observed by GISAXS before for minimal topographical guiding patterns [30].

2B.4 Discussion

2B.4.1 Comparison with chemoepitaxy and common graphoepitaxy

So far, it has been common sense that graphoepitaxial guiding patterns have to be designed such that the space between the guiding patterns is exactly or close to an integer multiple of the natural block copolymer pitch [31–35]. These findings are confirmed by the experiments presented in *chapter 2A* of this thesis.

This design rule implies that the successful design of graphoepitaxial guiding patterns depends on the interplay of pattern pitch p and pattern width w_{GP}. Based on the analysis presented in the *results* section of this *chapter*, we conclude that the design rule for the successful alignment of block copolymers in topographical guiding patterns with feature sizes in the range of individual block copolymer domains differs fundamentally from those for wide topographical guiding patterns. Similar to chemoepitaxy, the high-resolution topographical guiding patterns have to be designed such that their pitch (and not the space between the two guiding pattern features) is in the close vicinity of an integer multiple of the block copolymer pitch (see *figure 2B.5 a) – e)*).

A model to describe the normalized free energy of block copolymers under confinement has been developed by Turner [32] and successfully used to describe the self-assembly of block copolymers in topographical guiding patterns [18]. In *chapter 2A*, we have introduced an extension of this model to explain the free energy of a self-assembly morphology with a high defect density as it can also be found in our experiments for strongly incommensurate pitches. In the following, we will estimate the free energy of the block copolymers self-assembled in sub-10 nm guiding patterns using a further extension of the previously found model. Exactly like for guiding patterns with wide guiding pattern features, we observe alternatingly regions with successful self-assembly and regions where the self-assembly shows a large number of defects, which we refer to as defect-loaded state (see *figure 2B. 5 a)*).

Due to incommensurability, the self-assembly in samples with guiding patterns with 80 nm and 110 nm pitch leads to a very large defect density in the block copolymer template (see images in *figure 2B.5 b) / d)*, where images with a red frame represent examples for self-assembly with a large number or defects and images with a green frame represent examples with a defect-free self-assembly). The guiding patterns with 90 nm and 120 nm pitch, in turn, provide a self-assembly morphology free from defects (see *figure 2B.5 c) /*

e)). The basis of the extended model to describe the free energy of laterally confined block copolymers is the *model* derived by Turner to deduce e_T/e_0. Here, e_T is the free energy of one macromolecule confined in a trench of width w in consideration of the deformation free energy, the polymer-wall interaction and the A/B-interfaces, and e_0 corresponds to the free energy per macromolecule under equilibrium conditions. Despite of the differences in pattern feature width, we find that results elaborated for the design of wide guiding patterns are adaptable for the present system if we consider the guiding pattern pitch instead of the trench width as independent variable (note the two different x-axis on top and at the bottom of *figure 2B.5 a)*). For this reason, the trench width w from the original *equation* has been replaced by pattern pitch p to adapt the model corresponding to the present guiding pattern morphology:

$$\frac{e_T}{e_0} = \frac{1}{3}\left(\left(\frac{p}{n*L_0}\right)^2 + \frac{2*n*L_0}{p} + \frac{2*\Gamma*L_0}{p}\right), \qquad \text{(2B.3)},$$

where n is the multiplication factor, L_0 is the block copolymer equilibrium pitch in free surface and Γ is a term representing the interaction between the block copolymer and the guiding pattern features.

We will now add a summand e_D/e_0 to this *equation*, which accounts for the additional free energy introduced into the system due to the distortion of the block copolymer features in the direct vicinity of the top cap of the guiding pattern features, so that the *equation* turns into:

$$\frac{e_{Tt}}{e_0} = \frac{1}{3}\left(\left(\frac{p}{n*L_0}\right)^2 + \frac{2*n*L_0}{p} + \frac{2*\Gamma*L_0}{p}\right) + e_D/e_0 \qquad \text{(2B.4)}.$$

We call the expression e_{Tt}/e_0, because it describes the free energy of the system in thin guiding patterns. With the summand e_D/e_0 we account for the free-energy caused by chain deformation in the self-assembled system that is independent from the incommensurability [14].

The normalized free energy according to Turner in thin guiding patterns (*equation 2B.4*) is now compared with a term that we call e/e_0 and describes the free energy of the system, when it forms defects. This term sums up the normalized free energy in free surface (i.e. 1), the interface free energy contribution due to the interaction between the block copolymers and guiding pattern features (i.e. $2 * \Gamma * L_0/3 * p$) and a constant energy penalty term accounting for an additional free energy contribution (including, for example, the formation of additional interfaces, domain wiggling and chain stretching) called e_p/e_0

$$\frac{e}{e_0} = 1 + \frac{2*\Gamma*L_0}{3*p} + \frac{e_p}{e_0} \qquad (2B.5)$$

Following the reasoning presented in a *chapter 2A*, we can state that the system forms defects, if the term $\Delta e_t/e_0$ defined as

$$\frac{\Delta e_t}{e_0} = \frac{e_{Tt}}{e_0} - \frac{e}{e_0} \qquad (2B.6)$$

is positive, which occurs when Turner's free energy is larger than the free energy of the defective state. If the free energy of the defective state is larger than Turner's free energy (i.e. the result of *equation 2B.6* is negative), the block copolymers omit to form defects and deform to fit the guiding pattern dimensions.

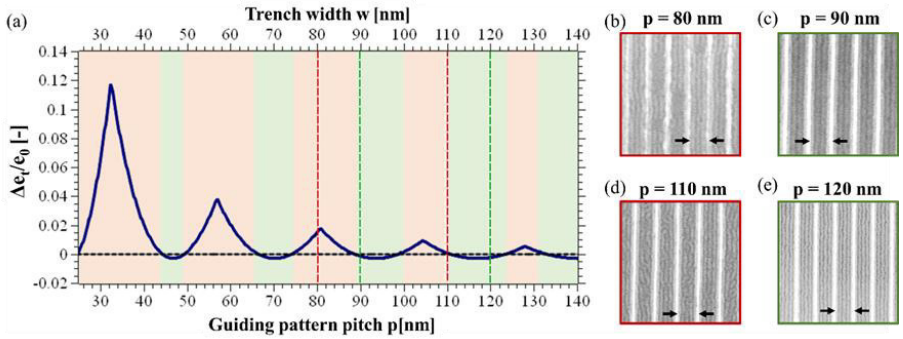

Figure 2B.5: Adaption of graphoepitaxy free energy model of chapter 2A to describe the self-assembly behavior of block copolymers in high-resolution guiding patterns. We observe a reduction of the process window for the fabrication of high-resolution guiding patterns with respect to wide guiding patterns.

We determine a distortion parameter that we call e_D. The determination of e_D is based on the assumption that the penalty term e_P (in chapter 2A and ref. [31] estimated to be approximately 0.007 for the self-assembly of *PS-b-PMMA* in wide guiding patterns) is valid for all the macromolecules in this system that are not subject to distortion in the close vicinity of the top cap of the guiding pattern features, as argued in the *results* section. To describe our new system accurately, we introduce the distortion term, which effectively increases the free energy of the defect-free state due to the deformation of molecules close to the top cap of the guiding pattern features. The term e_D is no function of the guiding pattern pitch, because the said distortion is independent of the (in-)commensurability of the guiding patterns. Based on this, we state that the parameter e_D as the reason for the observed narrowing of the process window and estimate

$$e_D \approx 0.003\, e_0 \qquad (2B.7).$$

We provide a detailed derivation of the model including the distortion parameter e_D in the supplemental information part. Using the *equation* proposed by Ohta and Kawasaki [36], we can now estimate that the energy penalty due to the domain distortion in the close vicinity of the guiding pattern features accounts for about nine thousandths of kT per chain. This free energy component does not exist in the self-assembly of block copolymers in wide guiding patterns. Our interpretation of this term is, that e_D represents the reason for the smaller process window for the successful alignment of block copolymers in thin topographical guiding patterns than in wide topographical guiding patterns. The smaller process window is particularly obvious when we compare the 110 nm pitch thin feature guiding pattern with the 110 nm trench width pattern for wide guiding pattern features [31]. While the wide guiding pattern shows defect-free assembly, the 110 nm pitch pattern is clearly inside the defective area for the high-resolution guiding patterns.

This finding, furthermore, demonstrates that the maximum free energy difference between the ordered (i.e. defect-free) and the disordered (i.e. defect-loaded) state in the described system merely accounts for *0.004* e_0, which is a result that is in good agreement with calculations done by Garner et al. for chemical guiding patterns [37]. The maximum free energy difference is here defined as the free energy difference for completely commensurate topographical thin guiding patterns.

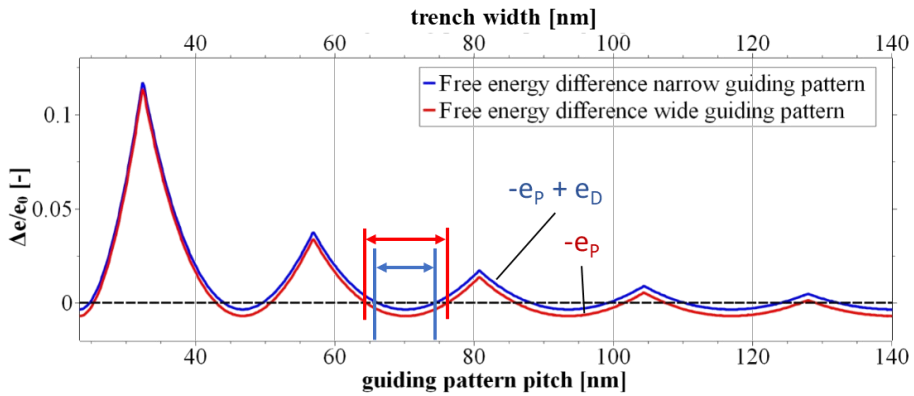

Figure 2B. 6: Comparison of process windows. A direct comparison for wide (red curve) and narrow (blue curve) guiding patterns in graphoepitaxy reveals a smaller process window for narrow guiding patterns.

Figure 2B.6 represents a comparison between the free energy difference as a function of the guiding pattern pitch (for narrow guiding patterns) and the trench width (for wide guiding patterns), respectively. The two curves have been derived in the *chapters 2A and 2B* of this thesis and are now plotted in the same coordinate system to facilitate direct

comparison. The free energy difference for narrow guiding patterns has a larger ordinate for each abscissa value when compared to the wide guiding patterns. This is because the defect-free state in the narrow guiding patterns has a larger free energy when compared to the defective state caused by the distortion in the top cap of the guiding pattern feature that we describe with the distortion parameter e_D. A direct consequence of this behavior is that a larger proportion of the blue curve is above the baseline as compared to the red curve. The areas above the baseline predict the non-favorable defective state. For this reason, we can state that the distortion term is the reason for the reduced process window of the narrow guiding patterns as compared to the wide guiding patterns.

2B.4.2 Derivation of the distortion parameter e_D

This section of the *chapter* is an insertion with the aim to provide additional insight into the determination of the distortion parameter e_D.

The free energy formula *2B.3* can also be written as

$$\frac{e_T}{e_0} = \frac{e_0 + e_{S,\lambda} + e_{AB,\lambda} + e_{AW}}{e_0} \qquad (2B.9),$$

where e_0 is the bulk free energy, $e_{s,\lambda}$ is the free energy penalty induced due to the chain deformation from the minimum free energy chain length.$L_0/2$ Furthermore, $e_{AB,\lambda}$ is the free energy contribution due to the change in A/B-interfaces upon domain deformation. The term e_{AW} is the free energy contribution due to the polymer-wall interaction.

Accordingly, formula *2B.4* can also be written as

$$\frac{e_{Tt}}{e_0} = \frac{e_0 + e_{S,\lambda} + e_{AB,\lambda} + e_{AW}}{e_0} + \frac{e_D}{e_0} \qquad (2B.11).$$

On the other hand, we know that

$$\frac{e}{e_0} = 1 + \frac{e_{AW}}{e_0} + \frac{e_P}{e_0} \qquad (2B.12).$$

Using equations *(2B.9)* and *(2B.12)*, we can state

$$\frac{\Delta e}{e_0} = \frac{e_T}{e_0} - \frac{e}{e_0} = \frac{e_{S,\lambda} + e_{AB,\lambda}}{e_0} - \frac{e_P}{e_0} \qquad (2B.13).$$

In a previous work (see ref. [31] and *chapter 2A*), we have determined

$$\frac{e_P}{e_0} = 0.007 \qquad (2B.14).$$

On the other hand, using the equations *(2B.11)* and *(2B.13)*, we can state accordingly:

$$\frac{\Delta e_t}{e_0} = \frac{e_{Tt}}{e_0} - \frac{e}{e_0} = \left(\frac{e_{S,\lambda} + e_{AB,\lambda}}{e_0} + \frac{e_D}{e_0}\right) - \frac{e_P}{e_0} = \frac{e_{S,\lambda} + e_{AB,\lambda}}{e_0} - \left(\frac{e_P}{e_0} - \frac{e_D}{e_0}\right) \qquad (2B.15).$$

Now, fitting our experimental results (i.e. defects in 80 nm and 110 nm pattern, and defect-free alignment in 90 nm and 120 nm pattern) to determine the offset $(\frac{e_P}{e_0} - \frac{e_D}{e_0})$ yields

$$\left(\frac{e_P}{e_0} - \frac{e_D}{e_0}\right) = 0.004 \qquad \text{(2B.16)}.$$

In the case that the chains are not deformed at all (i.e. $e_{s,\lambda} = 0$ and $e_{AB,\lambda} = 0$),

$$\frac{\Delta e_t}{e_0} = (\frac{e_P}{e_0} - \frac{e_D}{e_0}) \qquad \text{(2B.17)},$$

which means that $\left(\frac{e_P}{e_0} - \frac{e_D}{e_0}\right)$ equals the maximum energy difference between the defect-loaded and the defect-free state in the directed self-assembly of block copolymers in topographical guiding patterns in the size range of the block copolymer domain.

Furthermore, by using *eq. 2B.14* and *eq. 2B.16* we have determined *eq. 2B.7,* (i.e. $e_D = 0.003 * e_0$) is true.

2B.4.3 Estimating the correlation length of block copolymer pattern

It is well known that the average size of particles can be analyzed by the mean of X-rays [38]. The equation developed by Scherrer has successfully been applied to GISAXS [13] and afterwards also used to estimate the correlation length ξ of block copolymers [39]. The estimation of the correlation length of patterns of directed cylindrical block copolymers along their alignment direction by GISAXS measurements has recently been demonstrated [40].

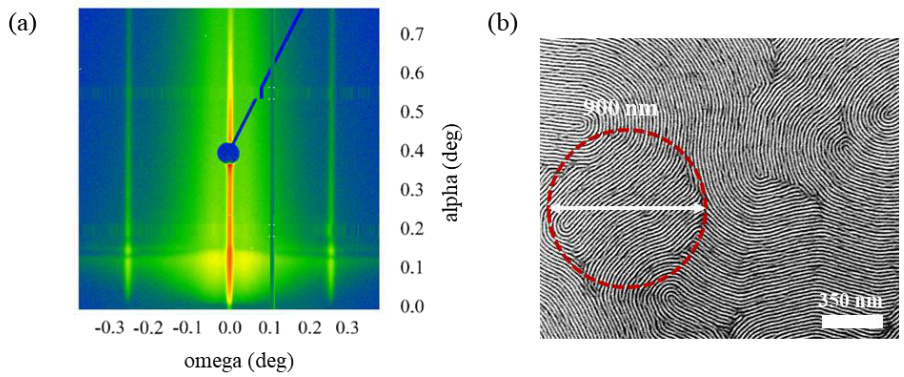

Figure 2B.7: Analysis of a block copolymer fingerprint pattern by the mean of GISAXS and SEM. a): GISAXS pattern of a lamellar diblock copolymer self-assembled in finger print pattern, b): SEM image of the same sample as in a).

The correlation length ξ can be estimated as a function of the width Δq of the respective peak as follows:

$$\xi = \frac{2\pi K}{\Delta q} \qquad \text{(2B.18)},$$

where K is the Scherrer constant, which depends on a variety of factors, like, among others, the shape of the grain and the unit cell [41]. In GISAXS the Scherrer constant for spherical grains accounts for 1.123, and 0.886 for platelets [13]. The peak data is fitted to Gaussian shaped peaks with the mathematical function

$$f(y_0, w, x_c, A) = y_0 + \sqrt{\frac{2}{\pi}} * \frac{A}{w} * e^{-2*\left({}^{(x-x_c)}/_{w}\right)^2} \qquad \text{(2B.19)}$$

with the fit parameters y_0, w, x_c and A. Here, x_c represents the peak center, y_0 is the baseline offset and A is the area under the peak. The parameter w is twice the standard deviation of a Gaussian distribution and relates to the peak *FWHM* as follows:

$$FWHM * 0.849 = w \qquad \text{(2B.20)}.$$

The *FWHM* is set equal to Δq to determine the correlation length. The determination of the correlation length based on the GISAXS pattern depicted in *figure 2B.6 a)* yields $\xi = 903$ *nm*. A comparison of *figure 2B.6 a)* and *b)* confirms that the results yielded by the GISAXS and SEM analysis are comparable. Block copolymer correlation lengths in free surface in the range of few hundreds of nanometers have previously been determined by the analysis of SEM images [42,43].

In the same manner, we have conducted an analysis of the width of the peaks depicted in *figure 2B.6 a)-e)* to extract information about the correlation length ξ of the block copolymers inside the guiding patterns.

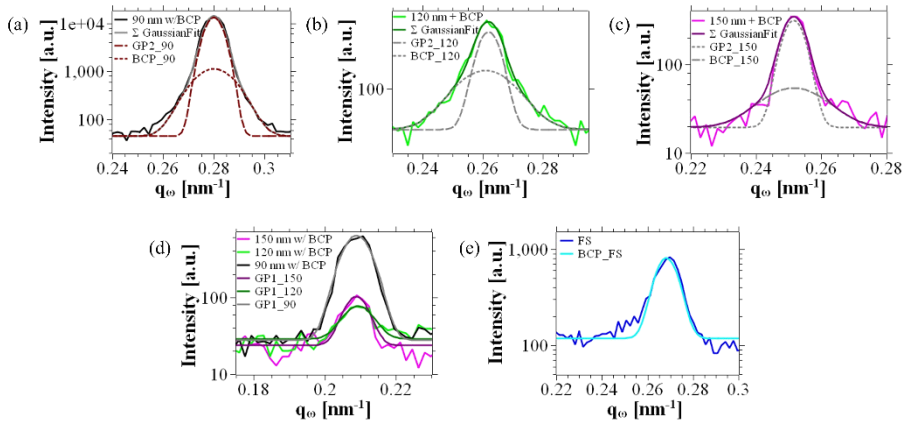

Figure 2B.8: Analysis of all the peaks referred to during the analysis. a): bi-peak fit of 4th GTR of 90 nm pattern with block copolymer, b): bi-peak fit of 5th GTR of 120 nm pattern with block copolymer, c): bi-peak fit of 6th GTR of 150 nm pattern with block copolymer, d):single-peak fit of 3rd GTR of 90 nm pattern, 4th GTR of 120 nm pattern, 5th GTR of 150 nm pattern (all patterns with block copolymer), e): single-peak fit of 1st GTR in free surface.

For the sake of clarity, we plot the fitted peaks separately in *figure 2B.7 a)-e).* Accordingly *figure 2B.7 a)* depicts the measured 4th order peak of the 90 nm guiding pattern in black and the two fitted Gaussians in brown. In the same way, the result of the 5th order peak of the 120 nm guiding pattern is depicted in *figure 2B.7 b)*, the 6th order peak of the 150 nm guiding pattern in *figure 2B.7 c).* To be able to compare the fits properly with GTRs that are not expected to contain signal originating from block copolymer scattering, the next lower order peaks are depicted in *figure 2B.7 d).* Furthermore, the cut through the free surface GTR we have analyzed before is plotted in panel *e)* of the same figure. In addition to that, we give an overview of the results in *table 2B.1* providing the peak name, the associated periodicity and the relevant required to calculate the correlation length.

The relevant values to determine the correlation length according to the formulas previously provided in this chapter are the peak width *w* according to *formula 2B.19,* and the device and experiment dependent peak broadening B_{res} as proposed by ref. [13], which has been determined to be 3.26 μm^{-1}. This result is very close to the uncertainty reported in ref. [40] for a similar experiment. The estimation of the correlation length of the block copolymers is done using *formula 2B.18* and yields 390 nm for the 90 nm pattern, 301 nm for the 120 nm pattern and 302 nm for the 150 nm pattern. The block copolymer pitch inside the 90 nm guiding pattern is compressed to 22.4 nm, while it is stretched to 24.1 nm and 25.0 nm in the 120 nm and 150 nm pitch guiding pattern, respectively.

GISAXS pattern	Peak name	q_α [nm^{-1}]	d [nm]	FWHM [μm^{-1}]	w [μm^{-1}]	w - B_{res} [μm^{-1}]	ξ [nm]
Free surface	BCP_FS	0.263	23.4	7.81	9.56	6.63	903.4
90 nm pitch	GP1_90	0.209	90.2	5.76	7.82	4.89	962.9
	GP2_90	0.280	89.8	4.38	6.65	3.72	1264.5
	BCP_90	0.280	22.4	14.22	15.00	12.07	390.1
120 nm pitch	GP1_120	0.209	120.3	2.29	4.87	1.94	2421.7
	GP2_120	0.261	120.5	5.32	7.45	4.52	1041.4
	BCP_120	0.261	24.1	18.39	18.54	15.61	301.7
150 nm pitch	GP1_150	0.209	150.5	4.22	6.51	3.58	1313.9
	GP2_150	0.252	149.9	4.40	6.66	3.73	1259.8
	BCP_150	0.252	25.0	18.34	18.50	15.57	302.4

Table 2B.1: Overview of peak analysis results.

The discrepancy between the relatively low defect density observed in our SEM images and the low correlation length of the measured patterns may be related to the 3-D self-assembly morphology depicted in *figure 2B.2 i)*. The small distortion of the structures in the guiding patterns may preclude the estimation of quantitatively accurate correlation lengths, because the distortion causes peak widening which is associated to a smaller correlation length. We may still compare the defect density in the different patterns, which represents one of the most important issues in block copolymer lithography [44,45]. Therefore we consider that the correlation length ξ is proportional to the defect density ρ_D^{-2} of the block copolymer pattern [46]. A mathematical expression to estimate the defect density ρ_D in a pattern with pitch p is $\rho_D \propto \frac{p}{\xi^2}$. This analysis shows us that in our experiments the defect density increases with the guiding pattern pitch, i.e. the multiplication factor *(see figure 2B.8)*. We may, however, not forget that the block copolymer self-assembly depends heavily on the guiding pattern commensurability. Consequently, we present this measurement merely as a method to extract qualitative information about the defect density in the directed self-assembly of block copolymers from GISAXS patterns.

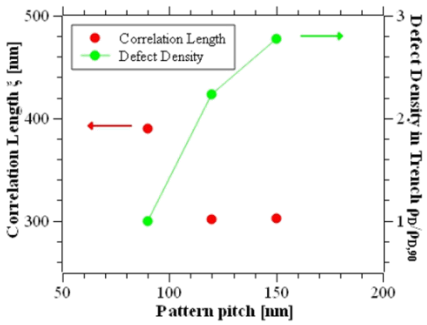

Figure 2B.9: Estimating the correlation length of block copolymers in guiding patterns. Analyzing the correlation length based on FWHM analysis of block copolymer peaks (red dots) and the normalized defect density of block copolymers (green dots) as a function of the guiding pattern pitch.

2B.5 Conclusions

We have presented the fabrication of topographical guiding patterns for the directed self-assembly of block copolymers with sub-10 nm resolution by electron beam exposure of *HSQ*. During the self-assembly in these guiding patterns, we observe a self-assembly morphology, where the block copolymer self-assembles not only between the guiding pattern features, but also on top of them. We deduce that the prerequisite for the block copolymer to self-assemble in this morphology is that the guiding pattern features are in the size range of the *PMMA* domain of the block copolymer.

The present structures have been analyzed by AFM, SEM and GISAXS. Detailed peak-analysis of GISAXS measurements reinforce the thesis about the morphology intuited based on the results of real-space imaging techniques. Furthermore, GISAXS enables the determination of the changing block copolymer pitch as a function of the guiding pattern pitch with sub-nm resolution. Based on an analysis of the peak width, we compare the correlation length of the material in guiding patterns and after self-assembly in fingerprint pattern. We furthermore propose a method to qualitatively analyze the defect density of block copolymers in narrow topographical guiding patterns by GISAXS. A quantitative estimation of the correlation length inside the guiding pattern is difficult due to the uncertainty about the extent of peak broadening that is caused by the distortion of the block copolymer domains adjacent to the guiding pattern features.

At last, we demonstrate that free energy models describing the self-assembly in wide guiding patterns are still valid for the description of our system after minor adjustments are introduced. Based on the modified model and the experimental results of this work, we determine that the maximum difference between the defect-free state and the defect-loaded state for thin guiding pattern features is only about half as large as for the directed

self-assembly in wide guiding patterns. We report that this is due to the distortion created by the incorporation of the thin guiding pattern features in the block copolymer thin film. As a result, the process window for the guiding pattern fabrication is smaller than for regular wide topographical guiding patterns.

2B.6 References

[1] Lane A P, Yang X, Maher M J, Blachut G, Asano Y, Someya Y, Mallavarapu A, Sirard S M, Ellison C J and Willson C G 2017 Directed Self-Assembly and Pattern Transfer of Five Nanometer Block Copolymer Lamellae *ACS Nano* **11** 7656–65

[2] Segalman B R A, Yokoyama H and Kramer E J 2001 Graphoepitaxy of Spherical Domain Block Copolymer Films *Adv. Mater.* **13** 1152–5

[3] Nickmans K, Murphy J N, Waal B De, Leclère P, Doise J, Gronheid R, Broer D J and Schenning A P H J 2016 Sub-5 nm Patterning by Directed Self-Assembly of Oligo (Dimethylsiloxane) Liquid Crystal Thin Films *Adv. Mater.* **28** 10068–72

[4] Müller-Buschbaum P, Gutmann J S, Cubitt R and Petry W 2004 Grazing incidence small-angle neutron scattering - An advanced scattering technique for the investigation of nanostructured polymer films *Phys. B Condens. Matter* **350** 207–10

[5] Pflügler M, Soltwisch V, Probst J, Scholze F and Krumrey M 2017 Grazing Incidence Small Angle X-Ray Scattering (GISAXS) on Small Targets Using Large Beams *IUCrJ* **4** 1–8

[6] Wernecke J, Scholze F and Krumrey M 2012 Direct structural characterisation of line gratings with grazing incidence small-angle x- ray scattering *Rev. Sci. Instrum.* **83** 1039061–8

[7] Suh H S, Chen X, Rincon-Delgadillo P A, Jiang Z, Strzalka J, Wang J, Chen W, Gronheid R, De Pablo J J, Ferrier N, Doxastakis M and Nealey P F 2016 Characterization of the shape and line-edge roughness of polymer gratings with grazing incidence small-angle X-ray scattering and atomic force microscopy *J. Appl. Crystallogr.* **49** 823–34

[8] Grigorescu A E and Hagen C W 2009 Resists for sub-20-nm electron beam lithography with a focus on HSQ: State of the art *Nanotechnology* **292001** 1–31

[9] Min Z, Baoqin C, Changqing X, Ming L and Jiebing N 2010 Study of Process of HSQ in Electron Beam Lithography *Proc. 2010 5th IEEE Conf. Nano/Micor Eng. Mol. Syst.* **5592584** 1021–4

[10] Caster A G, Kowarik S, Schwartzberg A M, Nicolet O, Lim S and Leone S R

2009 Observing hydrogen silsesquioxane cross-linking with broadband CARS *J. Raman Spectrosc.* **40** 770–4

[11] Henschel W, Georgiev Y M and Kurz H 2003 Study of a high contrast process for hydrogen silsesquioxane as a negative tone electron beam resist *J. Vac. Sci. Technol. B* **21** 2018–25

[12] Buffet A, Rothkirch A, Döhrmann R, Körstgens V, Abul Kashem M M, Perlich J, Herzog G, Schwartzkopf M, Gehrke R, Müller-Buschbaum P and Roth S V. 2012 P03, the microfocus and nanofocus X-ray scattering (MiNaXS) beamline of the PETRA III storage ring: The microfocus endstation *J. Synchrotron Radiat.* **19** 647–53

[13] Smilgies D M 2009 Scherrer grain-size analysis adapted to grazing-incidence scattering with area detectors *J. Appl. Crystallogr.* **42** 1030–4

[14] Blachut G, Sirard S M, Maher M J, Asano Y, Someya Y, Lane A P, Durand W J, Bates C M, Dinhobl A M, Gronheid R, Hymes D, Ellison C J and Willson C G 2016 A Hybrid Chemo-/Grapho-Epitaxial Alignment Strategy for Defect Reduction in Sub-10 nm Directed Self-Assembly of Silicon-Containing Block Copolymers *Chem. Mater.* **28** 8951–61

[15] Segal-Peretz T, Ren J, Xiong S, Khaira G, Bowen A, Ocola L E, Divan R, Doxastakis M, Ferrier N J, De Pablo J and Nealey P F 2017 Quantitative Three-Dimensional Characterization of Block Copolymer Directed Self-Assembly on Combined Chemical and Topographical Prepatterned Templates *ACS Nano* **11** 1307–19

[16] Hannon A F, Sunday D F, Bowen A, Khaira G, Ren J, Nealey P F, De Pablo J J and Kline R J 2018 Optimizing self-consistent field theory block copolymer models with X-ray metrology *Mol. Syst. Des. Eng.* **3** 376–89

[17] Borah D, Rassapa S, Shaw M T, Hobbs R G, Petkov N, Schmidt M, Holmes J D and Morris M 2013 Directed self-assembly of PS-b-PMMA block copolymer using HSQ lines for translational alignment *J. Mater. Chem. C* **1** 1192–6

[18] Keen I, Cheng H, Yu A, Jack K S, Younkin T R, Leeson M J, Whittaker A K and Blakey I 2014 Behavior of Lamellar Forming Block Copolymers under Nanoconfinement: Implications for Topography Directed Self- Assembly of Sub-10 nm Structures *Macromolecules* **47** 276–83

[19] Ma S, Con C, Yavuz M and Cui B 2011 Polystyrene negative resist for high-resolution electron beam lithography *Nanoscale Res. Lett.* **6** 1–6

[20] Chen W and Ahmed H 1993 Fabrication of 5-7 nm wide etched lines in silicon using 100 keV electron-beam lithography and polymethylmethacrylate resist *Appl. Phys. Lett.* **62** 1499–501

[21] Vaselabadi S A, Shakarisaz D, Ruchhoeft P, Strzalka J and Stein G E 2016 Radiation damage in polymer films from grazing-incidence X-ray scattering

measurements *J. Polym. Sci. Part B Polym. Phys.* **54** 1074–86

[22] Tolan M, Press W, Brinko F and Kotthaus J P 1995 X-ray diffraction from laterally structured surfaces: Total external re6ection *Phys. Rev. B* **51** 2239–51

[23] Jergel M, Baumbach T, Majkov E and Pinˇ E 2001 Coplanar and non-coplanar x-ray reflectivity characterization of lateral W / Si multilayer gratings *J. Appl. Phys. D Appl. Phys.* **34** A188-92

[24] Rueda D R, Martín-Fabiani I, Soccio M, Alayo N, Pérez-Murano F, Rebollar E, García-Gutiérrez M C, Castillejo M and Ezquerra T A 2012 Grazing-incidence small-angle X-ray scattering of soft and hard nanofabricated gratings *J. Appl. Crystallogr.* **45** 1038–45

[25] Kato A, Burger S and Scholze F 2012 Analytical modeling and three-dimensional finite element simulation of line edge roughness in scatterometry *Appl. Opt.* **51** 6457–64

[26] Yoneda Y 1963 Anomalous surface reflection of X rays *Phys. Rev.* **131** 2010–3

[27] Wernecke J, Krumrey M, Hoell A, Kline R J, Liu H K and Wu W L 2014 Traceable GISAXS measurements for pitch determination of a 25 nm self-assembled polymer grating *J. Appl. Crystallogr.* **47** 1912–20

[28] Cheng J Y, Sanders D P, Truong H D, Harrer S, Friz A, Holmes S, Colburn M and Hinsberg W D 2010 Simple and versatile methods to integrate directed self-assembly with optical lithography using a polarity-switched photoresist *ACS Nano* **4** 4815–23

[29] Cheng J Y, Sanders D P, Truong H D, Harrer S, Friz A, Holmes S, Colburn M and Hinsberg W D 2010 Simple and Versatile Methods To Integrate Directed Self-Assembly with Optical Lithography Using a Polarity- Switched Photoresist *ACS Nano* **4** 4815–23

[30] Choi J, Gunkel I, Li Y, Sun Z, Liu F, Kim H, Carter K R and Russell T P 2017 Macroscopically ordered hexagonal arrays by directed self-assembly of block copolymers with minimal topographic patterns *Nanoscale* **9** 14888–96

[31] Gottlieb S, Kazazis D, Mochi I, Evangelio L, Fernández-Regúlez M, Ekinci Y and Perez-Murano F 2018 Nano-confinement of block copolymers in high accuracy topographical guiding patterns: modelling the emergence of defectivity due to incommensurability *Soft Matter* **14** 6799–808

[32] Turner M S 1992 Equilibrium Properties of a Diblock Copolymer Lamellar Phase Confined between Flat Plates *Phys. Rev. Lett.* **69** 1788–91

[33] Walton D, Kellogg G J, Mayes A, Lambooy P and Russell T P 1994 A Free Energy Model for Confined Diblock Copolymers *Macromolecules* **27** 6225–8

[34] Tsai H, Miyazoe H, Cheng J, Brink M, Dawes S, Klaus D, Bucchignano J, Sanders D, Joseph E, Colburn M and Guillorn M 2015 Self-aligned line-space pattern customization with directed self-assembly graphoepitaxy at 24nm pitch

Proc. SPIE **942314** 14-1–7

[35] Park B S, Stoykovich M P, Ruiz R, Zhang Y, Black C T and Nealey P F 2007 Directed Assembly of Lamellae-Forming Block Copolymers by Using Chemically and Topographically Patterned Substrates *Adv. Mater.* **19** 607–11

[36] Ohta T and Kawasaki K 1986 Equilibirum Morphology of Block Copolymer Melts *Macromolecules* **19** 2621–32

[37] Garner G P, Rincon Delgadillo P, Gronheid R, Nealey P F and De Pablo J J 2017 Design of surface patterns with optimized thermodynamic driving forces for the directed self-assembly of block copolymers in lithographic applications *Mol. Syst. Des. Eng.* **2** 567–80

[38] Scherrer P 1918 Bestimmung der Grösse und der inneren Struktur von Kolloidteilchen mittels Röntgenstrahlen *Nachrichten von der Gesellschaft der Wissenschaften zu Göttingen* 98–100

[39] Majewski P W and Yager K G 2016 Rapid ordering of block copolymer thin films *J. Phys. Condens. Matter* **28** 1–37

[40] Majewski P W and Yager K G 2015 Latent Alignment in Pathway-Dependent Ordering of Block Copolymer Thin Films *Nano Lett.* **15** 5221–8

[41] Langford J I and Wilson A J C 1978 Scherrer after sixty years: A survey and some new results in the determination of crystallite size *J. Appl. Crystallogr.* **11** 102–13

[42] Harrison C, Adamson D H, Cheng Z, Sebastian J M, Sethuraman S, Huse D a, Register R a. and Chaikin P M 2000 Mechanisms of ordering in striped patterns *Science·* **290** 1558–60

[43] Ferrarese Lupi F, Giammaria T J, Volpe F G, Lotto F, Seguini G, Pivac B, Laus M and Perego M 2014 High aspect ratio PS-b-PMMA block copolymer masks for lithographic applications *ACS Appl. Mater. Interfaces* **6** 21389–96

[44] Neisser M and Wurm S 2015 ITRS lithography roadmap: 2015 challenges *Adv. Opt. Technol.* **4** 235–240

[45] Pathangi H, Chan B T, Bayana H, Vandenbroeck N, Van Den Heuvel D, Van Look L, Rincon-Delgadillo P, Cao Y, Kim J, Lin G, Parnell D, Nafus K, Harukawa R, Chikashi I, Nagaswami V, D'Urzo L, Gronheid R and Nealey P 2015 Defect mitigation and root cause studies in IMEC's 14nm half-pitch chemo-epitaxy DSA flow *J. Micro/Nanolithography, MEMS, MOEMS* **14** 0312041-12

[46] Ruiz R, Bosworth J K and Black C T 2008 Effect of structural anisotropy on the coarsening kinetics of diblock copolymer striped patterns *Phys. Rev. B - Condens. Matter Mater. Phys.* **77** 1–5

Chapter 3:

Thermal scanning probe lithography for the directed self-assembly of block copolymers

Abstract:

Thermal scanning probe lithography (t-SPL) is applied to the fabrication of chemical guiding patterns for directed self-assembly of block copolymers. The two key steps of the overall process are the accurate patterning of a *poly(phthalaldehyde*) (*PPA*) resist layer of only 3.5 nm thickness, and the subsequent oxygen-plasma functionalization of an underlying neutral *poly(styrene-random-methyl methacrylate)* (*PS-r-PMMA*) brush layer. We demonstrate that this method allows one to obtain aligned line/space patterns of *poly(styrene-block-methyl methacrylate)* block copolymers of 18.5 nm and 11.7 nm half-pitch. Defect-free alignment has been demonstrated on an area of tens of square micrometers. The main advantages of t-SPL are the absence of proximity effects, which enables the realization of patterns with 10 nm resolution, and its compatibility with standard DSA methods. In the brush activation step by oxygen-plasma exposure, we observe swelling of the brush. This effect is discussed in terms of the chemical reactions occurring in the exposed areas. Our results show that t-SPL can be a suitable method to direct the self-assembly for research activities in the field of DSA, in particular for low-pitch, high-χ block copolymers to achieve sub-10-nm line/space patterns.

Table of contents: Chapter 3

3.1 Introduction

In this chapter, we report on the use of the proximity-effect-free, low-cost thermal scanning probe lithography (t-SPL) for the creation of dense guiding patterns. It has been shown that t-SPL [1] can be used to fabricate sub-20-nm-sized patterns [2]. The patterning principle in t-SPL relies on the resistive heating of an AFM tip up to temperatures of 700 - 1000 °C. When the heated tip is brought into contact with a *poly(phthalaldehyde*) resist layer [3], the polymer evaporates in nanometre-sized areas. *PPA* is a self-amplified depolymerizing material with a decomposition temperature of about 150 ºC [4]. By heating the tip to a temperature considerably above the polymer decomposition temperature, polymer evaporation is promoted with very short tip-resist interaction times (see *figure 3.1 a)*). The main patterning parameters are the tip temperature, the tip-surface contact duration and contact force [5]. Thanks to the microsecond-scale polymer evaporation, the patterning at tip velocities of up to 20 $^{mm}/_{s}$ has been demonstrated [4], which means a throughput of up to 10^4 - 10^5 μm^2 per hour [6]. Another interesting application of t-SPL is the fabrication of 3D patterns in *PPA* [5], where the tip contact pressure is used to modulate the writing depth.

In the experiments presented in this chapter, we combine t-SPL with surface chemical modification to direct the self-assembly of block copolymers (e.g. chemoepitaxy). Chemoepitaxy has been demonstrated [7,8] to be an efficient way for directing the self-assembly of block copolymers as well as to be suitable for large-scale integration. To avoid the formation of dislocations and defects, it is crucial to induce chemically attractive areas with the natural pitch of the material [9] or a small integer multiple thereof [10] with high resolution and high accuracy.

One way to obtain chemical contrast is to expose a surface-sensitive polymeric brush layer to an oxygen plasma through a resist mask defined by means of lithographic methods, such as e-beam lithography [10] or DUV [11]. The interaction of the brush layer and the oxygen plasma promotes structural changes in the brush layer in such a way that the plasma-modified areas are preferentially wetted by one of the blocks. Maskless e-beam exposure [12] and local anodic oxidation (LAO) [13] are techniques that are also capable of inducing a chemical contrast in the neutral brush layer. There, the chemical contrast is directly induced by the interaction of charged particles with the brush layer. The major drawback of DUV-based fabrication of chemical guiding patterns is the high cost of equipment required at the production site. Moreover, proximity effects make it very difficult to obtain high-density *and* high-resolution guiding patterns by e-beam lithography. In contrast to light-based methods, probe-based lithography methods do not suffer from constraints due to diffraction effects.

In this chapter we present our results concerning the application of t-SPL to create guiding

patterns through selective exposure to an oxygen plasma. The performance of the method is evaluated in terms of pattern resolution and material (e.g. *PPA*) compatibility.

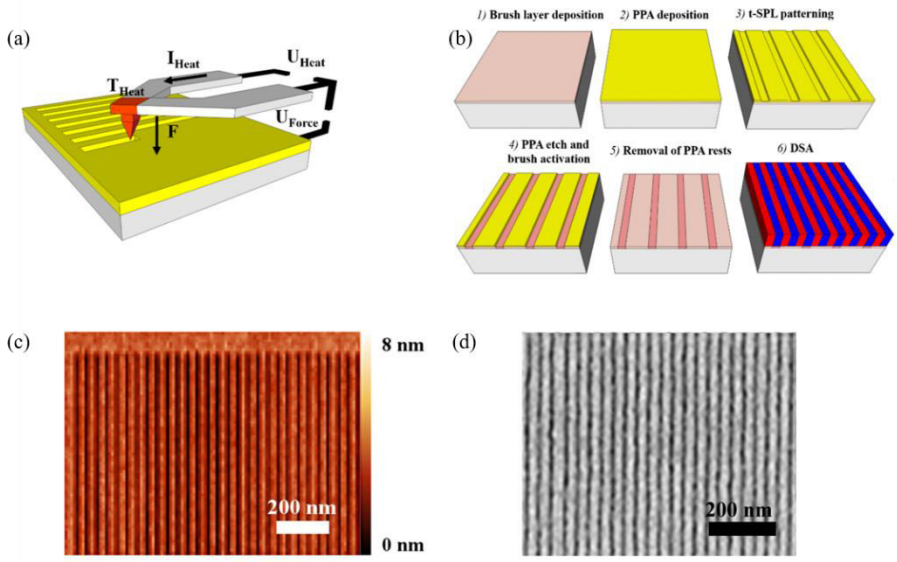

Figure 3.1: Work-flow and overview of results. a): Scheme of t-SPL working principle. To write a pixel, the resistively heated AFM tip is pulled into contact with the PPA surface by an electromechanically induced force F for several microseconds, b): the workflow can be divided into six steps, from brush deposition to the final directed self-assembly, c): AFM contact-mode height image of a t-SPL guiding pattern in PPA corresponding to step 3) in the workflow scheme, d): example of directed self-assembly of block copolymers on guiding patterns fabricated according to the workflow presented in b). Images b) and c) of this figure have been taken by Matteo Lorenzoni.

3.2 Experimental Section

The overall workflow to achieve long-range-ordered line structures by chemical modification induced by oxygen plasma is subdivided into six steps as shown in *figure 3.1 b)*. The initial substrate is a p-doped *silicon* wafer (4 – 40 Ω·cm resistivity) with a native *oxide* layer. After cleaning the substrate in *isopropyl alcohol* and *acetone*, a polymer brush layer and a *PPA* layer are deposited. Then the *PPA* is patterned by t-SPL, and the resulting pattern is transferred to the brush layer by an oxygen plasma. A local chemical modification is introduced in those areas that have been patterned by t-SPL. In the non-patterned area, the remaining *PPA* layer is removed, and the block copolymer film is deposited. *Figure 3.1 c)* shows a pattern defined by t-SPL on an 8-nm-thick *PPA* film, and *figure 3.1 d)* depicts the result of a self-assembled block copolymer pattern at the end of the annealing process. It shows the directed self-assembly of a 37 nm pitch *PS-*

b-PMMA block copolymer induced by the guiding pattern of *figure 3.1 c)*. To increase the topographic contrast, the image was taken after partial removal of the *PMMA*-domains by O_2 plasma etching. The process steps are referred to one-by-one on the following pages.

3.2.1 Brush layer deposition

Two kinds of polymer brush layers are used, depending on the block copolymer whose self-assembly was to be directed: a 7 nm thick brush layer of *PS-r-PMMA* with a *styrene* fraction of 58 % (M_{R60} = 7.9 $^{kg}/_{mol}$, PDI 1.85) and an 8 nm-thick *hydroxyl-terminated polystyrene* (*PS-OH*) brush layer ($M_{PS\text{-}OH}$ = 4.5 $^{kg}/_{mol}$, PDI 1.09) are grafted to the silicon substrate. To obtain these layers, 1.3 wt% of polymer are dissolved in *propylene glycol methyl ether acetate* (PGMEA) in case of *PS-r-PMMA* and in *toluene* in case of *PS-OH*, spin-coated at 5000 rpm for 30 s and subsequently annealed at 230 °C for 5 min. Then the sample is rinsed in a *PGMEA* ultrasonic bath for 5 min, and afterwards dipped in *acetone* and *isopropyl alcohol*. This treatment assures the removal of any non-grafted material from the sample. The roughness of the grafted layers accounts for 0.2 – 0.3 nm. The *PS-r-PMMA* brush layer is synthesized by Arkema and the *PS-OH* brush layer has been purchased from Polymer Source.

3.2.2 PPA deposition

The 3.5 nm thick t-SPL resist layer is deposited by spin-coating of 0.25 wt% *PPA* dissolved in *methoxybenzene* at 2000 rpm for 90 s. A 35 s spin-coating of a 1 wt% *PPA* solution at 3000 rpm leads to a film thickness of 10 nm. A discussion of the non-uniformities of the *PPA* layer on top of *PS-r-PMMA* can be found in the discussion part.

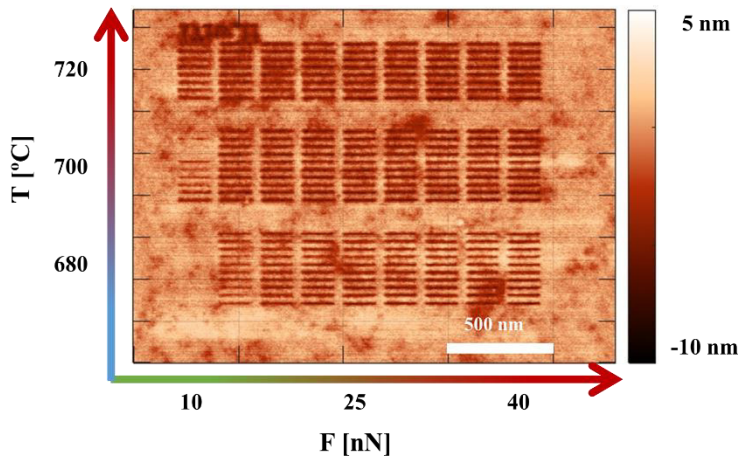

Figure 3.2: Patterning test with t-SPL to determine the process conditions. An array of ten vertical short lines is patterned into the PPA layer in order to determine the optimum writing conditions individually for each tip.

3.2.3 t-SPL patterning

To take advantage of the high-resolution patterning capability of t-SPL, super sharp *silicon*-tips with a nominal apex radius of 3 nm were used. The line patterns were written along the fast scan direction at a tip-heater temperature between 680 °C and 720 ºC, and applying between 10 nN and 40 nN force pulses of 5 µs duration. A patterning test covering this parameter field is depicted in *figure 3.2.* After patterning of a line, that line was immediately imaged in contact mode. The combination of fabrication and imaging is the principle of closed-loop lithography (CLL) [1]. This mode is very useful to correct the lithography conditions during the writing process. To obtain good imaging resolution, each written line corresponds to eight reading lines. Imaging the lines directly after their fabrication is possible because the time required for the tip to cool down after one heating phase corresponds to the thermal time constant of the heater of 6 µs. An example of a t-SPL pattern is given in *figure 3.1 c)*.

3.2.4 PPA trim and brush activation

An oxygen-plasma exposure step is used to etch the remaining *PPA* layer at the bottom of the patterned lines and to activate the unveiled brush layer. We used an oxygen plasma at 1 mbar and 150 W for 8 s to functionalize the *PS-r-PMMA* brush and an O_2/N_2 1:4 gas mixture, 10 W power and a pressure of $2 \cdot 10^{-2}$ mbar to functionalize the *PS-OH* brush.

3.2.5 Removal of PPA rests

After functionalization, any remaining *PPA* is removed by dipping the sample into a *cyclohexanone* bath for 2 s. The cyclohexanone is purchased from Sigma Aldrich and used as received.

3.2.6 Directed self-assembly

Two different block copolymer materials are used in this work. A slightly asymmetric *PS-b-PMMA* copolymer (M_{PS}= 18.1 $^{kg}/_{mol}$ and M_{PMMA}= 24.2 $^{kg}/_{mol}$, PDI 1.1) was deposited by spin coating at 2500 rpm for 30 s from a 1.1 wt% solution in *PGMEA*. The polymer self-assembled in structures with $L_0 = 23.4$ *nm* pitch. Self-assembly is induced by an annealing step at 230 °C for 10 min on a hot plate in ambient atmosphere. The resulting film thickness is 22 nm. For the second material, a 30 nm thick block copolymer film is deposited from a 1.5 wt% solution of a *PS-b-PMMA* polymer (M_{PS}= 39.5 $^{kg}/_{mol}$, M_{PMMA}= 39.5 $^{kg}/_{mol}$, PDI 1.09), resulting in a pitch size of L_0 = 37 nm. Both materials are spin-coated and annealed under the same conditions. An aligned block copolymer pattern of L_0 = 37 nm pitch size is shown in *figure 3.1 d).* Both block copolymer materials are provided by Arkema.

3.2.7 Characterization

The samples undergo an analysis after every step. The micrographs presented in this

chapter are taken in AFM tapping mode (*Dimension Icon / Nanoscope V, Bruker*) and with a scanning electron microscope (SEM) (*AURIGA; Zeiss*), where we use the In-lens detector. The images of the t-SPL patterns are taken with the t-SPL tool in contact mode. WSxM [14] is used to process some of the images.

3.3 Results

The minimum achievable structure size in t-SPL depends on the shape and geometry of the tip. Because the tip is conically shaped, it is recommended to work with extremely thin *PPA* layers to push the resolution of the technique. Writing deep patterns into thick *PPA* layers has a resolution-limiting effect because, as sketched in *figure 3.3 a)*, material will also be removed by the conical upper part of the probe, if the writing depth is larger than the tip radius. This indicates that at large writing depths the ultimate resolution is determined by the opening angle of the conically shaped part of the probe far away from the apex, and thus not directly by the radius of the tip. In contrast to that, the resolution at small writing depths is determined by the radius of the apex.

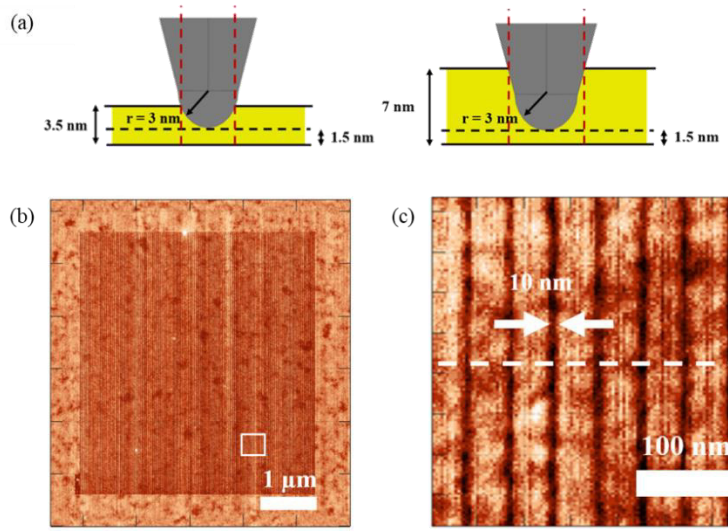

Figure 3.3: t-SPL patterns. a): A scheme of the t-SPL tip geometry. The nominal tip radius is 3 nm. The minimum achievable lateral resolution for two different writing depths, 2 nm and 5.5 nm, is indicated by the dashed red lines, b): Patterns written in PPA. Overall pattern with slight onset of a dewetting effect of PPA on brush. Z-range is 5 nm, c): Highly uniform pattern with 10 nm lines at 46.8 nm pitch in a close-up of the area indicated by the white box in b). Z-range is 5 nm.

Results of t-SPL patterning of a 3.5 nm thick *PPA* layer are shown in *figures 3.3 b) and*

figure 3.3 c). The patterning step was done at a contact force of 40 nN. The pattern lines were written parallel to the fast scan direction. To write a line, the tip temperature is set to 680 ºC for a single scan line. The t-SPL contact-mode image (see *figure 3.3 b*)) shows a patterned area of 25 μm^2 that has been written with an average tip velocity of 16.1 $^{\mu m}/_{s}$. The total time required for patterning and imaging is 5 min. A pattern with a resolution of 10 nm line width is achieved. This remarkable resolution was obtained by writing shallow patterns of only 2 nm depth, taking advantage of the extremely high resolution of t-SPL for patterning. The pattern pitch is 46.8 nm, which is equal to $2L_0$, where L_0 is the pitch of the block copolymer. In consequence, the multiplication factor $\eta = 2$, where η is defined as the ratio of the period of the guiding pattern period to the pitch of the block copolymer. As the patterns are shallower than the *PPA* film thickness, the polymer brush is not unveiled. The absence of piled-up material on the borders of the written lines proves that the *PPA* film has indeed been removed by evaporation and not by mechanical force. This observation leads to the conclusion that a tip temperature of 680 ºC is sufficiently high for the patterning process.

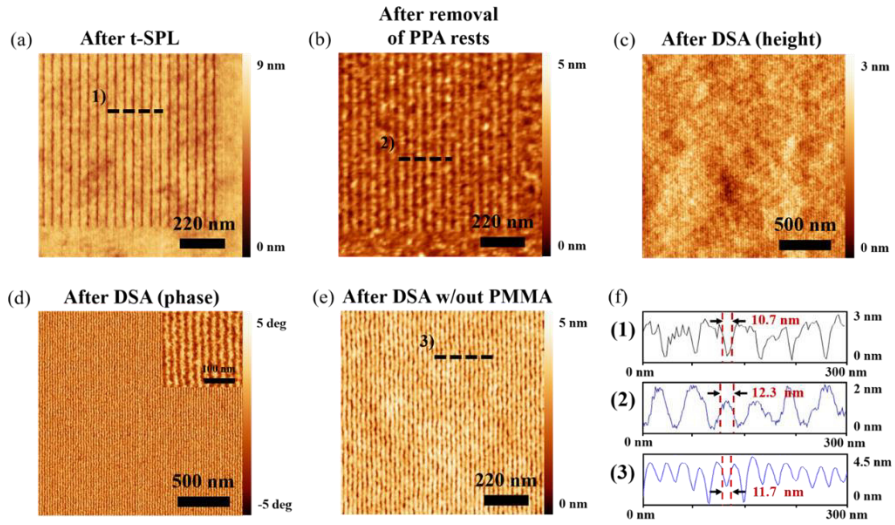

Figure 3.4: Documentation of workflow by the mean of AFM images. a): AFM height image after t-SPL patterning. b): AFM height image after residual PPA removal, showing the chemical guiding stripes on the polymer brush. c): AFM height image of aligned block copolymer on guiding pattern depicted in b). d): AFM phase image of the same area as depicted in c), e): AFM height image after removing the PMMA block by the mean of oxygen plasma. f): Comparative study of profiles (top to bottom) along the dashed black lines indicated in a), b) and e), respectively. The patterned lines in (1) are recessed, whereas after oxygen-plasma exposure, they are elevated (2). A density multiplication takes place from (2) to (3).

Fine-tuning of the plasma exposure process is crucial for achieving an optimal chemical

guiding pattern. Moreover, the process conditions have to be such that the residual *PPA* layer in the patterned lines can be removed without removing the *PPA* layer in the non-patterned areas and without removing the brush layer. This means that during the oxygen-plasma exposure the remaining 1.5 nm *PPA* layer in the patterned area has to be removed accurately, whereas the 3.5 nm thick pristine *PPA* layer in the non-patterned area must not be etched away entirely to make sure that the chemical modification of the brush takes place exclusively in the patterned area. *Figures 3.4 a)* and *b)* compare the patterns before and after oxygen-plasma activation. The area selected for the analysis corresponds to the edge of the patterned area, so that we can compare the change in pattern height with the unpatterned area. After the removal of the residual *PPA*, the pattern shows a homogeneous and regular line/space pattern *(see figure 3.4 b))*. Because of the brush annealing step, the neutral *PS-r-PMMA* brush layer is grafted onto the silicon surface so that the *cyclohexanone* dipping step to remove the remaining *PPA* does not affect the integrity of the brush layer. Interestingly, the previously patterned and oxygen-plasma-exposed areas appear slightly elevated in height with respect to the pristine brush layer. The difference in height is about 1.8 nm.

Figure 3.4 c) shows an AFM height image of the resulting block copolymer pattern immediately after self-assembly. As it is difficult to visualize the block copolymer pattern in AFM height images, we also present an AFM phase image in *figure 3.4 d)*. AFM phase imaging helps us to acquire a higher contrast image of the phase separated block copolymer despite of the flat sample topography. To enhance the surface contrast of the block copolymer AFM image, a brief oxygen plasma treatment of 5 seconds at 100 W is applied. This leads to a topography contrast between the two blocks because the etch rate of *PMMA* is larger than that of *PS* [15,16]. For this reason the recessed lines correspond to *PMMA* blocks. The result of this process step is depicted in *figure 3.4 e).* The AFM images presented in *figures 3.4 a), b) and e)* have the same *x*- and *y*-scale so that they are directly comparable and the concept of the multiplication factor η becomes evident: The self-assembled pattern is clearly denser than the line pattern fabricated with t-SPL. This is illustrated in the profiles extracted from *figures 3.4 a), b)* and *e)* along the dashed lines indicated in *figure 3.4 f).*

The SEM images presented in *figures 3.5 a)* and *b)* contribute to a better understanding of the morphology of the self-assembled structures. *Figure 3.5 a)* shows the same DSA pattern as *figure 3.4 e)*. It exhibits a large-area defect-free directed self-assembly. As explained by Wang et al. [17], a notable part of the structure in *PS-b-PMMA* structures with such small domain sizes still consists of a diffuse interface, where the structure is neither pure *PS* nor pure *PMMA*. This could explain the relatively large line-edge roughness of the structures, which is even larger after removal of the *PMMA* block [18].

The absence of defects proves that commensurable guiding patterns can be fabricated with t-SPL. As shown by coarse-grained many-body simulations of self-assembly, block copolymers may form a wetting layer above wide guiding stripes [19], depending on the strength of the affinity between the modified brush and the blocks. This would lead to a U-shaped configuration of the block copolymers, in which the structure in top view appears to self-assemble into vertical lamellae, although there is a *PMMA* bottom layer parallel to the guiding stripes. In our patterns we do not observe any difference in height, pointing to the existence of a wetting layer. This indicates that the guiding patterns are commensurate with $^{L0}/_{2}$ and that the affinity strength of the guiding patterns is suitable.

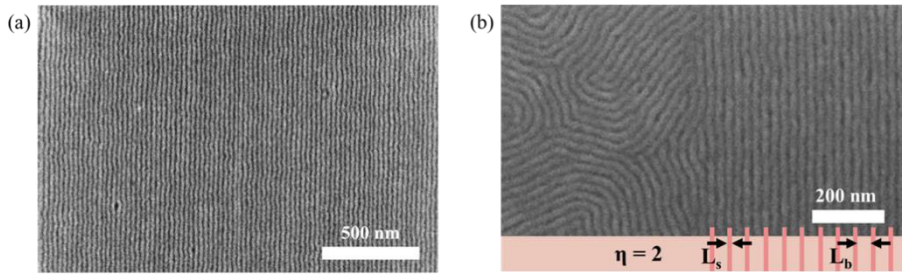

Figure 3.5: SEM images of aligned block copolymer. (a) Defect-free aligned block copolymers on micrometre-scale patterned area with both PS and PMMA blocks present. (b) Comparison of patterned area (right) and non-patterned area (left) shows the influence of the chemical guiding patterns on the self-assembly of the block copolymers. At the bottom on the right of the image, the dimensions of the guiding pattern are indicated. SEM images were taken after removal of the PMMA block by oxygen plasma.

Figure 3.5 b) is an image taken at the edge of the patterned area. On the left-hand side of the image, the characteristic fingerprint pattern can be observed. There is no long-range order in the non-patterned area of the sample. In sharp contrast to that, the block copolymer self-assembles in straight vertical lines on the right-hand side of the image. The patterned and the non-patterned areas can be understood as two adjacent grains. In the patterned area, the block copolymers self-assemble according to the guiding pattern whereas the adjacent grains nucleate and self-assemble randomly. The transition zone from one area to the other is narrow, and a large number of defects are generated at the interface. The interface can also be referred to as grain boundary. A high density of defects in close vicinity of the grain boundary indicates a large grain boundary energy and thus a large guiding pattern strength. The energy penalty of one point defect is in the range of 200 k_BT [20].

3.4 Discussion

3.4.1 Guiding stripe dimensions

Let us now focus on the analysis of the chemical guiding patters. First, we compare the dimensions of the t-SPL pattern with those of the pattern that is subsequently transferred to the brush layer. A single line profile of the pattern shown in *figure 3.4 a)* is depicted in the top panel of *figure 3.4 f).* The reason why the exposed lines are elevated in height is discussed below. The mean width is L_s *=10.7 nm* with a standard deviation σ *= 1.15 nm*. The mean width of the lines transferred to the brush layer (see second profile in *figure 3.4 d)*) is L_s*= 20.7 nm*, with a standard deviation σ *= 2.04 nm*. This profile is part of the profile indicated by the dashed line in *figure 3.4 b)*. Assuming that the nominal tip radius of the imaging probe is 7 nm and the average line height is 1.8 nm, the line width is overestimated by 8.4 nm (tip convolution effect). This implies that the actual line width is $L_{s,corr}$*=12.3 nm*. This means that the plasma activation step causes almost no widening of the structures. The guiding pattern corresponds to *0.52* L_0, which is close to the optimal value. Theoretical considerations reveal that (as a function of the guiding pattern strength) the optimal guiding pattern width for this pattern is slightly below the width of the *PMMA* domain to minimize the energy penalty induced by the curvature of the interface between the two blocks [19].

3.4.2 Pattern functionalization

Now we discuss the effect that leads to the swelling of oxygen-plasma-exposed lines in the brush layer. *Figure 3.4 b)* shows an AFM height image of a pattern at *step 5* that has been exposed to oxygen plasma for 8 s. From this image, we conclude that there is an effect that leads to the swelling of the brush layer after short exposure times, before the material removal process begins. The etch rate of *PPA* was estimated to be 44 $^{nm}/_{min}$. Taking into consideration that the device needs about 2.5 s to ignite a plasma, the actual exposure time is reduced to 5.5 s. If we also take into consideration that it takes approximately 2 s to etch through the 1.5 nm of remaining *PPA* film, the effective exposure time of the film to the plasma is 3.5 s. The swelling effect can be explained by the addition of unspecific functional groups in the exposed areas [21]. One of the characteristics of these functionalized layers is the relatively large ratio of polar *hydroxyl* groups. The number of *oxygen* on the uppermost polymer layer has been reported to increase and exhibit up to 18 – 24 *oxygen* atoms per 100 carbon atoms in the first 2 s of plasma exposure [22]. Polar *oxygen*-containing groups may be the reason for both the functionalization of the brush and the observed swelling. The existence of polar groups on the surface can explain the attractiveness of these areas to *PMMA* [10] because *methyl methacrylate (MMA)* monomers are slightly more polar than *styrene* monomers.

Extending the effective exposure time by 2 s leads to a pattern in which the exposed lines

are on a lower height level than the pristine brush layer, indicating a partial etching of the brush *(figure 3.6 a))*. The single line profile depicted in *figure 3.6 b)* shows the recess of the exposed areas. We conclude that after the initial formation of functionalized groups, a degradation process of the polymeric films starts once the surface is saturated with *oxygen*-containing by-products. Particularly, the aromatic ring of *polystyrene* suffers from degradation because of its large cross section [21]. Previous work suggests that *polystyrene* loses its aromatic rings relatively fast because it is attached to the rest of the monomer only through a single carbon-carbon bond. This mechanism initiates a crosslinking that leads to the formation of carbon-carbon double bonds [22]. The partial etching of the brush could thus be explained by the removal of aromatic rings from *styrene* species, which renders the surface chemically less similar to *PS*, which, in turn favours the wetting of these areas by *PMMA* even more.

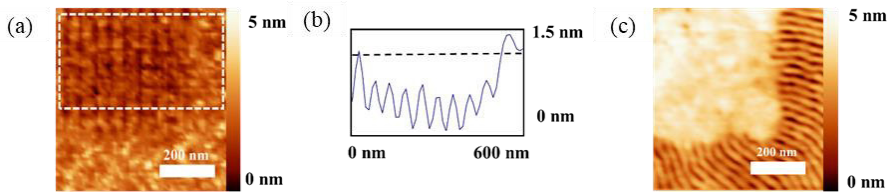

Figure 3.6: The nature of patterned lines after oxygen-plasma activation. a): AFM height image of an overexposed pattern, b): height profile averaged over the box indicated by the dashed white line in a) shows that the lines in the overexposed pattern are recessed with respect to the pristine brush layer, c): behaviour of block copolymers on an over-etched pattern. The morphology changes from vertical to horizontal lamellae.

The resulting behaviour of the deposited block copolymer on this pattern is shown in *figure 3.6 c)*. Increasing the *oxygen*-plasma exposure time consequently leads to a change of the self-assembly morphology from vertical lamellae to horizontal lamellae. The height of the vertically oriented area increases because vertical lamella block copolymers can only self-assemble in film thicknesses d with $d = n\,L_0$ and $n \geq 1$. As the block copolymer film thickness initially deposited is slightly below the material's natural pitch, $L_0 = 23.4\ nm$, the difference in height originates in this effect. Furthermore, it is expected that the increased etching time enlarges the width of the functionalized area.

3.4.3 PPA dewetting

As discussed in the main text, the *oxygen*-plasma activation step is crucial for the performance of the chemical guiding patterns. However, taking a closer look at *figure 3.3 a)* reveals a certain inhomogeneity in the *PPA* layer. Areas appear in which the *PPA* film seems to undergo a process similar to dewetting. As such problems do usually not occur when depositing *PPA* on *silicon* samples, we compared the behaviour of *PPA* on *silicon*

and on the neutral random copolymer brush layer. Corresponding AFM height images are depicted in *figures 3.7 a)* and *b)*, respectively. *Figure 3.7 a)* shows a *PPA* film deposited on a brush layer as used in our experiments. In addition to that, the sample was heated at 60 ºC for 90 s to enhance the mobility of the polymer chains and to accelerate possible dewetting effects. This temperature is well below the glass-transition temperature of *PPA* (137 ºC), *PMMA* (105 ºC) and *PS* (90 ºC). The depth of the holes corresponds to the thickness of the *PPA* deposited. In contrast to that, there is no such dewetting effect of *PPA* when it is directly spun onto *silicon* (see *figure 3.7 b)*.

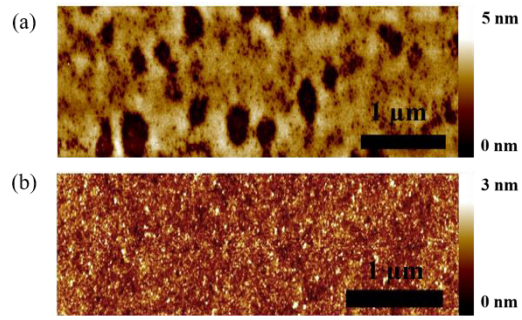

Figure 3.7: Comparison of the PPA thin-film morphologies on two different substrates. (a) PPA deposited onto PS-r-PMMA, (b) PPA deposition directly onto silicon.

Therefore, we conclude that the dewetting originates from the high surface tension between the brush layer and the *PPA*. Although the holes were transferred to the brush and led to a changed self-assembly morphology, an optimization of the etching step could prevent this problem. We did not experience compatibility problems when depositing the *PPA* layer on top of a hydroxyl-terminated *polystyrene* brush layer (*PS-OH*). The drawback of this brush chemistry is, however, that far away from the patterned area the polymer does not self-assemble into a fingerprint pattern. It requires stronger guiding patterns to direct the block copolymers on a *PS-OH* brush than on a *PS-r-PMMA* brush.

3.5 Conclusions

We have demonstrated the directed self-assembly of block copolymers with very small domain sizes in a chemoepitaxy process using t-SPL as lithography method for creating the guiding patterns. We have shown that it is possible to fabricate dense patterns for aligning the self-assembled block copolymers with half-pitches in the range of 10 nm. This result is possible thanks to the inherent absence of proximity effects in t-SPL.

We have demonstrated the fabrication of 10 nm-wide chemical guiding patterns using a merely 3.5 nm thick resist mask. For the chemical functionalization of the brush, we have developed a demanding, but reproducible etching/brush activation process. We have

observed the swelling of the activated *PS-r-PMMA* brush layer when exposed to *oxygen* plasma for few seconds, which is attributed to the attachment of polar functional groups. Longer exposure times lead to the removal and cracking of aromatic rings and a widening of the exposed areas.

We conclude that brush layer functionalization is exclusively due to the *oxygen*-plasma activation. We have also shown that we can tailor the strength of the guiding pattern by varying the *oxygen*-plasma exposure time.

Based on the results presented in this paper, we consider t-SPL to be a viable alternative to e-beam lithography for studies that require both high resolution and dense patterns. The process represents a good option for nanofabrication as an alternative to synchrotron radiation or expensive DUV immersion lithography, and it is compatible with the methods commonly used in directed self-assembly.

3.6 References

[1] Pires D, Hedrick J L, Silva A De, Frommer J, Gotsman B, Wolf H, Despont M, Duerig U and Knoll A W 2010 Nanoscale Three-Dimensional Patterning of Molecular Resists by Scanning Probes *Science·* **328** 732–5

[2] Wolf H, Rawlings C, Mensch P, Hedrick J L, Coady D J, Duerig U and Knoll A W 2015 Sub-20 nm silicon patterning and metal lift-off using thermal scanning probe lithography *J. Vac. Sci. Technol. B* **33** 02B102-1-6

[3] Coulembier O, Knoll A, Pires D, Gotsmann B, Duerig U, Frommer J, Miller R D, Dubois P and Hedrick J L 2010 Probe-based nanolithography: Self-amplified depolymerization media for dry lithography *Macromolecules* **43** 572–4

[4] Paul P C, Knoll A W, Holzner F, Despont M and Duerig U 2011 Rapid turnaround scanning probe nanolithography. *Nanotechnology* **22** 275306-1–9

[5] Knoll A W, Pires D, Coulembier O, Dubois P, Hedrick J L, Frommer J and Duerig U 2010 Probe-based 3-D nanolithography using self-amplified depolymerization polymers *Adv. Mater.* **22** 3361–5

[6] Garcia R, Knoll A W and Riedo E 2014 Advanced scanning probe lithography *Nat. Nanotechnol.* **9** 577–87

[7] Liu C C, Han E, Onses M S, Thode C J, Ji S, Gopalan P and Nealey P F 2011 Fabrication of lithographically defined chemically patterned polymer brushes and mats *Macromolecules* **44** 1876–85

[8] Teik B, Tahara S, Parnell D, Rincon P A, Gronheid R, Marneffe J De, Xu K, Nishimura E and Boullart W 2014 Microelectronic Engineering 28 nm pitch of line / space pattern transfer into silicon substrates with chemo-epitaxy Directed

Self-Assembly (DSA) process flow *Microelectron. Eng.* **123** 180–6

[9] Edwards B E W, Montague M F, Solak H H, Hawker C J and Nealey P F 2004 Precise Control over Molecular Dimensions of Block-Copolymer Domains Using the Interfacial Energy of Chemically Nanopatterned Substrates *Adv. Mater.* **16** 1315–9

[10] Ruiz R, Kang H, Detcheverry F A, Dobisz E, Kercher D S, Albrecht T R, de Pablo J J and Nealey P F 2008 Density Multiplication and Improved Lithography by Directed Block Copolymer Assembly *Science.* **321** 936–9

[11] Tiron R, Chevalier X, Couderc C, Pradelles J, Bustos J, Pain L, Fleury G and Hadziioannou G 2011 Optimization of block copolymer self-assembly through graphoepitaxy : A defectivity study *J. Vac. Sci. Technol. B* **29** 1–8

[12] Evangelio L, Fernández-Regúlez M, Borrisé X, Lorenzoni M, Fraxedas J and Perez-Murano F 2015 Creation of guiding patterns for directed self-assembly of block copolymers by resistless direct e-beam exposure *J. Micro/Nanolith. MEMS MOEMS.* **14** 033511-1–6

[13] Fernández-Regúlez M, Evangelio L, Lorenzoni M, Fraxedas J and Perez-Murano F 2014 Sub-10 nm resistless nanolithography for directed self-Assembly of block copolymers *ACS Appl. Mater. Interfaces* **6** 21596–602

[14] Horcas I, Fernández R, Colchero J and Baro A M 2017 WSXM : A software for scanning probe microscopy and a tool for nanotechnology *Rev. Sci. Instrum.* **78** 013705-1–8

[15] Liu C, Nealey P F, Ting Y and Wendt A E 2007 Pattern transfer using poly(styrene-block-methyl methacrylate) copolymer films and reactive ion etching *J. Vac. Sci. Technol. B* **25** 1963–8

[16] Taylor G N and Wolf T M 1980 Oxygen plasma removal of thin polymer films *Polym. Eng. Sci.* **20** 1087–92

[17] Wan L, Ruiz R, Gao H, Patel K C and Albrecht T R 2015 The Limits of Lamellae-Forming PS-b-PMMA Block Copolymers for Lithography *ASC Nano* **9** 7506–14

[18] Millward D B, Lugani G S, Khurana R, Light S L, Niroomand A, Hustad P D, Trefonas P, Chang S, Lee C N and Quach D 2014 A comparison of the pattern transfer of line-space patterns from graphoepitaxial and chemoepitaxial block co-polymer directed self-assembly *SPIE Proc.* **9054** ·0M-1-14

[19] Garner G, Williamson L, Seidel R, Rincon Delgadillo P, Hur S-M, Gronheid R, Nealey P F and de Pablo J J 2015 The effects of geometry and chemistry of nanopatterned substrates on the directed self-assembly of block-copolymer melts *Proc. SPIE* **9423K** 1–9

[20] Hur S-M, Thapar V, Ramírez-Hernández A, Khaira G, Segal-Peretz T, Rincon-Delgadillo P A, Li W, Müller M, Nealey P F and de Pablo J J 2015 Molecular

pathways for defect annihilation in directed self-assembly *Proc. Natl. Acad. Sci.* **112** 14144–9

[21] Friedrich J, Unger W, Lippitz A, Koprinarov I, Ghode A and Geng S H 2003 Plasma-based introduction of monosort functional groups of different type and density onto polymer surfaces . Part 1 : Behaviour of polymers exposed to oxygen plasma *Compos. Interfaces* **10** 139–71

[22] Friedrich J, Unger W, Lippitz A, Koprinarov I, Weidner S, Kühn G and Vogel L 1998 *Metallized Plastics 5 and 6: Fundamental and Applied Aspects* ed K Mittal (Utrecht: VSP)

Chapter 4:

Grain-boundary-induced alignment of block copolymer thin films

Abstract:

In this chapter we present and discuss the capability of grain boundaries between horizontally and vertically assembled grains to align block copolymers in thin films. We create these grain boundaries in a controlled manner and use them to direct the self-assembly of a 23.4 nm full-pitch lamellar *PS-b-PMMA* diblock copolymer.

We fabricate arrays of parallel fins making use of the directed self-assembly of block copolymers. For this, we trap an elongated grain of vertically aligned lamellae between two grains of horizontally aligned lamellae which leads to the formation of 90º twist grain boundaries. An energy minimization process makes the block copolymer domains come off perpendicular to the grain boundary. The features maintain their orientation on an average length scale, which can be described by the material's correlation length ξ. As the energy-minimizing feature is the grain boundary itself, the width of the manipulated area (e.g. the horizontally aligned grain) does not represent a critical process parameter. In this chapter, grain-boundary-induced alignment is achieved by the mechanical removal of the neutral brush layer via AFM. The concept is also confirmed by a maskless e-beam direct writing process.

Table of contents: Chapter 4

4.1 Introduction

The shape of grain boundaries in block copolymers and the energy minimization process associated to their formation has been studied quite extensively for bulk materials, and reported in excellent experimental [1] and theoretical [2–5] works.

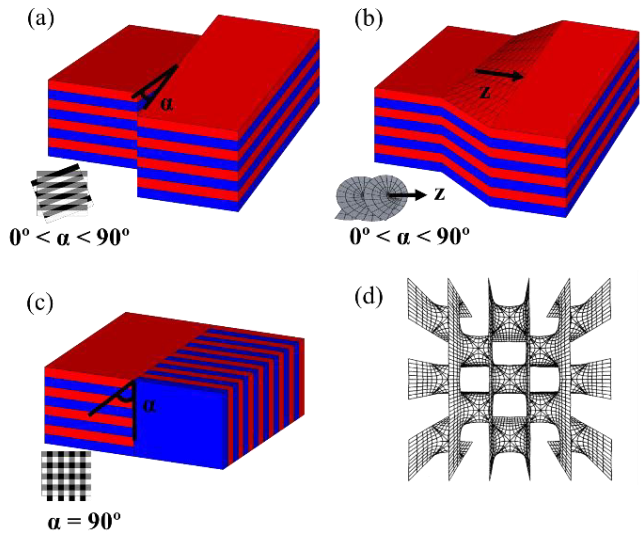

Figure 4.1: Different types of twist grain boundaries and their corresponding inter-material dividing surface (IMDS). a): two grains of lamellar block copolymers under a twist angle α << 90°; the grey areas of the inset represent the IMDS reconstructed in a Scherk surface, b): two grains of lamellar block copolymers under a twist angle α << 90°, the inset represent the IMDS reconstructed in a helicoid shape, c): two grains of lamellar block copolymers under a twist angle of 90°, the grey areas of the inset represent the IMDS reconstructed in a Scherk surface, d): (taken from ref. [6]*) scheme of a first Scherk surface representing the IMDS of c).*

Two relevant types of grain boundaries are the twist grain boundary at one hand (see *figure 4.1*) and the tilt grain boundary on the other hand (see *figure 4.2*). As for lamellar block copolymers, the grain boundary free energy is a function of the area of the intermaterial dividing surface (IMDS) and the stretching and the compression of molecules in the close vicinity of the grain boundary. The material usually tries to reduce the area of the IMDS by stretching and compressing adjacent chains.

For twist angles $\alpha < 15°$ we observe two different reconstruction moduli, which are called helicoid interphase and Scherk first surface [3,5]. The two morphologies coexist for low angles because of their similar grain boundary energies (see *figure 4.1 a)* and *b)*). The major difference between these two morphologies is the shape of the IMDS. There is no major reconstruction mechanism in the formation of helicoid grain boundaries (see shape

of the respective IMDS in inset of *fig. 4.1.b)*). In the second case, the first Scherk surface, the IMDS is reconstructed to a distorted chess board pattern, as excellently described in ref. [2]. The IMDS in these structures can be mathematically described as a first Scherk surface, which forms part of the family of minimal surfaces [7]. The insets of *figures 4.1 a)* and *c)* represent a scheme of the situation inside the grain boundary. Here, white and black areas represent A-A-block interfaces and B-B-block interfaces, respectively. The actual IMDS is represented by the grey areas, which represents A-B-block interfaces. The reconstruction of twist grain boundaries in first Scherk surfaces has been observed experimentally [1,8]. For better understanding, we have plotted a scheme of a first Scherk surface as it occurs in 90º twist grain boundaries in *figure 4.1 d)*. For large twist angles ($\alpha >> 15°$), the formation of first Scherk surfaces is energetically favorable when compared to helicoid grain boundaries. This is at one hand because the helicoid grain boundary massively compresses the lamellae (and therefore the chains) at large angles. On the other hand, the first Scherk surface is by definition a minimal surface that minimizes the IMDS at large twist angles of $\alpha = 90°$.

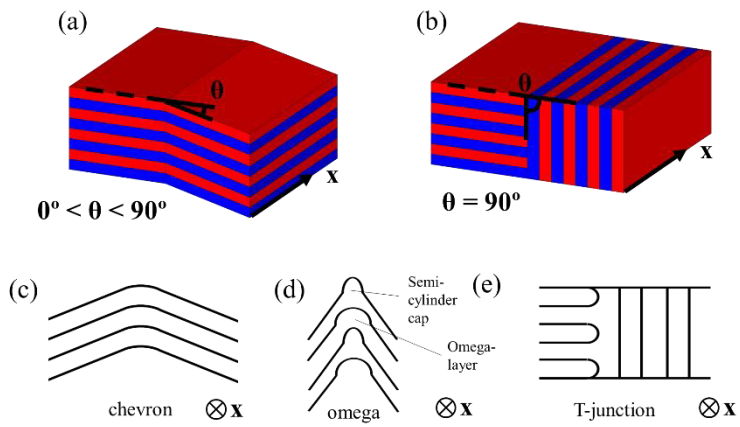

Figure 4.2: Overview of tilt grain boundary morphologies. a): two grains of lamellar block copolymer tilted under an angle well below 90º, b): two grains of lamellar block copolymer tilted under an angle of 90º, c): 2D-scheme of the IMDS of a low-tilt-angle chevron grain boundary, d): 2D-scheme of the IMDS of an omega grain boundary, e): 2D-scheme of the IMDS of a pure T-junction as observed in 90º tilt grain boundaries.

Tilt grain boundaries represent another grain boundary family commonly observed in bulk block copolymer samples. Schemes of two grains under a low tilt angle $\theta << 90^a$ and under a tilt angle $\theta = 90°$ are represented in *figure 4.2 a)* and *b)*. Low angle tilt grain boundaries are sub-divided in so-called chevron tilt grain boundaries and omega tilt grain boundaries. While the chevron tilt grain boundary is rather prominent at low tilt angles,

the omega grain boundary tends to be the result of energy minimization at larger tilt angles [4]. As we can tell from the two sketches depicted in *figure 4.2 c)* and *d)*, both morphologies are similar in appearance. The sequence of the omega-layers and semicylinder caps [4] in omega tilt grain boundaries efficiently minimizes the grain boundary energy at higher angles. When the tilt angle increases even more and θ approaches 90º (see *figure 4.2 b)*), the most efficient manner to minimize the free energy of the system is to interrupt the continuity of one of the species and reorganize them in semicylinder caps as shown in *figure 4.2 e)*.

90º tilt and 90º twist grain boundary structures, as sketched in *figure 4.1 c)* and *figure 4.2 b),* may form in block copolymer thin films, when a vertically oriented grain is adjacent to a horizontally oriented grain. This situation may occur wherever the surface energy changes abruptly from a neutral surface to a highly preferentially wetted surface. Taking into consideration that the block copolymer features on neutral surfaces are upright standing lamellae, the only two structures that may be formed in such grain boundaries are the 90º tilt grain boundary and the 90º twist grain boundary. In ref. [9] the authors argue that the free energy of 90º twist grain boundaries is around half of the free energy of 90º tilt grain boundaries, which heavily benefits the formation of twist grain boundaries. This calculation is moreover supported by the fact that 90º twist grain boundaries, and the resulting tendency to form Scherk's first surface IMDSs, are also observed in the terraced self-assembly horizontally aligned block copolymers on preferentially wetting substrates [10].

The few existing works on 90º twist grain boundaries in relation with block copolymer thin films include, for example, experiments with two chemically patterned plates [11], where the grain boundaries have been observed parallel to the substrate, and a soft graphoepitaxy approach, where 90º twist grain boundaries have been observed for film thicknesses significantly larger than the guiding pattern feature height [12]. Alignment perpendicular to the grain boundary has recently also been observed as a metastable state in the chemoepitaxial alignment of block copolymers [13] referred to by the authors as "stitch morphology". Interestingly, in ref. [14], the authors direct the self-assembly of block copolymers by the creation of structures under the formation of 90º tilt grain boundaries. This effect has for example been evoked by mixing a block copolymer with a determined ratio of its constituent homopolymers and coupled with chemoepitaxy used to direct the material in device-oriented features [15]. Nevertheless, despite of few isolated examples, grain boundaries have not been considered as order-inducing features in the directed self-assembly of block copolymers.

In this work we trap one grain of vertically self-assembled block copolymers between two elongated grains of horizontally aligned block copolymers. We use the 90º twist grain

boundaries on both sides of the trapped grain to direct the self-assembly of the block copolymer in this area without the use of any further guiding patterns.

Grain-boundary-induced alignment is an interesting complementary technique to direct the self-assembly of block copolymers, because it represents a versatile method to align the material on lengths up to its correlation length ξ. The correlation length ξ characterizes the length range where the self-assembly of block copolymers can successfully be directed by grain-boundary-induced alignment. It is inversely proportional to the defect density in the film [16] in fingerprint pattern. Due to the lack of guiding patterns in a stricter sense, grain-boundary-induced alignment does not increase the mean grain size of the material, but rather orients the grains perpendicular to the formed grain boundaries.

4.2 Experimental

4.2.1 Substrate

The substrate are chips cut from a *Si* wafer. Native oxide is not removed. After cleaning the substrate in *isopropyl alcohol* and *acetone*, the substrate undergoes an oxygen plasma treatment for 600 s at 500 W.

4.2.2 Neutral brush layer fabrication

The neutral brush layer consists of grafted *PS-r-PMMA* polymer chains (58 wt% *PS*, 42 wt% *PMMA*, M_p=7.9 $^{kg}/_{mol}$ and polydispersity index 1.85) yielding a film thickness of 6.5 nm (see *figure 4.3 a) panel (1)*). To deposit the neutral brush layer, 1.5 wt% of *PS-r-PMMA* is dissolved in *PGMEA* and the solution is spin-coated to the silicon wafer for 30 s at 5000 rpm. To graft the molecules to the surface, the chip is annealed at 230 ºC in a nitrogen atmosphere for 300 s. The non-grafted molecules are removed by rinsing the sample in *PGMEA*.

4.2.3 Guiding pattern fabrication

In this work we use two different methods to fabricate the guiding patterns.

The guiding pattern fabrication by AFM consists of removing the neutral brush layer in two elongated rectangular areas of 500 nm × 5 µm separated by a distance *d* in the range of few hundreds of nanometers. The brush removal is done by mechanical AFM using the contact mode of a *Dimension Icon / Nanoscope V* AFM by *Bruker*. The tips used in these experiments (*OTESPA*, *Si*-tip with nominal spring constant 42 $^{N}/_{m}$) have a nominal apex radius of 7 nm in the unused state. We estimate the contact force for the probed deflection set-points to be between 0.26 µN and 2.25 µN. The AFM height image shown in *figure 4.3 b)* shows the efficiency of the polymeric brush layer removal as a function of the contact force. The contact force has been increased by 0.26 µN for each segment

of the spiral going from the inside to the outside. The fabrication of the structures presented in this *chapter* have been conducted with nominal contact force of 1.04 µN, because this condition represents the minimum required force to remove the polymer film down to the substrate. This step of the work-flow is depicted in *figure 4.3 a), panel 2.a.*

The second approach to fabricate the guiding patterns is based on the modification of the brush layer by direct e-beam exposure. The exposure has been performed in a *RAITH 150 (TWO)* electron lithography tool at a nominal beam diameter of 2 nm. We expose lines of 50 µm in length and between 65 nm and 500 nm in width, separated by between 500 nm and 65 nm. This concept is sketched in *figure 4.3 a), panel 2.b*, where the electron beam exposed area is depicted in light red. We follow the procedure explained in ref. [17], where the neutral brush layer is exposed to an electron beam with 20 kV acceleration voltage and a sample current of 330 pA. The exposure dose is 256 $^{mC}/_{cm^2}$.

4.2.4 Block copolymer deposition

The diblock copolymer used in these experiments is a *PS-b-PMMA* consisting of 42 wt% *PS* and 58 wt% *PMMA*. Upon self-assembly, this material forms 23.4 nm full-pitch lamellar features. Its polydispersity index *PDI* is 1.1, and the molecular weight is 42.3 $^{kg}/_{mol}$. A 1.7 wt% solution of the polymer in *PGMEA* is deposited by spin coating for 30 s at 2500 rpm and subsequently annealed for 600 s in a N_2 atmosphere at 230 ºC. This process yields a film thickness of 24 nm in free surface. The result of the self-assembly process is sketched in *figure 4.3 a), panel 3.*

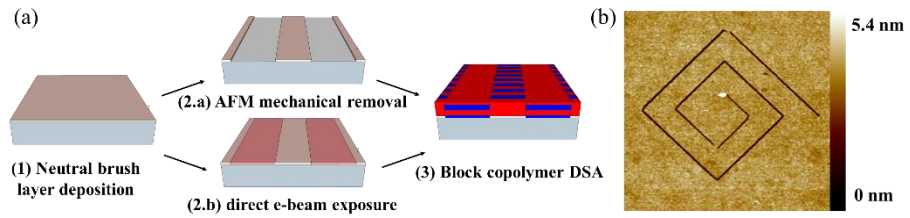

Figure 4.3: Alignment principle and work-flow. a): work-flow to direct the self-assembly of block copolymers by grain-boundary-induced alignment, b): force-dependence of the mechanical brush removal while successively increasing the contact force from 0.26 µN to 2.25 µN from the inside to the outside of the spiral.

4.2.5 Pattern transfer

The pattern transfer consists of two steps. At first, the *PMMA* block is removed in a selective dry etching step in an *Alcatel AMS 110 DE* ICP RIE. We used etching conditions similar to those previously successfully developed and used by the authors of ref. [18]: a gas mixture of 200 sccm *Ar* and 10 sccm O_2 with at 200 W source power and 5 W substrate power. The etch selectivity of *PS* with respect to *PMMA* in this process is 1:3

with *PS* being the more resistant material. The etching time for this step is 21 s. For the subsequent *Si* etching we use the same RIE tool with a plasma power of 1200 W and a substrate power of 10 W for 12 s. The used gases are 30 sccm SF_6 and 25 sccm C_4F_8. We employ an etch process in which both gases are injected in the reaction chamber in a non-pulsed fashion. For more information about these two pattern transfer processes and more detailed information about results they yield, refer to *annex 1* of this thesis.

4.2.6 GISAXS analysis

GISAXS measurements of a representative sample have been conducted at the *P03 Micro- and Nanofocus X-Ray Scattering Beamline* at *PETRA III* in Hamburg [19]. The sample-detector distance was 5800 mm and the radiation wavelength 0.107 nm. The incidence angle of the beam was 0.4°. The detector that has been used for these experiments is a PILATUS 300k pixel detector with a readout time $t < 3\ ms$ and a pixel size of 172 µm.

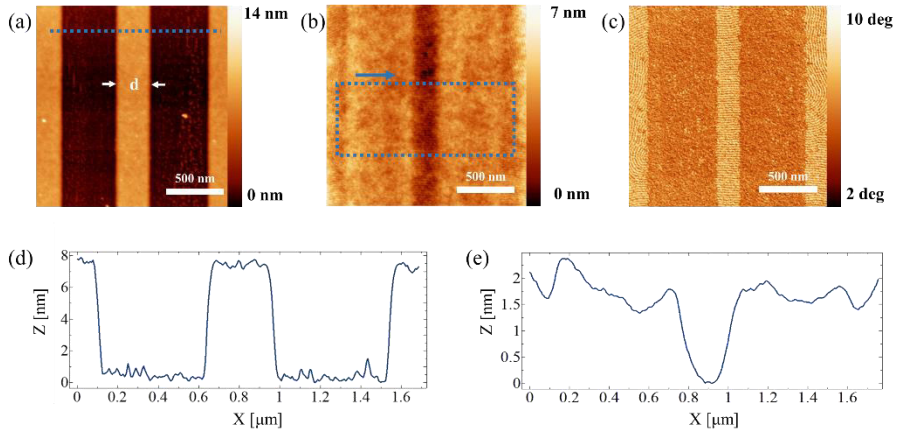

Figure 4.4: Results of grain-boundary-induced alignment via AFM mechanical removal. a): AFM height image of brush layer with two areas treated by m-AFM without brush layer, b) AFM height image of DSA on area depicted in a), c): AFM phase image of b), d): single line profile along blue dashed line in a), (e) average height profile as indicated by the box in b).

4.3 Results

4.3.1 Fabrication and DSA via mechanical AFM (m-AFM)

For the first set of experiments we have removed the neutral brush layer in areas of 500 nm x 5 µm by means of mechanical AFM. The width of those areas has been chosen such that the resulting structures to have a reasonable size for later characterization. The mechanical removal uncovers the underlying silicon substrate, which is preferentially wetted by *PMMA*. The preferential wetting of silicon by *PMMA* leads to the formation of

horizontal lamellae. For block copolymer film thicknesses in the range of L_0 the top material is thus *PMMA*, while the top-layer consists of *PS,* when the film thickness is in the range of *1.5* L_0. In order to dissolve the pile-ups of removed random copolymer the sample has undergone a *PGMEA* rinsing step before taking the AFM height image in *figure 4.4 a)*. This procedure is, however, not usually part of the fabrication process. The distance *d* of the two modified zones depicted in *figure 4.4 a)* is 300 nm. The result of the directed self-assembly on these guiding patterns is depicted in an AFM height image (*figure 4.4 b)*) and phase image (*figure 4.4 c)*). Profiles revealing the sample topography perpendicular to the modified areas before and after the directed self-assembly step are presented in *figure 4.4 d)* and *e)*. The measured height step of approximately 7 nm corresponds to the height of the random copolymer layer, which has been entirely removed. The self-assembled block copolymer structures have a notably shallower topography of around 2 nm. The block copolymer in the trapped grain adapts its thickness to the height of the adjacent horizontally self-assembled grains.

4.3.2 Fabrication and DSA via e-beam direct exposure

The second studied case is the surface modification by e-beam, where we make use of the modification of the neutral brush layer due to interaction with charged particles [17]. For relatively high exposure doses (e.g. 256,000 $^{\mu C}/_{cm^2}$), we observe that the exposed, previously neutral, surface is now preferentially wetted by *PMMA* which leads to horizontal self-assembly. Results of self-assembly in the direct vicinity of a 65 nm wide line and a 65 nm wide pristine area are depicted in the *panels a)* and *b)* of *figure 4.5*. The orientation of the block copolymer perpendicular to the grain boundary is explained by the energy minimization in the grain boundary and the formation of 90º twist grain boundaries.

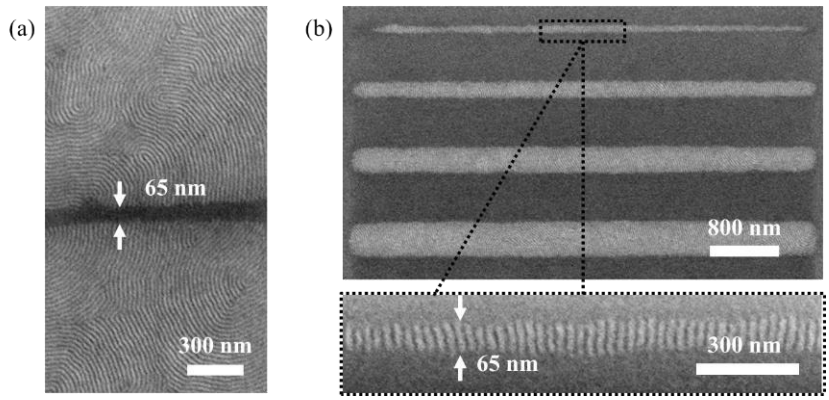

Figure 4.5: Results of grain-boundary-induced alignment obtained by the surface modification by e-beam direct writing. a): horizontal self-assembly on a 65 nm wide stripe, b): vertical self-assembly (e.g. grain-boundary-induced alignment) on stripes of different widths with a minimum of 65 nm.

4.3.3 Pattern transfer

As depicted in *figure 4.6,* the pattern transfer process consists of two steps. After the guiding pattern fabrication (*4.6 a)*) and the self-assembly (*4.6. b)*), it is necessary to remove the *PMMA*, so that the remaining *PS* part of the block copolymers matrix can serve as an etch mask. This process step is displayed in *figure 4.6. c),* where the bright lines correspond to *PS* features and the dark lines correspond to the voids created by removed *PMMA*. The *PMMA* removal can effectively be done using various oxygen-containing gas mixtures, such as Ar/O_2 or CHF_3/O_2. *PS*, in turn, is relatively inert towards oxygen-containing plasma etch processes, enabling an etch selectivity around 3.

Secondly, we use the remaining *PS* template as an etch mask to transfer the defined features into silicon. The result of the pattern transfer into silicon is depicted in *figure 4.6 d)*. A great advantage for the fabrication of devices with this technique is that the horizontally aligned block copolymers serve as an etch mask and preclude the chemical attack of Si in this area. If the process is conducted on a SOI wafer, these areas can subsequently be contacted and used as electrical contacts, because the silicon below is intact. This work-flow may represent a simple method for the fabrication of dense nanowire arrays by grain-boundary-induced alignment, for the fabrication of nanoelectronic devices.

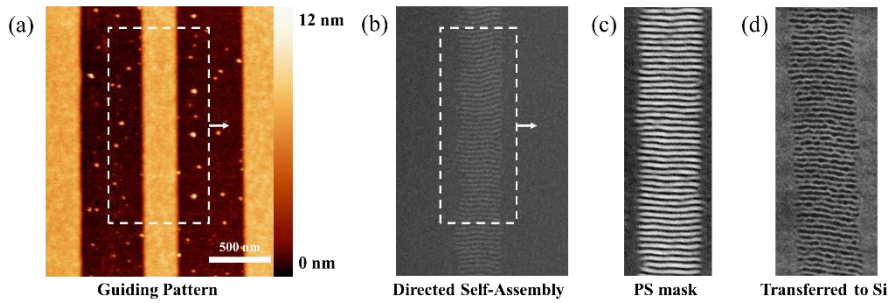

Figure 4.6: Micrographs of different fabrication stages in the pattern transfer process. a): AFM image of m-AFM treated area for grain-boundary-induced alignment, b): DSA of block copolymers on the presented guiding pattern, while the excerpt corresponds to area surrounded by dashed line in a), c): PS etch mask after selective removal of PMMA via RIE (area corresponds to white dashed line in b)), d): pattern transferred into silicon.

4.4 Discussion

4.4.1 Surface energy modification by m-AFM

As the surface energy modification of a polymeric brush layer by direct e-beam exposure has been successfully done and reported elsewhere [17], in this section we will focus on the surface energy modification induced by the m-AFM step.

The analysis of the wetting behavior of a homopolymer blend consisting of the components of the block copolymer can serve as a qualitative test for the surface energy in micrometric areas [20,21]. Here, we use this technique to qualitatively understand the surface energy by observing the behavior of a *PS/PMMA* blend in the modified and in the non-modified area. Phase separation of *PS* and *PMMA* is induced by the annealing of the film at 230 ºC for few minutes. To be capable of distinguishing the two polymers more easily in the SEM images, we subjected the sample to an 18 s oxygen plasma treatment at 500 W source power. Due to the higher etch resistivity of *PS* with respect to *PMMA*, we expect the *PMMA* droplets to be recessed in height. The results are depicted in two SEM images and two explanatory sketches in *figure 4.7*. *Figure 4.7 a)* shows the behavior of the polymer blend in the close vicinity of a 5 µm × 50 µm stripes, where the neutral brush layer has been removed by means of m-AFM. In *figure 4.7 b)* we observe a behavioral difference of the polymer blend between the modified area and the pristine area in more detail.

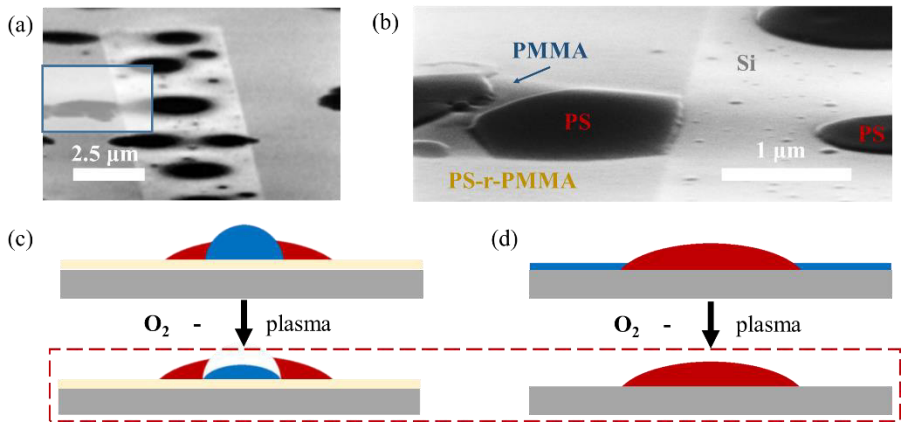

Figure 4.7: Qualitative analysis of PS/PMMA blends on neutral surfaces and on surfaces modified by m-AFM. a): Overview SEM image of PS/PMMA blend in two modified areas (stripes) and their direct pristine vicinity covered with neutral brush layer, b): close-up of the part of a)indicated by the light blue line, c): explanatory sketch of the architecture of the droplet sketched on the left side of b) before and after the oxygen plasma treatment, d): explanatory sketch of surface on the right side of image b)

The phase-separated *PS/PMMA* droplet in the pristine area of the sample in *figure 4.7 b)* is sketched in *figure 4.7 c)* and provides valuable insight in the behavior of polymer blends on neutral surfaces. The slightly recessed part of the droplet corresponds to a *PMMA* droplet inside a *PS* droplet due to the O_2 plasma treatment. This indicates that both polymers have very similar interface energies with respect to the neutral brush layer. The surface energy of *PMMA* (with respect to the air) is slightly higher than the one of

PS [22], which justifies that the *PMMA* droplet is inside the *PS* droplet and not vice versa. A similar behavior has been observed before [20,21].

In contrast, we do not observe these characteristic twin-droplets in the modified areas. This behavior is explained by a homogenous coverage of the silicon by *PMMA*, because the interface energy between the activated silicon and *PMMA* is significantly lower than between silicon and *PS*. The *PS* thus minimizes its surface energy through the formation of droplets on top of the *PMMA* layer. This concept is sketched in *figure 4.7 d).*

This experiment demonstrates that the surface energy is efficiently modified when the neutral brush layer is removed by m-AFM.

4.4.2 Fixed-height self-assembly

Transferring the created block copolymer patterns into the underlying substrate is a key step that converts block copolymer lithography into a purposeful technique for semiconductor manufacturing. Here, the pattern transfer process is particularly challenging, because *polystyrene* and *poly(methyl methacrylate)* are chemically similar. Despite of *PS* being chemically relatively inert, it does by far not show etch resistances as large as an inorganic hard mask would do. This leads to fast mask wear and requires exact knowledge about the film thickness of the initial block copolymer film to design a successful pattern transfer process. Nanometric fluctuations of the block copolymer thickness throughout the wafer / chip area due to microscopic impurities or other process-related issues may lead to difficulties in the pattern transfer process.

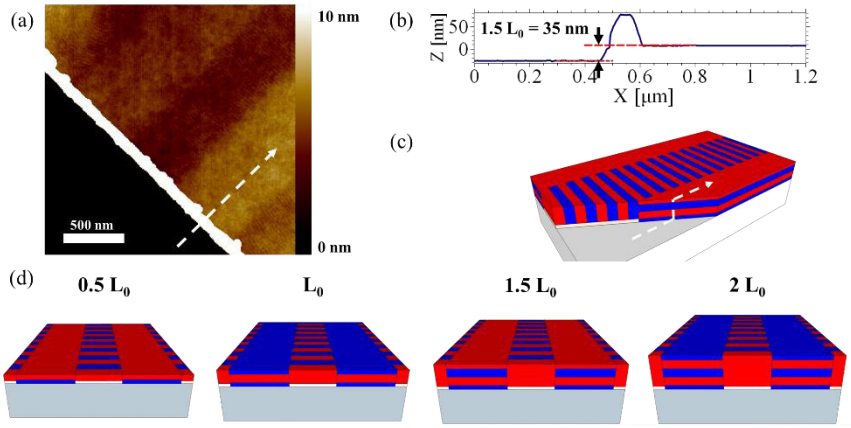

Figure 4.8: Measuring the height step between substrate and horizontally aligned block copolymer lamellae. a): AFM height image of prepared sample, b): single line profile indicated by white dashed line in a), c):3D sketch of the measurement presented in a), d): possible self-assembly morphologies with height quantized to from 0.5 L_0-2L_0 in steps of 0.5 L_0.

The self-assembly of block copolymers between two grain boundaries is quantized to multiples of 0.5 L_0, because of the adjacent horizontally oriented grains' quantized height. This concept is clarified in *figure 4.8*, where we present a measurement of the block copolymer height in the horizontally aligned (and previously modified) area. The block copolymer has been removed by m-AFM in an area orthogonal to the long axis of the modified area, and an AFM height image of one part of the sample is depicted in *figure 4.8 a)*. A single line AFM height profile is shown in *figure 4.8 b)*. The profile's precise location and direction is indicated by the white dashed line both in the sketch and in the actual height image. The step height is 35 nm, which corresponds to 1.5 L_0 (with L_0 being 23.4 nm, as we have found in *chapter 2*). Based on the knowledge that the silicon wafer is preferentially wetted by *PMMA*, we conclude that the top layer must be *PS*, as sketched in *figure 4.8 c).*

Figure 4.8 d) presents a sketch of four different self-assembly heights in steps of 0.5 L_0. We would like to state at this point that the horizontally aligned areas will self-assemble in a quantized state such that the film height in the horizontally aligned area is always an integer multiple of 0.5 L_0. Interestingly, we observe in all our experiments that the self-assembly of block copolymers in the vertically aligned trapped grain is about three nanometers recessed with respect to the horizontally aligned grains. The opposite has been observed by other authors in a similar experiment [23], where the vertically assembled block copolymer domain is few nanometers higher than the horizontally aligned domain.

4.4.3 Limits of grain-boundary-induced alignment

An important feature of the ordering of block copolymers via grain-boundary-induced alignment is that this technique does not require the fabrication of a high-resolution guiding pattern as it is the case for chemoepitaxy and graphoepitaxy. This comes, however, at the expense of the fact that the maximum alignment length is limited by the correlation length ξ of the block copolymer. To estimate a reasonable maximum distance d between the two horizontally aligned grains, we have to investigate the grain size distribution of the block copolymer finger print after self-assembly.

In *figure 4.9* we present an estimation of the block copolymer correlation length based on the GISAXS pattern depicted in *figure 4.9 a),* similar to the way it has already been discussed elsewhere (see *chapter 2B* of this thesis and refs. [24,25]). Moreover, we present an analysis of the width of the first order grating truncation rod (GTR) in *figure 4.9 b),* and an SEM image indicating the estimated mean grain size in *figure 4.9 c).*

It is well-known that block copolymer self-assembly is a process based on grain nucleation and subsequent growth, also referred to as coarsening [26]. Characterization

techniques like small-angle X-ray scattering (SAXS), depolarized light scattering (DPLS) [27] and grazing-incidence small-angle X-ray scattering (GISAXS) [24] are capable of providing mean values [28] for the grain sizes in block copolymers (e.g. correlation length). Nevertheless, the provided value does not a priori contain information about the grain size distribution. The experimental analysis of the grain size in the self-assembly of horizontally aligned diblock copolymers by AFM has been demonstrated to be in excellent agreement with a log-normal distribution function [29]:

$$f(\ln(\xi)) = \frac{1}{\sqrt{2\pi}*\ln(\sigma)} * exp\left\{-\frac{(\ln(\xi)-\ln(\mu))^2}{2*ln^2(\sigma)}\right\} \qquad (4.1)$$

with σ being the geometric standard deviation and μ being the number-based geometric mean, equivalent to the mode diameter of the grain.

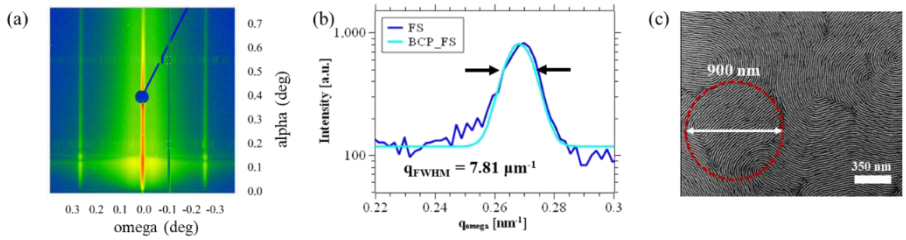

Figure 4.9: Estimating the limits of the directed self-assembly by grain-boundary-induced alignment. a): GISAXS pattern of randomly assembled block copolymer features, b): estimation of the FWHM of the block copolymer GTR to estimate the mean correlation length ξ of the sample, c): SEM image of finger-print pattern with a circle representing the mean grain size as determined by the analysis of the GISAXS pattern.

The authors of ref. [29] suggest that the block copolymer grain size can be described by a Smoluchowski coagulation function, for which σ=1.45; usually used for systems where particle trajectories are controlled by Brownian motion. If the correlation length ξ_{GISAXS} as determined by the GISAXS line width analysis corresponds to the mean correlation length of all grains is in the thin film (in this case $\bar{\xi}$=900 nm), we can estimate that the grain size distribution $f(ln(\xi))$ of our sample is:

$$f(\ln(\xi)) = \frac{1}{\sqrt{2\pi}*\ln(1.45)} * exp\left\{-\frac{(\ln(\xi)-\ln(731.7))^2}{2*ln^2(1.45)}\right\} \qquad (4.2)$$

(plotted in *figure 4.10 a)*) because in this way

$$\xi_{mean} = \frac{\int_0^\infty \xi * f(\ln(\xi))d\xi}{\int_0^\infty f(\ln(\xi))d\xi} = 900\ nm \qquad (4.3)$$

Knowing the approximate grain size distribution of our block copolymer in free surface $f(\ln(\xi))$, we can estimate the probability p [%], that a grain of the sample is smaller than a determined value ξ_0 with:

$$p(\xi_0) = 100 * \frac{\int_0^{\xi_0} f(\ln(\xi))d\xi}{\int_0^{\infty} f(\ln(\xi))d\xi}[\%] \qquad (4.4)$$

Furthermore, we subdivide the particle distribution function in *figure 4.10 a)* in a red and a blue area. The surface area of the red part divided by the total area represents the probability $p(\xi_0)$ that an areal unit forms part of a grain smaller than $\xi_0 = 450\ nm$. In this exemplified calculation using *formula (4.4)*, the probability for this event is 4.8 %. Accordingly, 0.3 % of the total area is occupied by grains with the size of 300 nm and merely 7×10^{-10} % of the area is occupied by grains smaller than 65 nm. The self-assembly in structures like the ones we fabricate in this work is by definition only considered to be successful if there is no defect on the entire length *l* of the grain boundary.

(a)

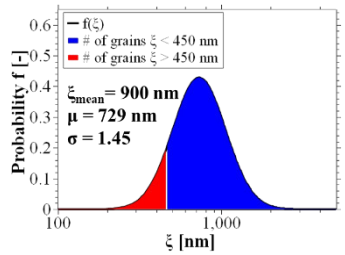

(b)

Distance between two grains d	Probability of defect free self-assembly $p_{\bar{d}}$
65 nm	99.999999 %
300 nm	95,15 %
450 nm	57.89 %

$\xi_{mean} = 900\ nm; l = 5\ \mu m$

Figure 4.10: Grain size analysis in block copolymer thin films. a): Grain size distribution for the block copolymer in free surface for ξ_{mean}=900 nm, b): table with results for the probability of defect free self-assembly between a 5 µm grain boundary for three characteristic distances d between the grains.

We can estimate the probability $p_{\bar{d}}$ of this event by estimating the probability that all the grains along the grain boundary with the length *l* are at least as large as the distance *d* between the two grain boundaries, which is given by the term:

$$p_{\bar{d}} = p(\xi_0 = d)^{l/d} \qquad (4.5)$$

In the table presented in *figure 4.10 b)* we present the probability to fabricate a *l* = 5 µm long array without defects for three different lengths of *d*. The values for *d* we worked with in this table are process parameters used in this section. In particular, we have presented the grain boundary-induced alignment with *d* = 300 nm in *figure 4.4* fabricated by m-AFM and d = 65 nm in *figure 4.5* by e-beam direct writing and we observe no or very few defects in these structures – just as predicted by the presented estimation. The fact that a $p_{\bar{d}}(d = 450\ nm)$ yields less than 60 % indicates that the probability to find

defects in such a structure is rather high. An example of a structure with *d = 450 nm* is depicted in *figure 4.11 a)* and we observe the formation of defects.

Based on the presented analysis, the self-assembly of block copolymers by grain-boundary-induced alignment mainly depends on the correlation length ξ of the block copolymer (material parameter), and on the distance d between the two horizontally aligned grains and the length l of the horizontally aligned grains (process parameters). For this reason, it is important to understand the mechanisms of self-assembly and defect-annihilation in detail, which has already been subject to a number of works [16,24,30,31].

The rate at which a block copolymer eliminates defects in the course of the self-assembly process is determined by the energy barrier that has to be overcome in order to annihilate the defect [32]. Here, a smaller energy barrier indicates a faster defect removal mechanism which is expressed by a higher degree of order in the block copolymer. In ref. [32] the authors demonstrate that the energy barrier for the defect removal is inversely proportional to χN. A direct consequence of that is that the correlation length ξ of block copolymers is larger for small-pitch materials (e.g. materials with small χN). This means that an inherent property of grain-boundary-induced alignment is the decreasing number of defects for smaller-pitch materials.

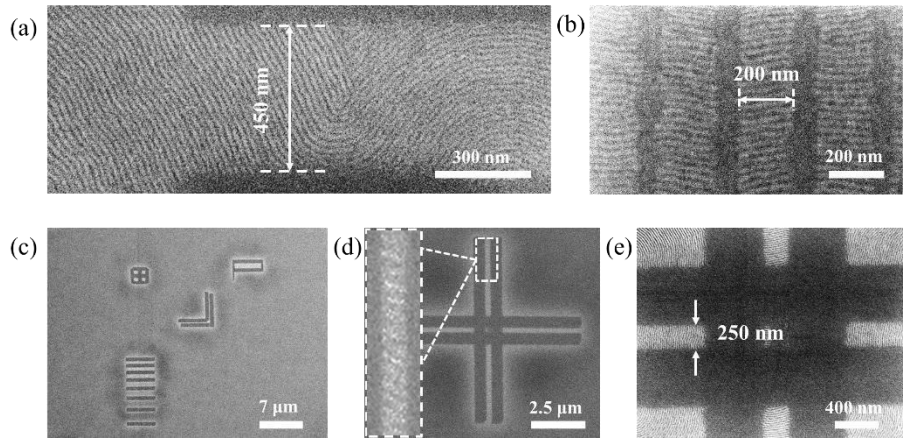

Figure 4.11: Alternative structures fabricated by grain-boundary-induced alignment. a): defective self-assembly due too large distance d between the two grain boundaries, b): self-assembly of nanowire array based on grain-boundary-induced alignment, c): arbitrary figures fabricated by mechanical AFM removal, d)/e): double-bar cross fabricated by mechanical AFM removal and grain-boundary-induced alignment of block copolymers between the cross branches.

The fabrication of patterns to direct the self-assembly of block copolymers by grain-boundary-induced alignment by m-AFM is not limited to trapping one single grain, which

has been the only structure that we have discussed until now. In *figure 4.11 b)-e)* we present alternative structures fabricated by grain-boundary-induced alignment, such as defect-free array of nanowires of 200 nm in length and a pitch of 250 nm in *figure 4.11 b)*. In *figure 4.11 c)* we show a number of geometric shapes that have been fabricated to demonstrate the versatility of the technique. A double-lined cross of 10 µm × 10 µm with a line width of 500 nm and 250 nm spaces between the lines is depicted in *figure 4.11 d)* and *4.11 e)*. The in-set of *panel d)* shows the Moiré pattern between the two branches of the cross, which indicates the high order of the block copolymer without actually having sufficient measurement points to resolve single block copolymer domains. Moiré patterns are interference patterns [33] that occur when a periodic lattice (for example a directed block copolymer pattern) is measured with an imaging technique whose sampling step size is below the step size of the lattice that is supposed to be measured. The existence of the Moiré pattern hence can be understood as a proof for the successfully directed self-assembly of the block copolymers between the two branches of the cross. To verify this thesis, we show a close-up of the center of the fabricated cross in *figure 4.11 e)*, where we doubtlessly see the directed self-assembly of block copolymers is successful in each one of the four trapped grains.

4.4.4 Grain-boundary-induced alignment with ternary blends

For the application of grain-boundary-induced alignment it could be favorable to achieve an alignment mode that is not restricted by the correlation length of the block copolymer. One way to do so is to influence the material is such a way that the preferentially formed grain boundary is a 90º tilt grain boundary (see *figure 4.1. c)*) instead of a 90º twist grain boundary (see *figure 4.2 b)*). This is the case when the vertical interface created by the horizontally ordered block copolymer is energetically more attractive to one block than for the other – similar to the energetic situation in graphoepitaxy.

Duque et al. [34] calculated the free energy in twist and tilt grain boundaries for a pure diblock copolymer and a ternary blend containing 70 % diblock copolymer and a 30 % fraction of homopolymers. The calculation yields that 90º tilt grain boundaries have the same (or in the concrete case of mixing in 30 % homopolymers an almost negligible 2 % lower) grain boundary free energy compared to the 90º twist grain boundary in case of mixing in homopolymers. The 90º twist grain boundary has, in turn, a clear energetic advantage over the 90º tilt grain boundary in case of pure diblock copolymers. Moreover, the absolute grain boundary free energy for the ternary blend is reduced heavily to approximately $^1/_3$ of the value for the pure block copolymer.

We reproduced this experiment using a blend of the 23.4 nm pitch *PS-b-PMMA* and different amounts of *PS* and *PMMA* homopolymers with a molecular weight of 39.5 $^{kg}/_{mol}$ with total accumulated homopolymer fractions between 0 % and 45 %. In all the

experiments the volume fraction of *PS* homopolymer equals the *PMMA* homopolymer fraction. Results of the behavior of the ternary block copolymer/homopolymer blend in the vicinity of a grain boundary is presented in *figure 4.12*. The annotation in the respective SEM images in *figure 4.12* refers to the accumulated homopolymer fraction, which means that "30 % HP" in *figure 4.12 b)* indicates that the ternary blend contains 15 % *PS*, 15 % *PMMA* and 70 % *PS-b-PMMA*.

We observe two different effects caused by the increasing homopolymer fraction. At one hand, we observe a progressive swelling of the block copolymer features due to the accumulation of homopolymer molecules in the center of the domain (because this is the place where the molecules can avoid the energetically unfavorable location close to the IMDS). This effect is accompanied by a decrease of the material's correlation length.

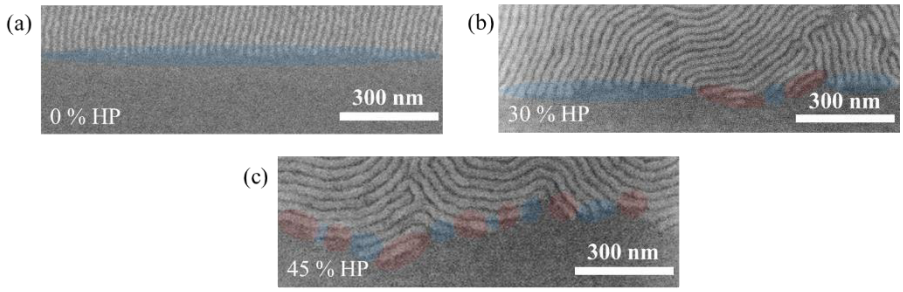

Figure 4.12: Grain boundary evolution as function of homopolymer content in the ternary blend. a): 0 % homopolymer, b): 30 %, c): 45 %; tilt grain boundaries and the blue areas are marked in red and twist grain boundaries are marked in blue.

On the other hand, we observe that the proportion of tilt grain boundaries rises upon increasing the homopolymer ratio. Those parts of the grain boundary that correspond to a tilt grain boundary are red shaded, while twist grain boundaries are marked blue (see *figure 4.12*). As a general trend we can state, that the block copolymer is more likely to form tilt grain boundaries at increasing homopolymer fractions. This behavior is explained by the reduction of the free energy difference between the two grain boundary morphologies. The formation of tilt grain boundaries does, however, not convert into the energetically clearly favorable state. The proportion of tilt grain boundaries and twist grain boundaries for the 45 % homopolymer sample is approximately equal, as shown in *figure 4.12 c).* This observation indicates that the energetic difference between the two states is very low.

The desired situation is, however, only achieved if the formation of a tilt grain boundary is energetically favorable for one particular block, but not for the other one. This effect may be better understood when we consider ref. [35], where the authors observe that

added *PS*-coated *Au* nanoparticles accumulate particularly in grain boundaries. There, the nanoparticles minimize the A/B interface area of the – in that case – *PS-b-PEO* block copolymer in favor of the *PS*-block. The alignment of block copolymers via grain-boundary-induced alignment parallel to the grain boundary can be successful, in case two prerequisites are fulfilled: *(i)* the total homopolymer fraction in the blend is large enough to lower the tilt grain boundary free energy significantly and *(ii)* the ratio of the two homopolymers in the blend is sufficiently asymmetric that the tilt grain boundary is reduced significantly more for one block than for the other.

In ref. [36] the authors make use of asymmetric ternary blends with a total of 40 % homopolymers (e.g. 29 % *PMMA* and 11 % *PS*) to provoke the formation of tilt grain boundaries. The alignment of the block copolymers in that work, is however accompanied by the use of high-resolution chemical guiding patterns, which we believe would not be necessary for sufficiently high-correlation-length blends. The effect of having worked with a ternary blend could represent an explanation for unusual self-assembly morphology that is observed, but not further explained, in ref. [23].

4.5 Conclusions

The directed self-assembly of block copolymers is possible either by the controlled removal of an intermediate polymeric brush layer or its surface modification. We have shown this concept using both a probe-based mechanical removal approach and an electron-beam direct writing approach.

The driving force of the self-assembly is an energy minimization process in the grain boundary between horizontally and vertically assembled block copolymers. This specific grain boundary is referred to as 90º twist grain boundary, where the *PS*/*PMMA* surface is reduced to a first Scherk surface, which mathematically represents a minimal surface. Because this approach lacks any kind of guiding pattern along the self-assembly direction, the correlation length ξ is the limiting factor for the self-assembly in grain-boundary-induced alignment and deserves profound analysis. Understanding the parameters that influence the correlation length of block copolymer thin films in the annealing step is most likely to lead to an improved performance of block copolymer self-assembly in grain-boundary-induced alignment.

For this reason, grain-boundary-induced alignment may represent a particularly interesting alternative for early stage testing of new high-χ, low-pitch block copolymers with large correlation lengths. A recent report on the self-assembly of sub-5 nm liquid crystals (with a remarkably high degree of intrinsic order) has shown that the alignment

of very small features by means of graphoepitaxy may be perturbed by large guiding pattern roughness [37]. Grain-boundary-induced alignment offers one possible solution for upcoming challenges that may be encountered by graphoepitaxy (and also chemoepitaxy), which is the difficulty to provide reliable guiding patterns for very small pitch self-assembling materials. Grain-boundary-induced alignment, in turn, favors the directed self-assembly of materials with small pitches due to their large correlation length.

4.6 References

[1] Thomas E L, Anderson D M, Henkee C S and D H 1988 Periodic area-minimizing surfaces in block copolymers *Nature* **334** 598–601

[2] Gido S P and Thomas E L 1994 Lamellar Diblock Copolymer Grain Boundary Morphology. 2. Scherk Twist Boundary Energy Calculations *Macromolecules* **27** 849–61

[3] Gido S P and Thomas E L 1997 Lamellar Diblock Copolymer Grain Boundary Morphology. 3. Helicoid Section Twist Boundary Energy *Macromolecules* **30** 3739–46

[4] Gido S P and Thomas E L 1994 Lamellar Diblock Copolymer Grain Boundary Morphology. 4. Tilt Boundaries *Macromolecules* **27** 6137–44

[5] Gido S P, Gunther J, Thomas E L and Hoffman D 1993 Lamellar diblock copolymer grain boundary morphology. 1. Twist boundary characterization *Macromolecules* **26** 4506–20

[6] Diekers U, Hildebrandt S and Sauvigny F 2010 *A Serries of Comprehensive Studies in Mathematics: Minimal Surfaces* (Heidelberg: Springer)

[7] Helfand E and Wasserman Z R 1976 Block Copolymer Theory. 4. Narrow Interphase Approximation *Macromolecules* **9** 879–88

[8] Jinnai H, Sawa K and Nishi T 2006 Direct observation of twisted grain boundary in a block copolymer lamellar nanostructure *Macromolecules* **39** 5815–9

[9] Jeong S, Moon H, Shin J, Kim B H, Shin D O, Kim J Y, Lee Y, Kim J U and Kim S O 2010 One-Dimensional Metal Nanowire Assembly via block copolymer soft graphoepitaxy *Nano Lett.* **10** 3500–5

[10] Carvalho B L and Thomas E L 1994 Morphology of Steps in Terraced Block Copolymer Films *Phys. Rev. Lett.* **73** 3321–4

[11] Liu G, Ramirez-Hernandez A, Yoshida H, Nygard K, Satapathy D K, Bunk O, de Pablo J and Nealey P F 2012 Morphology of Lamellae-Forming Block Copolymer Films between Two Orthogonal Chemically Nanopatterned Striped Surfaces *Phys. Rev. Lett.* **108** 1–5

[12] Jeong S J, Moon H S, Shin J, Kim B H, Shin D O, Kim J Y, Lee Y H, Kim J U and Kim S O 2010 One-dimensional metal nanowire assembly via block copolymer soft graphoepitaxy *Nano Lett.* **10** 3500–5

[13] Raybin J, Ren J, Chen X, Gronheid R, Nealey P F and Sibener S J 2017 Real-Time Atomic Force Microscopy Imaging of Block Copolymer Directed Self Assembly *Nano Lett.* **17** 7717–23

[14] Oria L, Ruiz de Luzuriaga A, Alduncín J a. and Pérez-Murano F 2012 Block co-polymer guided self-assembly by surface chemical modification: optimization of multiple patterning process and pattern transfer *Proc. SPIE* **8323** 27-1–7

[15] Stoykovich M P, Muller M, Kim S O, Solak H H, Edwards E W, de Pablo J J and Nealey P F 2005 Directed assembly of block copolymer blends into nonregular device-oriented structures *Science.* **308** 1442–6

[16] Murphy J N, Harris K D and Buriak J M 2015 Automated defect and correlation length analysis of block copolymer thin film nanopatterns *PLoS One* **10** 1–32

[17] Evangelio L, Fernández-Regúlez M, Borrisé X, Lorenzoni M, Fraxedas J and Perez-Murano F 2015 Creation of guiding patterns for directed self-assembly of block copolymers by resistless direct e-beam exposure *J. Micro/Nanolith. MEMS MOEMS.* **14** 033511-1–6

[18] Satake M, Iwase T, Kurihara M, Negishi N, Tada Y and Yoshida H 2013 Characteristics of selective PMMA etching for forming a PS mask *Proc. SPIE* **8685** T1–7

[19] Buffet A, Rothkirch A, Döhrmann R, Körstgens V, Abul Kashem M M, Perlich J, Herzog G, Schwartzkopf M, Gehrke R, Müller-Buschbaum P and Roth S V. 2012 P03, the microfocus and nanofocus X-ray scattering (MiNaXS) beamline of the PETRA III storage ring: The microfocus endstation *J. Synchrotron Radiat.* **19** 647–53

[20] Lorenzoni M, Evangelio L, Nicolet C, Navarro C, San Paulo A and Perez Murano F 2015 Nanomechanical properties of solvent cast PS and PMMA polymer blends and block co-polymers *J. Micro/Nanolith. MEMS MOEMS.* **14** 033509-1--6

[21] Evangelio L, Fernández-Regúlez M, Fraxedas J, Müller M and Perez-Murano F 2018 Role of Surface Softness in Directed Self-Assembly of Block Copolymers *submitted* **n/a** n/a

[22] N/A Solid surface energy data (SFE) for common polymers *12/06/18* http://www.surface-tension.de/solid-surface-energy

[23] Oria L, Ruiz De Luzuriaga A, Alduncin J A and Perez-Murano F 2013 Polystyrene as a brush layer for directed self-assembly of block co-polymers

Microelectron. Eng. **110** 234–40

[24] Perego M, Ferrarese Lupi F, Ceresoli M, Giammaria T J, Seguini G, Enrico E, Boarino L, Antonioli D, Gianotti V, Sparnacci K and Laus M 2014 Ordering dynamics in symmetric PS-b-PMMA diblock copolymer thin films during rapid thermal processing *J. Mater. Chem. C* **2** 6655–64

[25] Choi J, Gunkel I, Li Y, Sun Z, Liu F, Kim H, Carter K R and Russell T P 2017 Macroscopically ordered hexagonal arrays by directed self-assembly of block copolymers with minimal topographic patterns *Nanoscale* **9** 14888–96

[26] Chastek T Q and Lodge T P 2006 Grain shapes and growth kinetics during self-assembly of block copolymers *J. Polym. Sci. Part B Polym. Phys.* **44** 481–91

[27] Wang X, Chintapalli M, Newstein M C, Balsara N P and Garetz B A 2016 Characterization of a Block Copolymer with a Wide Distribution of Grain Sizes *Macromolecules* **49** 8198–208

[28] Smilgies D M 2009 Scherrer grain-size analysis adapted to grazing-incidence scattering with area detectors *J. Appl. Crystallogr.* **42** 1030–4

[29] Limary R and Green P F 2002 Late-stage coarsening of an unstable structured liquid film *Phys. Rev. E - Stat. Physics, Plasmas, Fluids, Relat. Interdiscip. Top.* **66** 2–7

[30] Ceresoli M, Volpe F G, Seguini G, Antonioli D, Gianotti V, Sparnacci K, Laus M and Perego M 2015 Scaling of correlation length in lamellae forming PS-b-PMMA thin films upon high temperature rapid thermal treatments *J. Mater. Chem. C* **3** 8618–24

[31] Ruiz R, Bosworth J K and Black C T 2008 Effect of structural anisotropy on the coarsening kinetics of diblock copolymer striped patterns *Phys. Rev. B - Condens. Matter Mater. Phys.* **77** 1–5

[32] Li W, Nealey P F, De Pablo J J and Müller M 2014 Defect removal in the course of directed self-assembly is facilitated in the vicinity of the order-disorder transition *Phys. Rev. Lett.* **113** 1–5

[33] Hexemer A, Stein G E, Kramer E J and Magonov S 2005 Block copolymer monolayer structure measured with scanning force microscopy moiré patterns *Macromolecules* **38** 7083–9

[34] Duque D, Katsov K and Schick M 2002 Theory of T junctions and symmetric tilt grain boundaries in pure and mixed polymer systems *J. Chem. Phys.* **117** 10315–20

[35] Listak J and Bockstaller M R 2006 Stabilization of grain boundary morphologies in lamellar block copolymer/nanoparticle blends *Macromolecules* **39** 5820–5

[36] Stoykovich M P, Kang H, Daoulas K C, Liu G, Liu C C, De Pablo J J, Müller M

and Nealey P F 2007 Directed self-assembly of block copolymers for nanolithography: Fabrication of isolated features and essential integrated circuit geometries *ACS Nano* **1** 168–75

[37] Nickmans K, Murphy J N, Waal B De, Leclère P, Doise J, Gronheid R, Broer D J and Schenning A P H J 2016 Sub-5 nm Patterning by Directed Self-Assembly of Oligo (Dimethylsiloxane) Liquid Crystal Thin Films *Adv. Mater.* **28** 10068–72

Chapter 5:

Thermal imaging of block copolymers with sub-10 nm resolution

Abstract:

We present a probe-based thermal imaging technique capable of providing sub-10 nm lateral resolution. We demonstrate this resolution by resolving microphase separated *PS-b-PMMA* block copolymers with molecular weights ranging from 42 $^{kg}/_{mol}$ to 79 $^{kg}/_{mol}$ that self-assemble in structures with half-pitch widths between 11 nm and 19 nm. At each pixel location, a resistively heated tip is brought in contact with the surface, and the power dissipated into the sample is quantified. The excellent lateral resolution of the presented technique is based on the use of very sharp resistively heated tips with apex radii of < 5 nm. We are capable of measuring the thermal transport into the sample with a resolution of < 0.1 µW. The difference in detected heat transfer between the *PS* domain of the measured block copolymers and the *PMMA* domain is in the range of 20 %. The presented technique represents an interesting way to image complex mixed polymeric systems with high resolution and a good material contrast based on the differences in the material's thermal conductivity.

Table of contents: Chapter 5

5.1 Introduction

The impressive increase in device density in modern microprocessors has been accompanied by a notable increase in power density raising the need for efficient thermal management on chips [1]. As the size of nano-devices decreases, effects like self-heating play a limiting role in their design [2]. Great effort has been put into taking thermal images of nanoscale hot spots [3] and even of operating nano-devices [4,5] with impressive results. The referenced examples justify the importance of thermal properties of materials and devices with the highest-possible resolution.

Thermal properties of samples can be measured by four [6] different temperature-dependent effects, namely thermovoltage [7], electrical resistance [8], fluorescence [9] and thermal expansion [10].

Besides their important role in the development of nano-patterning processes [11,12], heated AFM tips have found application in the study of thermal properties of materials [13] and devices [4], because their small apexes are capable of providing a high spatial imaging resolution. The use of scanning probe microscopy to map variations in thermal conductivity with high resolution has first been demonstrated in 1992 [14]. One recent application is the measurement of thermal transport into graphene as a function of the layer-thickness [15]. Many works on thermal high-resolution imaging of, for example, inorganic films [16], and ultra-high vacuum approaches [17] are restricted in their resolution due to the size of the tip-sample contact area. Studies of the glass transition temperature of polymers in thin films, especially *PS* and *PMMA* [18] with probe sizes in the micrometer-range have moreover led to interesting results. Thermal AFM has moreover been used as tool to measure heat transport properties of polymer blends [19] and single crystalline polymer fibers [20] considered for electronic packaging applications.

The contactless analysis of nano-scale heat transport usually requires ultra-high vacuum and complicated computational modeling [21]. Studies of radiative heat transfer in the extreme near field in very good agreement with theory have been presented [22] albeit lateral resolution has not been optimized yet. In this *chapter* we present a thermal imaging technique that enables the measurement of power dissipated from a resistively heated tip [23] into block copolymers through a nanometric tip-sample contact. This technique acquires images with sub-10 nm resolution and a high surface sensitivity. The measured difference in dissipated energy between the *polystyrene* and the *poly(methyl methacrylate)* is in the range of 20 %, which is close to the difference that can be expected based on the heat conductivity values of the bulk material [24,25]. The presented experiments are executed with the same tool and the same tips as the experiments presented in *chapter 3.* Besides the excellent resolution, the technique allows us to

thermal images at a rate of approximately 5 $^{ms}/_{pixel}$ without the need to conduct the experiment in ultra-high vacuum. We use self-assembled block copolymer films of different pitches and orientations relative to the substrate to demonstrate the excellent resolution of this technique. The material's controlled nanoscale feature sizes provide a good metrology standard for testing the resolution of such imaging method. Studying the thermal properties of block copolymers with high resolution and high contrast requires both a good measurement sensitivity and a large signal-to-noise ratio because *PMMA* and *PS* domains are connected to each other by covalent bonds.

5.2 Experimental

5.1.1 Brush layer deposition

The interface free energy between the substrate and the block copolymer is controlled by a thin layer of *polystyrene-random-poly(methyl methacrylate)* copolymer (*PS-r-PMMA*) to promote vertically oriented lamellae in the block copolymers, and a *hydroxyl-terminated polystyrene* polymer (*PS-OH*) to promote horizontal lamellae. The materials we have used in this work are a *PS-r-PMMA* with a molecular weight $M_{R60} = 7.9\ ^{kg}/_{mol}$ (58 *wt% PS* and 42 *wt% PMMA*; *PDI = 1.85*) and *PS-OH* with a molecular weight $M_{PS\text{-}OH} = 14.5\ ^{kg}/_{mol}$ (*PDI = 1.4*).

Both materials are dissolved in *PGMEA* and a 1.5 wt% solution is spin-coated at 5000 rpm for 30 s. The grafting is promoted through a 5 min annealing step at 230 ºC. Non-grafted macromolecules are subsequently removed in a *PGMEA* rinsing.

5.1.2 Brush layer patterning

The patterning of the *PS-r-PMMA* thin film in elongated rectangular areas of 500 nm x 5 µm has been realized by AFM mechanical (m-AFM) at a tip contact force of approximately 1 µN as described in *chapter 4*. The nominal spring constant of the cantilever is 42 $^{N}/_{m}$.

5.1.3 Block copolymer deposition

In the experiments presented in this paper we work with three different lamellar *PS-b-PMMA* block copolymers characterized by three different relative and absolute chain lengths. The material with a molecular weight $M_{L37}=79\ ^{kg}/_{mol}$ is symmetric (50 wt% *PMMA*; 50 wt% *PS*) and self-assembles in features with 38 nm pitch. The second material consists of 47 % *PS* and 53 % *PMMA* at an overall molecular weight of $M_{L30}=61.2\ ^{kg}/_{mol}$. Its full-pitch is 30 nm. The third material we use is a 42.3 $^{kg}/_{mol}$ molecular weight *PS-b-PMMA* with 42 % *PS* and 58 % *PMMA* at a *PDI = 1.1* whose full-pitch is 23.4 nm.

5.1.4 Thermal AFM tool

The tool we use is an electrostatically actuated scanning probe microscope with the capability to control the apex temperature via resistive heating. For elevated tip temperatures, the tool can be operated in thermal scanning probe patterning mode (see *chapter 3*). For the thermal scanning probe measurements, the tip heat is reduced and the tool is placed in a vacuum chamber. The pressure inside the measurement chamber is typically around 10^{-3} mbar.

5.1.5 Thermal measurement

The cantilever heater temperature in our measurements is between 150 ºC and 400 ºC as determined using the model developed in ref. [26]. The measurement process at each pixel consists of an approach-retract cycle and takes around 5 ms for each cycle. The pixel size is 1-8 nm both in x- and y-direction on the sample surface. Normally, an image as acquired in the course of our experiments consists of 128 x 128 pixels or 256 x 256 pixels per image. Typical imaging times are below 6 min per image.

5.3 Results

5.3.1 Heating and bending the cantilever

Two-legged cantilevers have originally been designed for the use in nano-scale high-speed data storage systems [7,25,26]. In this work we have used three-legged cantilevers that have been developed for the use in thermal scanning probe lithography (t-SPL) [27–29] (see *figure 5.1*). The cantilever consists of high-doped legs represented by resistances $R_{L,1}$, $R_{L,2}$ and $R_{L,3}$ in the equivalent circuit in *figure 5.1.* The source of electric current in the cantilever is the applied bias voltage V_B. The cantilever heating is caused by dissipation of electrical energy in a low-doped region in the close vicinity of the tip apex, referred to as *heater*, and represented by R_H in the equivalent circuit. The voltage drop over the lever legs can be determined using the voltmeter V_L, and the heater current I_H is determined by the amp meter I_H. For the measurement of the thermal conductivity of surfaces, we predominantly use the heater circuit, which is marked by the dotted line in *figure 5.1*. A read sensor, denoted R_R, is used to control the cantilever-surface distance. While the nominal doping concentration both of the *heater* and the *reader* is 3.3 x 10^{17} cm^{-3}, the rest of the cantilever is doped with a nominal concentration of 2.2 x 10^{20} cm^{-3} of phosphorous ions. The capability of predicting the heater temperature as a function of the dissipated electrical power is an essential prerequisite both for thermal scanning probe patterning (*see chapter* 3) and the measurement of thermal properties of materials. For temperatures of up to 1200 ºC, the *heater* represents the principal source of electrical resistance in the legs. For this reason, the resistances $R_{L,1}$, $R_{L,2}$ and $R_{L,3}$ are usually

neglected in the course of our analysis. Reference [26] provides an excellent model for the Joule heating of the cantilever, that has been used in this work to calibrate the cantilever and to estimate the heater temperature as a function of the dissipated electrical power in the heater (defined as heater current I_H multiplied by voltage drop V_L over the cantilever).

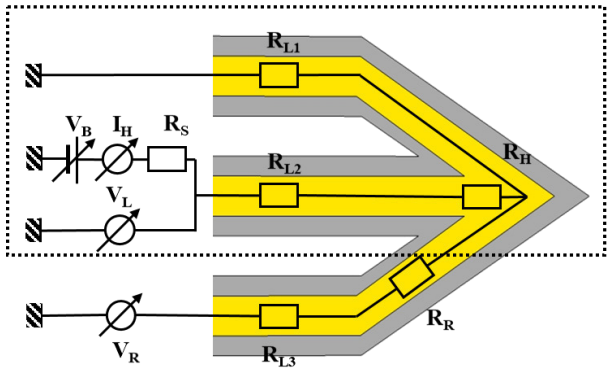

Figure 5.1: Sketch of electrical circuit of the cantilever. In this work, we mainly work with the heater circuit indicated by the dotted box. The bias voltage V_B induces current in the cantilever. The apex is heated by the resistive heating of current flowing through the low-doped region referred to as R_H. V_L is a voltmeter to determine the voltage drop over the cantilever legs and the amp meter I_H determines, how much current is induced into the heater circuit.

The apex is brought into contact with the surface by applying a voltage V_F between the cantilever and the substrate. This creates an attractive force which can be modelled by a capacitor-spring model [11] (see *figure 5.2 a)*). Hence, applying a voltage V_F bends the cantilever down towards the substrate until it comes into contact. The tool registers that the tip has come into contact with the sample, because the tip temperature decreases, which leads to a change in R_H. The voltage V_F is subsequently released and the tip snaps out. Then, the motors move the tip to the next pixel and the procedure is repeated. The sketches in *figure 5.2* help to understand the two operating modes of the unbent cantilever ($V_F = 0$) with a hot apex ($V_B = 0$; at temperature T_1) (*figure 5.2 a)*) and the bent cantilever ($V_F > 0$) at the same bias voltage V_B, but at a slightly lower temperature T_2 (*figure 5.2 b)*). Due to the micrometer sized cantilevers, thermal response times of the Joule heated apex are in the range of micro-seconds. The voltage bias V_B is at a constant level $V_B > 0$ throughout the measurement of an entire image.

5.3.2 Quantification of the heat transfer into a sample

The heater resistance is a function that depends exclusively on the temperature. For this reason, a calibration (see ref. [26]) is capable of correlating the heater temperature with the voltage bias V_B. This calibration is done when the tip is not in contact with the surface

and therefore allows us to set a determined voltage bias V_B that is constant for the entire measurement. In case of the example depicted in *figure 5.2,* the tip temperature T_1 resulting from the applied bias potential V_B is 282.1 °C.

The electrical power P dissipated in the *heater* is quantified by the product of heater current I_H and lever voltage V_L, which both can be read out in the measurement set-up. The $I_H(V_L)$-curve of the heater circuit is depicted in *figure 5.2 c).* Here, the blue point ($I_{H,A}$ / $V_{L,A}$) describes the working point of the cantilever in equilibrium in air. The red line is an accumulation of measurement points as taken during the measurement of an arbitrary block copolymer surface (e.g. corresponding to a state when the tip is in contact with the surface). Once the tip gets into contact with the surface, the tip temperature decreases from T_1 to T_2 with $T_1 > T_2$. This temperature decrease leads to an increase in the heater resistivity and changes both $I_{H,C}$ and $V_{L,C}$ (see *figure 5.2 c), zoom*). The new heater resistance (when the system is in contact with the substrate) can easily be calculated with the help of the new values of $I_{H,C}$ and $V_{L,C}$ by using Ohm's law. The new heater resistance can be correlated with the new tip temperature T_2 due to the initial calibration.

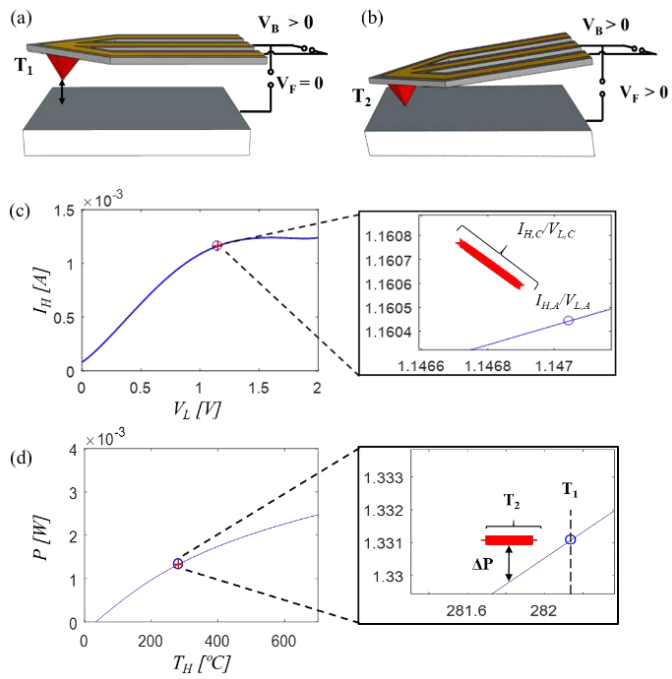

Figure 5.2: Measuring principle and temperature calibration. a): Scheme of cantilever with heated tip ($V_B > 0$, leading to tip temperature T_1) in unbent state ($V_F = 0$), b): Scheme of cantilever in contact with the sample ($V_F > 0$; $V_B > 0$ is the same as in panel a), and the tip temperature is reduced to T_2 due to the tip-sample contact), (c): I-V curve of heater circuit in air (blue curve) and with measuring points (red).

In *figure 5.2.d)* we present the power P dissipated in the heater as a function of the tip temperature. Again, the blue point is the working point of the cantilever in air, not in contact, and the red points represent the different measurement points during the measurement of an arbitrary image. The latter are not located on the initial *P(T)*-curve as measured during contact. This is because, as soon as the tip gets into contact with the surface, electrical power is not only dissipated in the heater, but a part of it is also dissipated into the sample. Because of that, the same amount of dissipated electrical power in the heater now yields a lower tip temperature. We define the power dissipated into the sample ΔP as difference between the dissipated power at each measurement point and the power that would be necessary to heat the tip to this determined temperature T_2, (typically $\Delta T = T_1 - T_2$ is in the range of some tenths of a degree Celsius) if the tip were in contact with the sample. The magnitude of ΔP is in the range of 1 µW. This expression is graphically equivalent to the distance between the respective measurement point and the blue curve in y-direction, as depicted in *figure 5.2 d).*

In general terms, the temperature difference ΔT at each point is directly proportional to the power dissipation ΔP. Here, a higher value for ΔP is associated to a higher thermal conductivity of the probed material.

The following paragraph is to clarify why the measurement of the dissipated power into the sample surface allows us to draw conclusions about the thermal conductivity of the probed material. The thermal resistance R_{th} $[^K/_W]$ of the measured body is defined as the temperature difference $\Delta T_{T\text{-}S}$ between the tip (here equals heater temperature T_H) and the sample (here: room temperature *RT*) divided by the dissipated power ΔP:

$$\frac{\Delta T_{T-S}}{\Delta P} = R_{th}\ \left[\frac{K}{W}\right] \qquad (5.1)$$

An alternative definition of the thermal (spreading) resistance for a sphere into a semi-infinite bulk is

$$R_{th}\ \left[\frac{K}{W}\right] = \frac{1}{4 * k\ \left[\frac{W}{m*K}\right] * a\ [m]} \qquad (5.2)$$

with k being the thermal conductivity of the material and a being the contact radius. By plugging *formula 5.2* into *formula 5.1,* we find that

$$\Delta P = 4 * k * a * \Delta T_{T-S} \qquad (5.3)$$

This expression tells us that for constant $\Delta T_{T\text{-}S}$ the power dissipated ΔP into the sample is linearly proportional to the thermal conductivity k of the probed material. This assumption is reasonable as long as the detected changes in tip temperature are not significant. In the presented measurements, the detected changes in tip temperatures are

in the range of few tenths of a degree Celsius, which is very little compared to the temperature difference between tip and sample, that is in the range of a few hundred degrees Celsius.

5.3.3 Measuring the heat transfer on different surfaces

To take an image as depicted in *figure 5.3 a)*, we scan the surface and detect both the temperature difference $^{\Delta T}/_{T}$ and the dissipated energy ΔP as a direct result thereof for each pixel according to the procedure described before. The image depicted in *figure 5.3 a)* represents a $^{\Delta T}/_{T}$ -map for a lamellar *PS-b-PMMA* block copolymer with a full-pitch of 38 nm self-assembled in vertical lamellae.

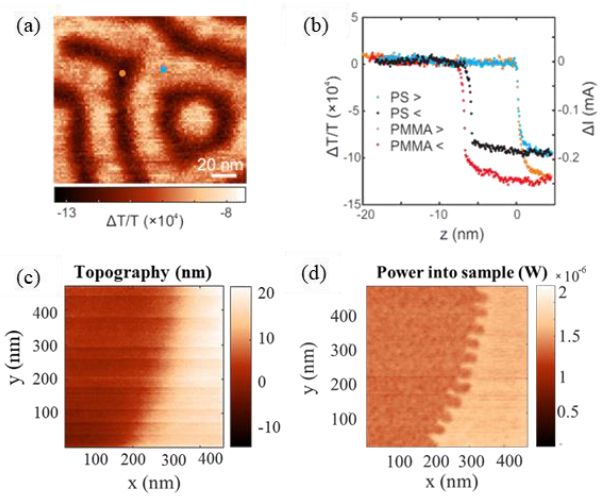

Figure 5.3: Measurement of block copolymers. a): high resolution thermal image of 38 nm pitch PS-b-PMMA block copolymer, b): selected contact curves of image in panel a) for the two different materials, c): topography extracted from snap-in voltages at each measuring point, d): thermal image of the image shown in c).

Let us now have a look at the approach / retract curves detected at each measuring point. In *figure 5.3 b)*, z corresponds to the cantilever deflection that can be controlled by means of the applied substrate voltage V_F. The measured temperature difference $^{\Delta T}/_{T}$ is equal to zero as long as the cantilever is not in contact with the surface. When the cantilever is close to the surface, the attractive capacitive force outweighs the restoring spring force and the cantilever snaps in. The cantilever z-position, at which the snap-in is detected, e.g. position at the moment when the temperature drop is measured, is defined as $z = 0$. The heat transfer from the apex to the surface consequently leads to a temperature drop. Once the snap-in has been detected, the cantilever-bending substrate voltage V_F is

reduced. The snap-out of the cantilever is accompanied by the return to the equilibrium condition of the heater temperature, e.g. $\Delta T/T = 0$. The difference Δz between the snap-in and the snap-out (in this case also referred to as adhesion) represents a measure for the adhesion of the hot tip to the surface and contains qualitative information about the contact area during the measurement. A larger adhesion indicates a larger contact radius of the tip. Nevertheless, Δz is also influenced by the material-dependent contact physics of the tip, which is, for example, expressed in the different Δz values for *PS* and *PMMA*.

The measurement cycle with the approach curve in orange and retract curve in red represents a typical measurement for the *PMMA* domain. Here, the larger $\Delta T/T$ indicates a larger temperature drop. Although the thermal conductivity of *PS* and *PMMA* is a function of the material temperature [30], the thermal conductivity of *PMMA* is at any temperature larger than the one of *PS*. Therefore, there is evidence that areas with lower temperature drops correspond to an area characterized by a lower thermal conductivity, which is *PS* in our measurement. The detected temperature difference of the tip is in the range of $\Delta T/T = 10^{-3}$. A better thermal conductivity of *PMMA* (0.19 $^{W}/_{mK}$) as compared to *PS* (0.14 $^{W}/_{mK}$) is confirmed by results presented in literature [24,25].

An additional information that we can extract form the measurement of the snap-in position as a function of z is the topography of the probed surface. The corresponding topography image is depicted in *figure 5.3 c).* The corresponding thermal image of the same frame is depicted in *figure 5.3 d)* and demonstrates the capability of this method to provide high-resolution images without being influenced by the sample topography. While it is impossible to distinguish the two materials in the topography image, a clear material contrast becomes visible in the thermal image. The thermal image is taken on a sample with a 38 nm full-pitch block copolymer self-assembled in horizontal lamellae. This system can only self-assemble in films with a thickness of an integer multiple of its half-pitch $n\ (0.5\ L_0)$ forming holes or islands with $(n - 1)\ (0.5\ L_0)$ or $(n + 1)\ (0.5\ L_0)$, respectively. To carry out this transition, the material assembles in horizontal lamellae due to their capability of forming structures of arbitrary height [31]. The fringed interface is actually a situation similar to the one described in *chapter 4*, where a narrow area of vertically oriented block copolymers is assembled between two horizontally oriented grains divided by a 90º twist grain boundary. An interesting property of these height steps is that different materials are located at the block copolymer-air interface in each one of the areas. From the topography image we can tell that the left part of the image corresponds to a hole recessed by $0.5\ L_0$ with respect to the right part of the image. Based on the thermal image depicted in *figure 5.3. d),* we can state that less power is dissipated in the left part of the sample, which accordingly consists of *PS*, while the right part consists of *PMMA*.

5.3.4 High-resolution thermal measurements on different block copolymers

In *figure 5.4* we present thermal scanning probe measurements of three different self-assembled block copolymer thin films in fingerprint vertical lamellae. As the materials are defined by different molecular weights, they self-assemble in structures characterized by three different pitches [32]. The structures in *figure 5.4 a)-c)* are characterized by half-pitches of 11.7 nm, 15 nm and 19 nm, respectively. The fact that the features are so clearly resolved demonstrates the excellent lateral resolution of the technique. In the examples of *figure 5.4*, the pixel size of the images is 2 nm x 2 nm.

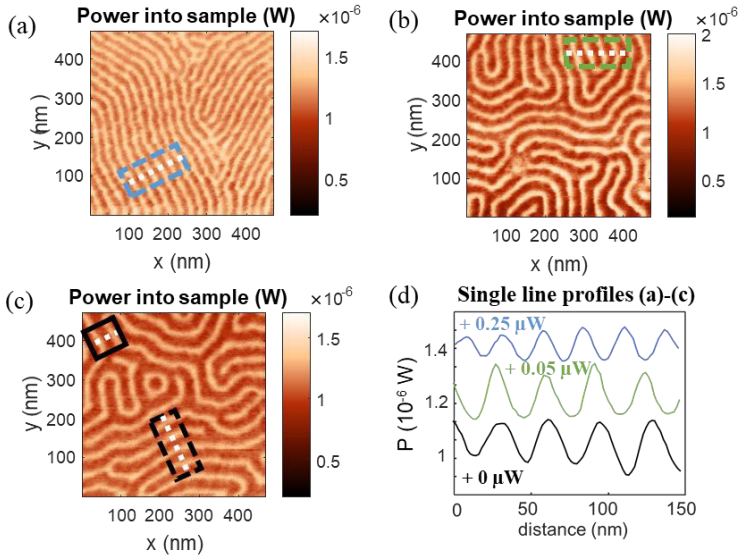

Figure 5.4: <u>High-resolution imaging.</u> a): Thermal image of 23.4 nm pitch PS-b-PMMA block copolymer, b): Thermal image of 30 nm PS-b-PMMA pitch block copolymer, c): Thermal image of 38 nm PS-b-PMMA pitch block copolymer, d): Comparing the dissipated energy for block copolymers with three different pitches a)-c) averaged over the lines indicated by the boxes in the respective image. Added off-sets are 0.05 µW for the green curve and 0.25 µW for the blue curve.

Figure 5.4 d) represents the average of all line scans in the boxes drawn in colored dashed lines. The color of the curve matches the color of the box in the thermal image. Here, it is important to note that the absolute values of the transmitted power may undergo slight changes from one measurement to the other. A reason for this effect may be the attachment and subsequent release of single polymer chains leading to changes in the contact radius. For this reason, we have added an offset to the curves of images of *figure 5.4 (a)* and *(b)*. The y-axis in *figure 5.4 d)* can therefore only be used to identify relative changes in dissipated power between the two materials. We observe that the amplitude of the curve (e.g. the difference in dissipated power ΔP between *PS* and *PMMA*) is nearly

the same for 30 nm pitch and 38 nm pitch polymer (0.150 μW an 0.135 μW, respectively) and decreases notably upon imaging the 23.4 nm polymer (0.073 μW).

Various reasons may be associated to the declining contrast between the two blocks. The first reason is related to the width of the interphase between the two polymer domains. The block copolymer with 23.4 nm pitch is close to the theoretic lower limit for microphase separation in *PS-b-PMMA* [33,34]. This regime is referred to as weak segregation limit and characterized by large interphase widths between the two domains that may occupy up to half of the domain width [35]. The interphase width is inversely proportional to the repulsive force between the blocks, which is in turn proportional to the molecular weight. The diffuse interphase consists of a mixture of *polystyrene* and *PMMA* and is at the prospect of exhibiting a thermal conductivity between the values for the two pure phases.

On the other hand, the tip radius (or more precisely the contact radius between the tip and the material) represents the ultimate resolution limit of thermal imaging [17]. An estimation based on the resolution of the measurement discussed here, is presented in the *discussion* section. TEM images estimate the tip radii of the samples used in this work in the range of 2.5 - 3.5 nm [12]. Additional information about the tips and their analysis is provided in ref. [36].

A combination of these two effects may lead to the effect of decreasing contrast in thermal conductivity between the two blocks as observed during the measurements. The fact that the amplitude of the 30 nm-pitch material is close to equal to the 38 nm-pitch material indicates that such effects play a negligible role in the measurement of block copolymers with 15 nm feature width and above.

5.4 Discussion

In the following, we present the results of a 3D-COMSOL simulation that has been executed to determine the resolution of the thermal imaging and compare its outcome with our measurements. In *sub-section 5.4.1*, we determine the lateral resolution, while we dedicate the second *sub-section 5.4.2* to the discussion of the sampling depth normal to the sample surface.

5.4.1 Determining the lateral resolution

We determine the resolution of the presented thermal imaging technique by comparing the measured block copolymer profile as measured in the 38 nm full-pitch block copolymer averaged over the box indicated by the black solid line in *figure 5.4 c)* with a model of the block copolymer thermal conductivity.

To construct the block copolymer thermal conductivity profile, let us first model the *PS/PMMA* interface using a formula originally developed by Helfand and Tagami for the strong segregation limit SSL [37]. A χN-factor in the range of 30 justifies the use of formulas developed for the SSL. There, the probability f_{PS} of finding an *PS* monomer along the x-direction, which is defined normal to the interface of *PS* and *PMMA* is given by the formula

$$f_{PS}(x) = \left(1 + exp\left\{-2 * \sqrt{6 * \xi} * {}^{x}/_{b}\right\}\right)^{-1} \qquad (5.4)$$

Accordingly,

$$f_{PMMA}(x) = \left(1 + exp\left\{2 * \sqrt{6 * \xi} * {}^{x}/_{b}\right\}\right)^{-1} \qquad (5.5)$$

is to estimate the probability of finding a *PMMA*-monomer along the x-direction, where $x = 0$ is defined at the position where $f_{PS} = f_{PMMA}$. The two curves associated to the *formulas 5.4* and *5.5* are plotted in *figure 5.5 a).* We used $b = 0.66\ nm$ as average Kuhn segment length [38,39] and $\xi = 0.041$ [34,40]. Other authors have determined the diffuse interface width to be in the range of 5 nm, which is in-line with this result [35,41].

Furthermore, we determine the proportion of *PS* and *PMMA* at the polymer-air interface. Despite of the fact the block copolymer material consists of symmetric block copolymer chains, the fraction of the two materials on the sample surface in *figure 5.4 a)* is not equal. To quantify this effect, we present the histogram depicting the number of pixels as a function of dissipated power for the thermal image in *figure 5.5 b).* The shape of the distribution revealed by the histogram can be fitted to the sum of two Gaussian peaks, each one of the form:

$$G(w, x_c, A) = \sqrt{\frac{2}{\pi}} * \frac{A}{w} * e^{-2*\left({}^{(x-x_c)}/_{w}\right)^2} \qquad (5.6)$$

For more information about this formula, see *chapter 2B.* The result of the Gaussian fitting of the *PS* peak and the *PMMA* peak is summarized in *table 5.1*.

Parameter	PS peak	PMMA peak
w [nm]	0.12	0.11
x_c [nm]	1.05	1.24
A [nm]	93.6	59.3
A [%]	61 %	39 %

Table 5.1: Results of the Gaussian fitting of the histogram in figure 5.5 b) to determine the surface distribution of block copolymers in the 38 nm pitch block copolymer.

According to this analysis, the mode value of power dissipated in the *PS* domain is 1.05 μW. The mode value for power dissipated in the *PMMA* domain is 1.24 μW. The relative difference in energy dissipated in the domains, defined as the difference between the two mode values, therefore accounts for 18 %. The literature predicts a difference in thermal conductivity between the two materials in the range of 35 % [24,25]. The measurement points in the vicinity of the intersection between the two Gaussian peaks, that are not optimally represented by the sum of the two fitted peaks, originate from the *PS/PMMA* interface. The detected difference in thermal conductivity represents a very good result given the fact that we measure a system, in which each macromolecule consists both of *PMMA* and *PS*. This results suggests that heat conductivity along the backbone of the macromolecule plays a subordinate role when compared to the influence of the non-covalently bonded monomers in the close vicinity of each monomer.

One reason for the good spectral resolution of this measurement technique is the large signal-to-noise ratio. We believe that the FWHM of the peaks is a reasonable measure for the noise of our measurements, even though the FWHM is likely to overestimate the noise, because we neglect the contribution of the *PS/PMMA* interface to the peak breadth. The measurement points taken at the interphase yield a thermal conductivity that represents neither one of the pure phases, but are still represented in the histogram and utilized during the evaluation. The relation between the fit parameter w and the peak *FWHM* is given in *formula 2B.8* in *chapter 2B* and yields $n_{PS} = 0.235\ \mu W$ for the *FWHM* of the *PS* peak and $n_{PMMA} = 0.118\ \mu W$ for the *PMMA* peak. For the signal-to-noise ratio of the measurement of a material i we use the formula:

$$SNR_{dB,i} = 10 * log_{10}\left(\frac{x_{c,i}}{n_i}\right) \qquad (5.7)$$

This yields $SNR_{dB,PMMA} = 10.2\ dB$ and $SNR_{dB,PS} = 6.5\ dB$ for their measurement.

Based on the Gaussian fitting we find, furthermore, that 61 % of the sample surface represents *PS* (e.g. domain width on the surface is $w_{PS} = 23.2\ nm$), while only 39 % of the surface is *PMMA* (e.g. domain width on the surface is $w_{PMMA} = 14.8\ nm$). These values are provided by an analysis of the parameter *A*, which indicates the area under the peak. Interestingly, the *PS* polymer covers a larger proportion of the surface area than its volume fraction would suggest. A plausible explanation for this effect may be the slightly lower surface energy of *PS* compared to *PMMA*. The same analysis of the 23.4 nm full-pitch block copolymer in *figure 5.4 a)* yields that a 53.5 % of the sample surface consists of *PS* and a 46.5 % of *PMMA*. This result is in-line with the fact that the material is slightly asymmetric and consists of 58 % *PMMA* and 42 % *PS*.

We model the block copolymer thermal conductivity profile as an oscillation between the *ΔP* values for *PS* and *PMMA* with the interfaces determined in *formulas 5.4* and *5.5* and with the domain widths as determined by the histogram analysis.

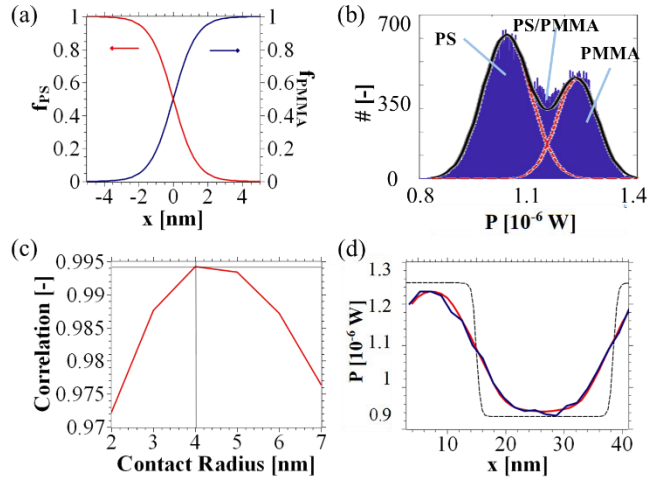

Figure 5.5: Determination of contact radius. a): distribution of PS and PMMA monomers in the close vicinity of the PS/PMMA interface according to Helfand and Tagami, b): histogram of the thermal measurement of a 38 nm full-pitch block copolymer, c): correlation between the measured profile and the modelled profile as a function of the modelled tip-sample contact radius, d): comparison of the measured (blue) and the modelled (red) curve with the grey dotted line representing the distribution in the actual sample.

In the following, we present the result of a COMSOL simulation, where diffusive heat transport through a flat and round contact area was modelled along the profile that we have derived on the previous pages. The sample is represented by a cylinder with a sufficiently large radius (300 nm) and a thickness of 30 nm, with an internal structure equivalent of the block copolymer. The thermal conductivity of the *PS* domain is set to 0.14 $^{W}/_{mK}$ and the one of *PMMA* to 0.19 $^{W}/_{mK}$. The outside surface of the sample cylinder is defined as thermally insulating and the bottom surface is at room temperature. The tip-sample contact area is modelled as circle with radius *a* in the upper part of the sample cylinder. Given that the phonon mean free path in amorphous polymers is in the range of few Ångström, the assumption of purely diffusive heat transport is reasonable. In the following, the correlation coefficient R^2 for different contact radii *a* is compared and the resulting curve is plotted in *figure 5.5 c).* The coefficient of correlation R^2 peaks at a contact radius of 4 nm with $R^2 = 0.994$, indicating that the derived model represents the measured curve excellently. The comparison of the modelled profile (red curve), the measured profile (blue curve) and the actual block copolymer density profile (black

dashed curve) is depicted in *figure 5.5 d)* and demonstrates the excellent agreement between model and measurement. The modelled tip contact radius is in good agreement with the tip radius measured with TEM [12].

In the simulation the block copolymer has been treated as an isotropic material. In the next section we will discuss why this assumption is reasonable despite of the fact that molecular self-assembly influences the orientation of the macromolecules with respect to the sample surface.

5.4.2 Determination of sensing depth

In *figure 5.6 a)/b)* we present a sketch and a thermal image of a block copolymer configuration, where the *PS-b-PMMA* block copolymer with a full-pitch of 30 nm is self-assembled in vertical lamellae next to an area with horizontal lamellae. The fabrication is based on the local removal of the neutral *PS-r-PMMA* brush layer, which promotes vertically aligned lamellae. In those areas where the brush layer is removed, the underlying silicon substrate is revealed. Because the silicon substrate is preferentially wetted by the *PMMA* block, the block copolymer self-assembles in horizontal lamellae [42,43]. This concept is sketched in *figure 5.6 a),* while the thermal image is depicted in *figure 5.6 b)*. For more information about the fabrication of this structure refer to *chapter 4.*

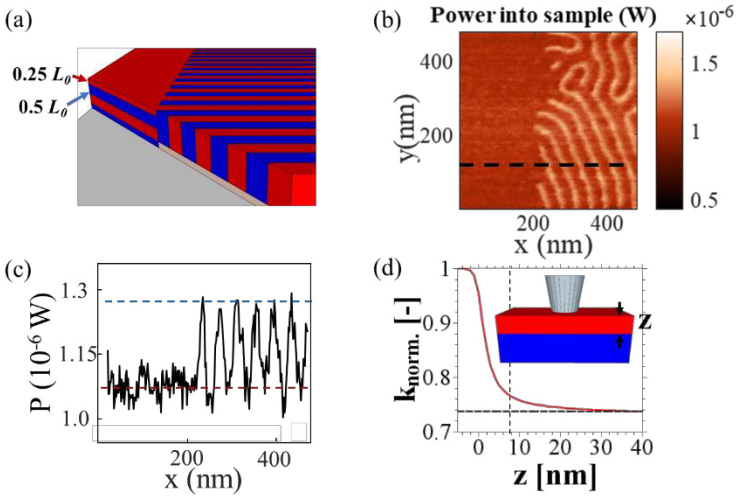

Figure 5.6: Material contrast and determination of sensing depth. a): Scheme of block copolymer morphology in the sample imaged in panel b); b): Image of $^{dT}/_{T}$ of interface between horizontally and vertically aligned block copolymers, c): single line profile along the black dashed line depicted in b), d): model of measured thermal conductivity k_{norm} (normalized to thermal conductivity of PMMA) as a function of the distance z of the PS/PMMA interface from the surface.

Interestingly, we observe that the polystyrene surface has the same thermal conductivity in the area with horizontal lamellae as in the area with vertical lamellae (see single line profile in *figure 5.6 c)*). This observation implies two conclusions. At one hand, the measurement of the thermal conductivity relies on a very surface-sensitive process. As the *polystyrene* top-layer has a thickness of approximately 7.5 nm (*0.25 L_0*), and the absolute dissipated power in this area is exactly the same as in the vertically aligned area, we deduce that the measurement does not gather information from more than 7.5 nm below the surface. On the other hand, it is well-known that the thermal conductivity of polymer chains along their backbone is much larger than the perpendicular to it [44], which is an effect that was expected to find expression in the detection of different thermal conductivities of the *PS* surface in vertically and horizontally aligned areas.

We will first explain, why we do not observe a difference between the horizontally and the vertically oriented domains due to different thermal conductivities along and perpendicular to the chain direction. Let us define the chain stretching σ as the deviation of the block copolymer chain length from its unperturbed state. The unperturbed state is described by the molecule's radius of gyration R_G. On average, one block copolymer molecule is stretched from an extension of twice its radius of gyration R_G to a length of *0.5 L_0* in the course of the self-assembly process. The radius of gyration of an unperturbed polymer chain is a function of the Kuhn segment length b and the polymerization N, and L_0 is a function of χ, N and b [45]. If we now define the relative stretching σ induced to the polymer as the quotient of both terms, the dependence of b cancels out and we can estimate

$$\sigma = \frac{L_0}{4 * R_G} = \frac{1.03 * \chi^{\frac{1}{6}} * N^{\frac{2}{3}}}{4/\sqrt{6} * \sqrt{N}} \approx 1.17 \qquad (5.8)$$

using $N = 600$, $\chi = 0.041$ [34], which represents the present material in a realistic manner. This estimation indicates that a macromolecule similar to the block copolymer used in this experiment exhibits a deformation during the microphase separation in the range of 17 % with respect to its radius of gyration. According to results presented in ref. [44], this deformation leads to a change in thermal conductivity of *PS* of less than 1 %. It is therefore reasonable, that we are not capable of detecting different thermal conductivities in two differently self-assembled block copolymer domains consisting of the same material.

We now refer to the curve depicted in *figure 5.6 d)* to explain, why we do not detect the influence of the *PMMA* layer 7.5 nm below the surface in the horizontally aligned layer. The depicted curve represents a simulation based on a 3D-COMSOL model of the measured thermal conductivity on a *PS* surface with a *PS/PMMA* at a distance z below

the surface for a tip contact radius of 4 nm. The y-axis is normalized to the expected result for a *PS* top layer with zero thickness, which is equivalent to a measurement directly on a *PMMA* surface. For very large distances between the surface and the interface, e.g. for a thick upper *PS* film, the curve asymptotically approaches a value of 0.737, which corresponds to the thermal conductivity of *PS* normalized to the value of *PMMA*. The vertical dashed line indicates that the result for a measurement with $z = 7.5\ nm$ below the surface as measured with a tip with a contact radius of 4 nm is expected to differ merely 4 % from the result on a pure *PS* film. This is below the noise level in *figure 5.6 c).*

5.5 Conclusions

We measured the thermal power dissipated into *PS-PMMA* block copolymer samples with sub-10 nm resolution using electrostatic actuation of heated silicon levers in vacuum. Owing to the small thermal time constant of 6 µs and the fast actuation scheme, an entire approach cycle is monitored within ~5 ms. The thermal signal is consistent with the difference in thermal conductivity between *PS* and *PMMA* based on the literature values for bulk *PS* and *PMMA*. We are capable of obtaining images with an excellent lateral resolution due to the very sharp resistively heated AFM tips. Based on a comparison with a finite element model, we determine a tip-sample contact radius of 4 nm. Knowing the contact radius, we infer that more than 90 % of the signal originates from a depth of less than 10 nm, highlighting the surface sensitivity of the method. The good signal-to-noise ratio gives rise to the expectation that the technique is also capable of distinguishing between (polymeric) materials with even smaller differences in thermal conductivity and/or more different polymers in the same sample. Being able to measure dissipated power and contact radius simultaneously may allow us to obtain reliable absolute measurements of the thermal conductivities of polymers close to the surface and at sub-10 nm lateral resolution. It could moreover represent an interesting technique to study the thermal properties self-assembly mechanism of block copolymers and other polymeric materials below and around their glass transition temperature.

5.6 References

[1] Schelling P K, Shi L and Goodson K E 2005 Managing heat for electronics *Mater. Today* **8** 30–5

[2] Pop E 2010 Energy Dissipation and Transport in Nanoscale Devices **2** 147–69

[3] Menges F, Riel H, Stemmer A and Gotsmann B 2012 Quantitative Thermometry of Nanoscale Hot Spots *Nano Lett.* **12** 596–601

[4] Menges F, Mensch P, Schmid H, Riel H, Stemmer A and Gotsmann B 2016

temperature mapping of operating nanoscale devices by scanning probe thermometry *Nat. Commun.* **7** 1–6

[5] Soudi A, Dawson R D and Gu Y 2011 Characteristics in Current-Carrying GaN Scanning Thermal Microscopy and *ACS Nano* **5** 255–62

[6] Gomès S, Assy A and Chapuis P-O 2015 Scanning thermal microscopy: A review *Phys. Status Solidi A* **212** 477–94

[7] Majumdar A, Lai J, Chandrachood M, Nakabeppu O, Wu Y and Shi Z 1995 Thermal imaging by atomic force microscopy using thermocouple cantilever probes *Rev. Sci. Instrum.* **66** 3584–92

[8] Edinger K, Gotszalk T and Rangelow I W 2001 Novel high resolution scanning thermal probe *J. Vac. Sci. Technol. B Microelectron. Nanom. Struct.* **19** 2856–60

[9] Aigouy L, Tessier G, Mortier M and Charlot B 2005 Scanning thermal imaging of microelectronic circuits with a fluorescent nanoprobe *Appl. Phys. Lett.* **87** 1–3

[10] Nakabeppu O, Chandrachood M, Wu Y, Lai J and Majumdar A 1995 Scanning thermal imaging microscopy using composite cantilever probes *Appl. Phys. Lett.* **694** 694–6

[11] Vettiger P, Cross G, Despont M, Drechsler U, Durig U, Gotsmann B, Haberle W, Lantz M, Rothuizen H E, Stutz R and Binnig G K 2002 The “millipede” - nanotechnology entering data storage *IEEE Trans. Nanotechnol.* **1** 39–55

[12] Ryu Cho Y K, Rawlings C D, Wolf H, Spieser M, Bisig S, Reidt S, Sousa M, Khanal S R, Jacobs T D B and Knoll A W 2017 Sub-10 Nanometer Feature Size in Silicon Using Thermal Scanning Probe Lithography *ACS Nano* **11** 11890–7

[13] Fischinger T J, Laher M and Hild S 2014 An evaluation of local thermal analysis of polymers on the sub-micrometer scale using heated scanning probe microscopy cantilevers *J. Phys. Chem. B* **118** 5570–6

[14] Nonnenmacher M and Wickramasinghe H K 1992 Scanning probe microscopy of thermal conductivity and subsurface properties *Appl. Phys. Lett.* **61** 168–70

[15] Menges F and Stemmer A 2013 Thermal Transport into Graphene through Nanoscopic Contacts **205901** 1–5

[16] Hinz M, Marti O, Gotsmann B, Lantz M A and Dürig U 2008 High resolution vacuum scanning thermal microscopy of HfO2 and SiO2 *Appl. Phys. Lett.* **92** 1–3

[17] Kim K, Jeong W, Lee W, Reddy P and Al K I M E T 2012 Ultra-High Vacuum Scanning Thermal Microscopy for Nanometer Resolution Quantitative Thermometry *ACS Nano* **6** 4248–57

[18] Fryer D S, Nealey P F and Pablo J J De 2000 Thermal Probe Measurements of the Glass Transition Temperature for Ultrathin Polymer Films as a Function of Thickness *Macromolecules* **33** 6439–47

[19] Kim G H, Lee D, Shanker A, Shao L, Kwon M S, Gidley D, Kim J and Pipe K

P 2015 High thermal conductivity in amorphous polymer blends by engineered interchain interactions *Nat. Mater.* **14** 295–300

[20] Shen S, Henry A, Tong J, Zheng R and Chen G 2010 Polyethylene nanofibres with very high thermal conductivities *Nat. Nanotechnol.* **5** 251–5

[21] Luo T and Chen G 2013 Nanoscale heat transfer – from computation to experiment *Phys. Chem. Chem. Phys.* **15** 3389–412

[22] Kim K, Song B, Fernández-hurtado V, Lee W, Jeong W, Cui L, Thompson D, Feist J, Reid M T H, García-vidal F J, Cuevas J C, Meyhofer E and Reddy P 2015 Radiative heat transfer in the extreme near field *Nature* **528** 387–91

[23] Drechsler U, Bürer N, Despont M, Dürig U, Gotsmann B, Robin F and Vettiger P 2003 Cantilevers with nano-heaters for thermomechanical storage application *Microelectron. Eng.* **67**–**68** 397–404

[24] Mahmoodi M, Hoon Lee Y, Mohamad A and Park S S 2014 Effect of Flow Induced Alignment on the Thermal Conductivity of Injection Molded Carbon Nanotube-Filled Polystyrene Nanocomposites *Polym. Eng. Sci.* **55** 753–62

[25] Assael M J, Botsios S, Gialou K and Metaxa I N 2005 Thermal conductivity of polymethyl methacrylate (PMMA) and borosilicate crown glass BK7 *Int. J. Thermophys.* **26** 1595–605

[26] Spieser M, Rawlings C, Lörtscher E, Duerig U and Knoll A W 2017 Comprehensive modeling of Joule heated cantilever probes *J. Appl. Phys.* **121** 174503-1–12

[27] Knoll A W, Pires D, Coulembier O, Dubois P, Hedrick J L, Frommer J and Duerig U 2010 Probe-based 3-D nanolithography using self-amplified depolymerization polymers *Adv. Mater.* **22** 3361–5

[28] Pires D, Hedrick J L, Silva A De, Frommer J, Gotsman B, Wolf H, Despont M, Duerig U and Knoll A W 2010 Nanoscale Three-Dimensional Patterning of Molecular Resists by Scanning Probes *Science·* **328** 732–5

[29] Wolf H, Rawlings C, Mensch P, Hedrick J L, Coady D J, Duerig U and Knoll A W 2015 Sub-20 nm silicon patterning and metal lift-off using thermal scanning probe lithography *J. Vac. Sci. Technol. B* **33** 02B102-1-6

[30] Santos W N, Sousa J A De and Jr R G 2013 Thermal conductivity behaviour of polymers around glass transition and crystalline melting temperatures *Polym. Test.* **32** 987–94

[31] Carvalho B L and Thomas E L 1994 Morphology of Steps in Terraced Block Copolymer Films *Phys. Rev. Lett.* **73** 3321–4

[32] Bates F S and Fredrickson G H 1999 Block Copolymers—Designer Soft Materials *Phys. Today* **52** 32–8

[33] Leibler L 1980 Theory of microphase separation in block copolymers *Macromolecules* **13** 1602–17

[34] Russell T P, Hjelm R P and Seeger P A 1990 Temperature Dependence of the Interaction Parameter of Polystyrene and Poly (methyl methacrylate) *Macromolecules* **23** 890–3

[35] Wan L, Ruiz R, Gao H, Patel K C and Albrecht T R 2015 The Limits of Lamellae-Forming PS-b-PMMA Block Copolymers for Lithography *ASC Nano* **9** 7506–14

[36] Jacobs T D B, Wabiszewski G E, Goodman A J and Carpick R W 2016 Characterizing nanoscale scanning probes using electron microscopy: A novel fixture and a practical guide *Rev. Sci. Instrum.* **87** 013703-1–10

[37] Helfand E and Tagami Y 1971 Theory of the interface between immiscible polymers *Polym. Lett.* **9** 741–6

[38] Sparnacci K, Antonioli D, Gianotti V, Laus M, Ferrarese Lupi F, Giammaria T J, Seguini G and Perego M 2015 Ultrathin Random Copolymer-Grafted Layers for Block Copolymer Self-Assembly *ACS Appl. Mater. Interfaces* **7** 10944–51

[39] Ballard D G H, Wignall G D and Schelten J 1973 Measurement of molecular dimensions of polystyrene chains in the bulk polymer by low angle neutron diffraction *Eur. Polym. J.* **9** 965–9

[40] Bates F S and Fredrickson G H 1990 Block Copolymer Thermodynamics: Theory and Experiment *Annu. Rev. Phys. Chem.* **41** 525–57

[41] Sunday D F, Ashley E, Wan L, Patel K C, Ruiz R and Kline R J 2015 Template-polymer commensurability and directed self-assembly block copolymer lithography *J. Polym. Sci. Part B Polym. Phys.* **53** 595–603

[42] Carriere C J and Sammler R L 2000 Temperature dependence of the interfacial tension of PS/PMMA , PS/PE, and PMMA/PE blends *Rheol. Acta* **39** 476–82

[43] Owens D K and Wendt R C 1969 Estimation of the Surface Free Energy of Polymers *J. Appl. Polym. Sci.* **13** 1741–7

[44] Washo B D and Hansen D 1969 Heat conduction in linear amorphous high polymers: Orientation anisotropy *J. Appl. Phys.* **40** 2423–7

[45] Hashimoto T, Shibayama M and Kawai H 1980 Domain-Boundary Structure of Styrene-isoprene Block Copolymer Films Cast from Solution. 4. Molecular-Weight Dependence of Lamellar Microdomains *Macromolecules* **13** 1237–47

General conclusions

This PhD thesis contributes to the field of guiding pattern fabrication for the directed self-assembly of block copolymers with a particular focus on the exploration of guiding patterns with high resolution and high accuracy. These structures are at the prospect of playing a key role for the successful directed self-assembly of new high-χ block copolymers, which are particularly interesting for the fabrication of future nanoelectronic devices. The most important achievements of this thesis are summarized in the following paragraphs.

A substantial part of this thesis is dedicated to the development and testing of different guiding pattern fabrication techniques, where we have pushed the respective techniques towards their resolution limit.

In particular, we have successfully directed the self-assembly of a 11.7 nm half pitch *PS-b-PMMA* block copolymer making use of **five different lithography techniques for the fabrication of guiding patterns**, namely *(i)* EUV-IL *(ii)* e-beam lithography (both used for graphoepitaxy), *(iii)* thermal scanning probe lithography (chemoepitaxy), *(iv)* mechanical AFM lithography and *(v)* e-beam direct writing (both used for grain-boundary-induced alignment).

The self-assembly mechanism of block copolymers in **topographical guiding patterns** has been studied using parallel EUV-IL. Herein, the behavior of block copolymers under **confinement** has been studied with **nanometer precision**, and a **free energy model** has been developed to describe the defective self-assembly state based on the experimental findings. The developed free-energy model accurately defines the process window for the directed self-assembly in topographical guiding patterns.

The developed free energy model has been modified to describe the process window for the directed self-assembly of block copolymers in **topographical guiding patterns with sub-10 nm feature width** defined by e-beam lithography. This system has been used to determine the self-assembly morphology of block copolymers in topographical guiding patterns with feature sizes close to their half-pitch and to formulate a general design rule for such guiding patterns.

A thermal scanning probe based technique for the fabrication of **chemical guiding patterns with 10 nm resolution** has been developed. The recent commercialization of thermal scanning probe lithography as nanofabrication technique converts the use of thermal scanning probe lithography for the directed self-assembly of block copolymer lithography into a technologically particularly interesting combination.

Grain-boundary-induced alignment is presented as an **alternative alignment technique** capable of controlling block copolymers on length scales around their inherent correlation length. Its working principle is explained and experimentally demonstrated using mechanical AFM surface modification and e-beam direct writing. The technique is especially interesting for the use in fast prototyping processes and has been entirely developed in the facilities of the IMB-CNM.

A complementary, but yet important part of this thesis is related to the development of measurement techniques capable of providing improved insight into the self-assembly morphology and the properties of block copolymers.

A thermal scanning probe based imaging technique to study the **thermal conductivity** of block copolymers with a **sub-10 nm resolution** has been developed. The technique is very surface sensitive and allows it to differentiate clearly between *PS* and *PMMA* despite of their very similar thermal conductivities.

GISAXS has been used to study the self-assembly of block copolymers in topographical guiding patterns and we demonstrate to be capable of determining the **block copolymer pitch** under confinement **with sub-nm precision**. GISAXS has moreover been used to estimate the **correlation length** of block copolymers in free surface.

Annex 1:

Pattern transfer using block copolymer templates

Abstract:

This *annex* summarizes the results obtained during pattern transfer experiments with *PS-b-PMMA* block copolymers with critical feature sizes between 10 nm and 15 nm. Concrete etch recipes are presented that enable the pattern transfer of nanometer-sized features employing a pseudo-Bosch process with SF_6 and C_4F_8 as simultaneously injected reaction gases yielding etch depths of few tens of nanometers. Herein, we have used both *PS* and Al_2O_3-infiltrated *PMMA* as etch masks. Lateral etching and mask erosion have been identified as critical parameters for the successful pattern transfer of block copolymers features with an aspect ratio AR > 2. When using *PS* etch masks, we moreover identify the thickness of the neutral brush layer as critical parameter for the successful fabrication of the mask. We conclude that the infiltration of *PMMA* with Al_2O_3 is an interesting method to increase the process window for the pattern transfer of block copolymers and enhance the maximum achievable etch depth.

Table of contents: Annex 1

A.1 Introduction

To make use of the directed self-assembly of block copolymers for nanofabrication purposes, it is important to develop suitable etch processes to transfer the defined patterns into the underlying substrate. Lamellar block copolymers transferred into silicon represent an interesting alternative for the fabrication of finFETs [1]. Besides the fabrication of the holes for vertical contacting of micro- and nanoelectronic devices, upright standing cylindrical block copolymer structures have been demonstrated to be a good way to fabricate bit patterned media [2]. They may moreover be used as a template for the selective growth of nanowires with precisely defined diameter and spacing [3]. This *annex* represents a compilation of results obtained by transfer processes of block copolymer patterns into silicon.

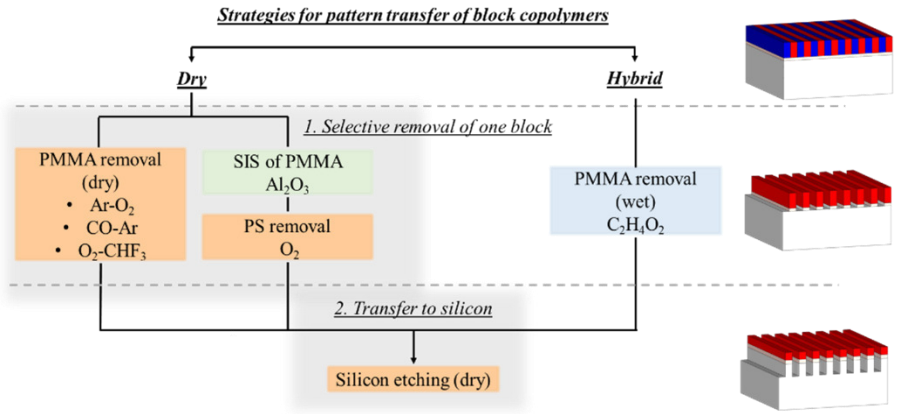

Figure A.1: Overview of pattern transfer strategies. Pattern transfer strategies for block copolymers always consist of at least two process steps including one step to selectively remove one of the blocks and a second one to transfer the structure into the substrate, which is usually silicon. The sketches on the right side show sketches of the status of the respective block copolymer sample.

Pattern transfer processes for block copolymer patterns usually consist of two major steps, namely the selective removal of one of the blocks at one hand and the subsequent substrate etching step on the other hand (see *figure A.1)*. The first step, the selective removal of one block, is necessary to convert the initially continuous block copolymer film into an etch mask consisting of areas that protect the substrate from the following chemical attack, and areas where the substrate is directly exposed to the reactive species. For *PS-b-PMMA*, the most frequently used approach is to remove the chemically less inert *PMMA* block. There are, however, also approaches that enhance the etch resistivity of *PMMA* by a special treatment and in the following remove the *PS* block. The second step then uses the previously created etch mask to transfer the defined pattern into the

substrate. Given the small feature sizes and the small thickness of the initial film (and therefore also of the etch mask), it is critical for both of the steps to have good control over the lateral and vertical etch rate, and to develop processes with a sufficiently large etch selectivity.

In this thesis we have made exclusively use of dry etching steps both for the selective removal of one of the blocks and the subsequent silicon pattern transfer. There are also hybrid approaches, that remove the *PMMA* block of a *PS-b-PMMA* block copolymer *via* wet etching and transfer the patterns into silicon *via* dry etching. An overview of different block copolymer pattern transfer strategies is provided in *figure A.1*. Wet etching therefore represents an alternative for the first step of the pattern transfer process. An infinite [4] etch selectivity is claimed for the rinsing of *PS-b-PMMA* in acetic acid after the exposition of the film by DUV radiation [5]. The UV-sensible *PMMA* layer is degraded [6], while *PS* is not [7]. For moderate UV exposure doses, *PS* undergoes a crosslinking process and therefore even reduces its solubility [8]. At the same time, acetic acid is a solvent for the (both degraded and non-degraded) *PMMA* [9].

In pure dry etching approaches, *PMMA* can be selectively removed using a variety of different process gases. Pure oxygen plasmas [10], *Ar*-O_2-mixtures [11], *CO*-*Ar*-mixtures [12] and also O_2-CHF_3-mixtures [13] are some of the gas mixtures that have been demonstrated to be suitable for this process. The specific underlying mechanisms for the preferential etching of *PMMA* in each of the respective mixtures is beyond the scope of this *annex*. The common denominator of those processes is the use of oxygen, whose radicals drive the etching mechanism. The aromatic side group of polystyrene is chemically much more resistant towards oxygen radicals than the oxygen-containing side groups of *PMMA*. This effect explains the lower etch resistance of *PMMA* compared to *PS*.

The second and technologically more sophisticated selective removal approach seeks to convert one of the blocks into another material. This conversion is realized by the means of an infiltration triggered by an atomic layer deposition (ALD) step. The entire process is referred to as selective infiltration synthesis (SIS) [14–16]. A commonly used precursor for selective infiltration synthesis is *trimethyl aluminum* (*TMA*), which is selectively deposited on top of the *PMMA* domain. The material is converted into aluminum oxide during a water exposure cycle. The quantity of aluminum oxide infiltered into the *PMMA* domain is proportional to the number of repeat cycles of this procedure [17]. The aim of the SIS process is that the infiltrated block (*PMMA* in case of *PS-b-PMMA*) shows a higher etch resistance with respect to the plasma and a higher etch selectivity with respect to the other block. The etch resistance of the *PMMA* domain infiltrated by aluminum

oxide is significantly larger than of the non-infiltrated *PS* and *PMMA* domains. In this approach, the *PS* domain is removed by an aggressive O_2 plasma exposure.

To transfer structures with nanometer lateral dimensions into the underlying (usually silicon) substrate, it is indispensable to apply a patterning process with a precisely controllable and at the same time moderate etch velocity. One alternative to achieve this is the pseudo-Bosch process. Unlike in the common Bosch process used in microfabrication, in the pseudo-Bosch process both reaction gases, C_4F_8 and SF_6, are injected with a constant flow rather than in a pulsed mode [18]. The SF_6 molecules are decomposed in the plasma and represent the source of fluorine ions ultimately responsible to etch the silicon substrate under the formation of SiF_4 as reaction product [19]. The injection of C_4F_8, on the other hand, leads to the polymerization of CF_2 species [20]. This homogenously deposited film of CF_2 chains with different polymerization protects the side walls of the etched features, while it is constantly sputtered away on the bottom of the trenches. The sputtering speed of this process can be controlled by the applied chuck potential, a value that is responsible for the acceleration of charged particles towards the substrate [18]. The forward bias is a sensitive parameter, especially to transfer nanometer-sized features when defined by the polystyrene part of the block copolymer. A large forward bias sputters away not only the polymerized CF_2 layer efficiently, but also damages the polystyrene layer. Processes with very low forward bias, however, lack sufficient etch velocity and may not be capable of efficiently removing the deposited polymer layer on the bottom of the pattern [18].

In the following, we present images of block copolymer patterns transferred into silicon substrates and give an overview of the used etching conditions. Unless the contrary is explicitly stated, all the block copolymer films shown in this *annex* have been spun from a 1.5 wt% solution of the respective block copolymer in *PGMEA* at 2500 rpm, which yields a film thickness of about 25 nm.

A.2 Selective removal of one block

A.2.1 PMMA removal via dry etching

The process conditions that have been applied in the *PMMA* removal step are the following: 200 sccm *Ar*, 10 sccm O_2, 1.33 Pa, 200 W ICP power and 5 W chuck power (see *table A.1*) using an Alcatel AMS 110 deep RIE ICP system. The etch velocity of the *PMMA* domain is about 80 $^{nm}/_{min}$ at a selectivity of around 1:4 with respect to *PS*. The images presented in *figure A.2 a)-d)* are taken after a 30 s etch process.

Source power	Chuck power	Gas flows		Process pressure	Etch time
		O_2	Ar		
200 W	5 W	10 sccm	200 sccm	1.3 Pa	30 s

Table A.1: Process conditions for the PMMA removal in different PS-b-PMMA block copolymers.

The red arrows depicted in the panels *a)* and *b)* in *figure A.2* indicate areas where we detect residual brush layer after the etching step. According to our experience, the etch rate for the brush layer is significantly lower than for the *PMMA* domain. The reason for that may that, the neutral brush layer is a mixture of *PS* and *PMMA* and may therefore resist the *Ar-O2*-etch more efficiently than the pure *PMMA* domain. In *figure A.2 a)* the *PS* fraction in the random copolymer is 70 %, while the *PMMA* fraction is 30 %. In *figure A.2 b)* the used random copolymer consists of 60 % *PS* and 40 % *PMMA*. The relatively high proportion of *PS* in both neutral brush layers used in this work leads to the effect that the process time must be increased notably in order to open the layer entirely. An increase in etching time represents, however, also an increase of the mask wearing. An entirely removed brush layer in the areas of the *PMMA* block is nevertheless a prerequisite to start the etching of the features in the whole sample area at the same time.

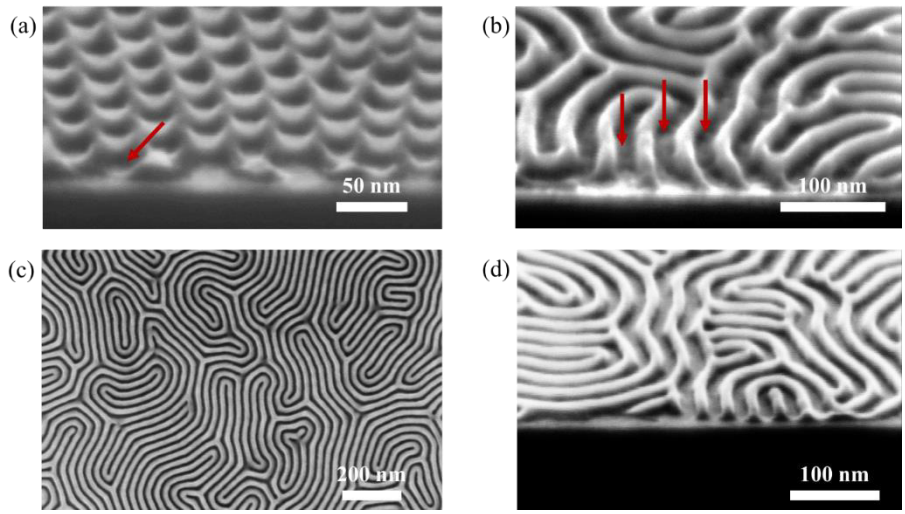

Figure A.2: Residual brush layer after PMMA etching. a) 35 nm full-pitch cylindrical block copolymer with 7 nm neutral brush layer after PMMA removal, b) 38 nm full-pitch lamellar block copolymer with 7 nm neutral brush layer after PMMA removal, c) top-view image of a 30 nm pitch lamellar block copolymer deposited on a thin random copolymer layer after PMMA removal, d) cross-section SEM image of image c).

A convenient solution for this problem is the reduction of the random copolymer thickness. The brush layers of the samples depicted in *figure A.2. a)* and *b)* have been deposited with the conditions referred to as *"thick brush layer"* in *chapter 2A*. This means that the initial film is spun from a 1.5 wt% solution, which leads to an approximately 7 nm thick random copolymer film after rinsing. In *chapter 2A* we have also presented a deposition method referred to as *"thin brush layer"*, where the random copolymer is spun from a 0.25 wt% solution leading to an approximately 3 nm thick film in free surface.

The SEM images depicted in *figure A.2 c)* and *d)* are taken from a sample with a 25 nm lamellar block copolymer deposited on top the said *"thin brush layer"*. The overview image depicted in *figure A.2 c)* demonstrates that the thin brush layer is also capable of providing upright standing block copolymer lamellae. Furthermore, the cross-section image depicted in *figure A.2 d)* demonstrates that the same 30 s lasting *PMMA* removal step is capable of opening the structure down to the silicon substrate. The remaining structure represents merely a network of *PS* domains which precisely represents the desired outcome for this process.

A.3 Pattern transfer to silicon

As suggested in the *introduction*, the implementation of block copolymer lithography in semiconductor manufacturing requires the transfer of patterns to silicon. *Section A.3* of this *annex* aims to present our results of pattern transfer into silicon. More specifically, we present results on the pattern transfer using a *PS* mask in *section A.3.1*, and the results of the pattern transfer after a SIS process in *section A.3.2.* We have applied different pseudo-Bosch processes to the samples discussed in both sections. The silicon etching processes have been done in the same Alcatel AMS 110 deep RIE ICP system as the *PMMA* removal.

A.3.1 Pattern transfer using a PS etch mask

Results of the pattern transfer of a 30 nm pitch lamellar block copolymer are depicted in a top-view SEM image in *figure A.3 a)* and a cross-section SEM image of the same sample in *figure A.3 b).*

We observe in the SEM top-view image depicted in *figure A.3 a)* that the features show a waviness that has not been there after the *PMMA* removal (compare with *figure A.2 c)*). The reason for this waviness is not clear. We have discussed a similar effect in *chapter 2A*

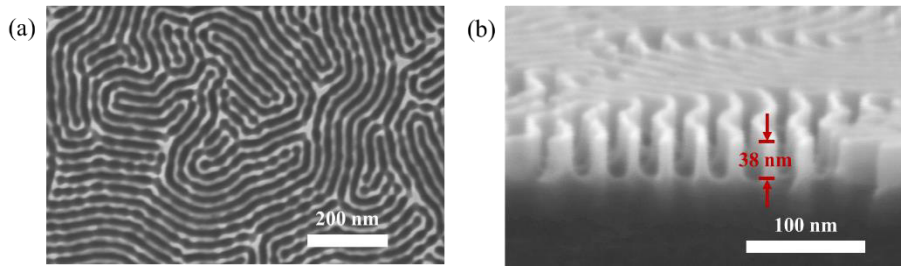

Figure A.3: Overview of the pattern transfer of a 30 nm pitch lamellar block copolymer.

The process parameters of the applied pseudo-Bosch process to etch the silicon are summarized in *table A.2*. The relatively large source power of 1200 W is a normal value for the etching of silicon in ICP processes [21]. The chuck power of 10 W is low, but still larger than for the *PMMA* removal process, where it is 5 W. 10 W has been found to represent the minimum value that is capable of opening the CF_2 polymer layer at the given ratio of SF_6 and C_4F_8. A low chuck power yields a lower vertical and larger horizontal etch rate [22], but also represents an effective way to reduce mask sputtering. On the other hand, the large percentage of SF_6 compared to C_4F_8 yields a relatively fast etching. While the gas composition contains 20 sccm SF_6 and 15 sccm C_4F_8, results presented in literature suggest gas mixtures with a significantly larger C_4F_8 fractions. Gas mixtures of up to 80 sccm C_4F_8 and 15 sccm SF_6 been reported [21]. It is a frequently observed phenomenon in reactive ion etching processes that the same conditions yield different results in different tools. The presented etch conditions are developed for the Alcatel AMS 110 Deep ICP-RIE in the clean room of IMB-CNM and must not necessarily be transferrable to other tools. On the other hand, many different sets of process conditions may lead to similar plasma chemistries and therefore to similar etching results.

Source power	Chuck power	Gas flows		Process pressure	Etch time
		SF_6	C_4F_8		
1200 W	10 W	20 sccm	15 sccm	2 Pa	20 s

Table A.2: Process conditions of pattern transfer using the PS block of a 30 nm full pitch lamellar block copolymer as etch mask.

The presented etching conditions yield a patterning depth of 38 nm. According to the 2016 edition of the IEEE International Roadmap for Devices and Systems, a typical fin heights for the fabrication of finFETs is supposed to be around 42 nm [23]. The difference between the feature height and the height required for fins in high volume manufacturing is below 10 %. Despite of the fact that the block copolymer is symmetric (e.g. in the

pristine film the *PS* domain is as wide as the *PMMA* domain) the feature width is in the range of 11 nm at 30 nm full pitch. The derivation of the feature width from the expected 15 nm is in part caused by a non-zero lateral etch velocity throughout the silicon etching process. The second reason is related to the interphase between the *PS* and the *PMMA* block upon self-assembly. A formula to determine the diffuse interphase between the *PS* and the *PMMA* block has been proposed by Helfand and Tagami [24] and yields that the distance between the position where the film consists of 95 % *PS* and where it consists of 95 % *PMMA* is around 4 nm (see *chapter 5*). The successively changing material composition is leads to a successively changing etch resistance throughout the interphase and represents another reason for the reduction of the feature width.

The result of the pattern transfer of a 23.4 nm full pitch lamellar *PS-b-PMMA* block copolymer is discussed in the following paragraphs. The chosen etching conditions for this process are the same as for the 30 nm full pitch block copolymer discussed before, while the etching time is reduced notably from 20 s to 10-15 s (see *table A.3*).

Source power	Chuck power	Gas flows		Process pressure	Etch time
		SF_6	C_4F_8		
1200 W	10 W	20 sccm	15 sccm	2 Pa	10-15 s

Table A.3: Process conditions of pattern transfer using the PS block of a 23.4 nm full pitch lamellar block copolymer as etch mask.

Representative SEM images of the results of processes using etching times of 10 s, 12 s and 15 s are depicted in *figure A.4 a)-c)*. While the sample depicted in the left image (*figure A.4 a)*) has clearly not yet reached the maximum etch depth (e.g. the residual *PS* mask is very thick in comparison to the etch depth), the sample depicted in the right image is clearly overetched (*figure A.4 c)*). This is expressed by notably thinner features, some of whom even suffer from breakthroughs. Considering the residual mask thicknesses as a function of the etching time (compare *figure A.3 b)* and *figure A.4 a)-c)*) indicates that the etch resistivity of the *PS* mask for the two different block copolymers in question is comparable, hence the resistivity of the *PS* mask is not a function of the molecular weight.

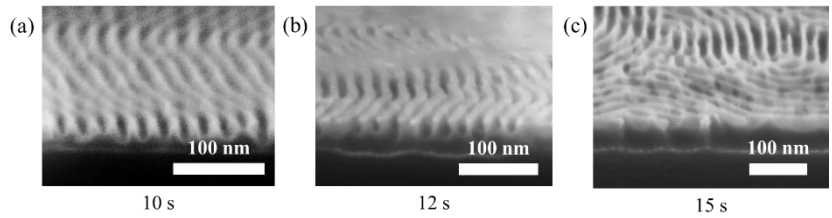

Figure A.4: Evolution of the aspect of the pattern of a 23.4 nm full pitch lamellar PS-b-PMMA block copolymer as a function of the etching time.

Based on our experiments, we conclude that the limit of the pattern transfer depth for the two block copolymers is determined by two different effects. While mask wearing is the dominant effect in the pattern transfer of the 30 nm full pitch block copolymer, the pattern transfer of the 23.4 nm full pitch block copolymer is restricted by the lateral etch velocity. The difficulty of the lateral etch rate in the 23.4 nm block copolymer becomes even more evident, when we take into account that the material consists of merely 43 wt% *PS*. Based on this we can estimate that the width of the *PS* domain in its initial state is as low as 10 nm. In addition to that, this material is relatively close to the order-disorder-transition line in the phase diagram. As a result, the diffuse interphase between the two phases becomes broader and makes the *PS* domain more prone to lateral etching in the *PMMA* removal step.

Cross-section images of transferred structures under minimum tilt angle (e.g. 2º) before and after the removal of the residual etch mask are depicted in *figure A.5*. A sketch on the left side of the SEM images depicts the *PS* domain in red color and silicon in light-grey. The removal of the residual mask is done *via* an oxygen plasma cleaning step at 500 W for about 10 minutes. The treatment is strong enough to remove the residual ≈10 nm thick *PS* mask and the thin underlying brush layer efficiently. The transferred silicon features without residual mask layer are depicted in *figure A.5 b)*. The full pitch of the features in the images seems to be larger than the actual 23.4 nm. This may be because the SEM image been taken from a sample with self-assembly in finger print pattern and the imaged features do not run perfectly perpendicular to the cleavage.

Changes in the patterning recipe to increase the maximum pattern transfer depth for the both previously discussed block copolymer materials have to tackle the principal limiting factor that precludes a deeper transfer. For this reason, possible improvements in the pattern transfer recipe for the 23.4 nm full pitch block copolymer have to aim for a reduction in lateral etch velocity. A way to do so could be to increase the forward bias and/or the C_4F_8 ratio in the gas mixture. The principal limiting factor in the pattern transfer of the 30 nm full pitch block copolymer is, in turn, the mask wear. Increasing the forward bias is therefore not recommended, because this would enhance the acceleration of charged particles towards the substrate and result in increased mask wear. An alternative may be a slight reduction in C_4F_8, which increases both lateral and vertical etch velocity.

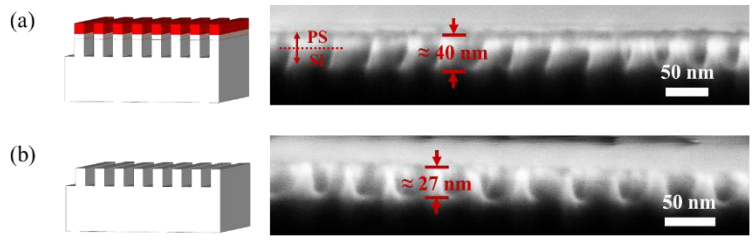

Figure A.5: Pattern transfer of a 22 nm pitch block copolymer. a) SEM cross section, 2° inclination after pattern transfer, with etch mask, b) SEM cross section, 2° inclination after silicon etching, without etch mask

Based on this analysis, we conclude this section with the insight that it is possible to conduct a pattern transfer of block copolymer features using *PS* as an etch mask. Due to the limited resistance of the mask towards physical etch mechanisms, a more resistant mask would, however, be desirable.

A.3.2 Pattern transfer to silicon using infiltrated PMMA as etch mask

A method to increase the etch resistivity by a factor of up to 37 [16] is sequential infiltration synthesis. Sequential infiltration synthesis is a way to infiltrate the *PMMA* domain of the block copolymer with an alumina complex. This forms an organic-inorganic hybrid material with high resistance to etch processes. A reason for the selectivity of the mechanism (e.g. the reason why *PS* is not infiltrated, but *PMMA* is) is the chemisorption of *TMA* to the *OH-groups* in *PMMA* [25]. According to this theory, *PS* is not infiltrated due to the absence of *OH-groups*. A SIS process consists of various repetition cycles consisting of an ALD of *TMA* and a following H_2O exposition. The exact processes taking place on the molecular basis are complex [15,26,27] and go beyond the scope of this thesis.

After the SIS process, the non-infiltrated *PS* domain is removed by an oxygen plasma for 10 minutes at 500 W. The material that has been used for the results presented in this section is a 67.1 $^{kg}/_{mol}$ molecular weight *PS-b-PMMA* block copolymer consisting of 71 wt% *PS* and 29 wt% *PMMA*. This block copolymer self-assembles in cylindrical domains with a pitch of 35 nm and *PMMA* features with a nominal diameter of 17 nm. The self-assembly of the block copolymers, the sequential infiltration synthesis and the removal of the residual *PS* of the samples shown in this section have been conducted by collaborators from CEA Leti and IMM-CNR.

The conditions used to transfer the structures into silicon are summarized in *table A.4* below. Sequential infiltration synthesis is a way to increase the resistance of the etch mask as a result of the addition of Al_2O_3, which represents a solution for the first problem

encountered during for the use of *PS* as etch mask, as has been found in the previous section. In addition to that, we increase the substrate bias from 10 W to 20 W compared with etching process using *PS* masks to reduce lateral etching, and raise the relative fraction of C_4F_8 in the gas flow from 43 % to 60 %.

Source power	Chuck power	Gas flows		Process pressure	Etch time
		SF_6	C_4F_8		
1200 W	20 W	20 sccm	30 sccm	2 Pa	30-45 s

Table A.4: Process conditions of pattern transfer using an infiltrated PMMA block of a 23.4 nm full pitch lamellar block copolymer as etch mask.

The SEM image depicted in *figure A.6 a)-c)* shows the evolution of the features as a function of etching time by the application of said etching process. The images are labeled with the process time. We notice that the increased C_4F_8 flow has contributed to a reduced etch velocity. While the process with 15 sccm C_4F_8 and 20 sccm SF_6 yields an etch rate in the range of 126 nm/min, we observe an about 25 % reduced etch rate upon increasing the C_4F_8-flux to 30 sccm. The exact determination of the etch rate is, however, complicated due to the relatively small process window of both processes.

The feature height after 30 s etching is 42 nm (including the etch mask), while lateral etching at that point has not yet led to substantial thinning of the features (see *figure A.6 b)*). After 45 s seconds, we measure a feature height of 76 nm (including the mask), while the features have become notably thinner (see *figure A.6 c)*). This may be due to two reasons. At one hand, lateral etching cannot be completely suppressed by the increase of forward power and C_4F_8-ratio. As we see in *figure A.6 a)*, the mask has a semi-spherical shape, which means that mask failure first occurs at the border of the infiltrated dots. It is conceivable that the reduced pillar width is also due to beginning mask failure on the edges of the infiltrated dots.

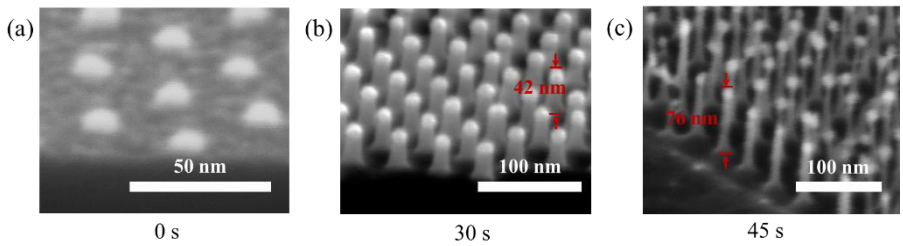

Figure A.6: Evolution of pillar aspect as a function of the etching time.

A.4 Conclusions

We present solutions for the transfer of templates defined by the self-assembly of block copolymers into silicon. Herein, we develop concrete recipes for the removal of the *PMMA* domain of the block copolymer and the subsequent transfer into silicon with the remaining *PS* block as an etch mask. We demonstrate the transfer of a lamellar block copolymer structure with 11 nm wide features with an etch depth of 38 nm. The main limiting factors precluding larger etch depths are the mask erosion and the lateral etching of the features. This problem can be minimized by using SIS, which strengthens the mask and reduces wearing. The increase of both forward bias and C_4F_8 concentration in the gas mixture has been demonstrated to yield the desired effect of lower lateral etching and contributed to a notable increase in the maximum vertical etch depth.

A.5 References

[1] Tsai H, Pitera J W, Miyazoe H, Bangsaruntip S, Engelmann S U, Liu C C, Cheng J Y, Bucchignano J J, Klaus D P, Joseph E A, Sanders D P, Colburn M E and Guillorn M A 2014 Two-dimensional pattern formation using graphoepitaxy of PS-b-PMMA block copolymers for advanced FinFET device and circuit fabrication *ACS Nano* **8** 5227–32

[2] Griffiths R A, Williams A, Oakland C, Roberts J, Vijayaraghavan A and Thomson T 2013 Directed self-assembly of block copolymers for use in bit patterned media fabrication *J. Phys. D. Appl. Phys.* **46** 1–29

[3] Kruse J E, Lymperakis L, Eftychis S, Adikimenakis A, Doundoulakis G, Tsagaraki K, Androulidaki M, Olziersky A, Dimitrakis P, Ioannou-Sougleridis V, Normand P, Koukoula T, Kehagias T, Komninou P, Konstantinidis G and Georgakilas A 2016 Selective-area growth of GaN nanowires on SiO2-masked Si (111) substrates by molecular beam epitaxy *J. Appl. Phys.* **119** 224305-1–10

[4] Sarrazin A, Pimenta-Barros P, Posseme N, Barnola S, Gharbi A, Argoud M, Tiron R and Cardinaud C 2015 PMMA removal selectivity to PS using dry etch approach for sub-10nm node applications *Proc. SPIE* **9782** 97820G1-11

[5] Thurn-Albrecht B T, Steiner R, Derouchey J, Stafford C M, Huang E, Bal M, Tuominen M, Hawker C J and Russell T P 2000 Nanoscopic Templates from Oriented Block Copolymer Films *Adv. Mater.* **12** 787–91

[6] Bartnik H, Fiedorowicz A, Jarocki R, Kostecki R J and Szczurek M 2010 PMMA and FEP surface modifications induced with EUV pulses in two selected wavelength ranges *Appl. Phys. A* **98** 61–5

[7] Sun Y, Wang C and Liou J 2016 Tuning polymer-surface chemistries and interfacial interactions with UV irradiated polystyrene chains to control domain

orientations in thin films of PS- b -PMMA *Soft Matter* **12** 2923–31

[8] Thurn-Albrecht T, Steiner R, DeRouchey J, Stafford C M, Huang E, Bal M, Tuominen M, Hawker C J and Russell T P 2000 Nanoscopic templates from oriented block copolymer films *Adv. Mater.* **12** 787–91

[9] Chavez K L and Hess D W 2003 Removal of Resist Materials Using Acetic Acid *J. Electrochem. Soc.* **150** G284–91

[10] Liu C, Nealey P F, Ting Y and Wendt A E 2007 Pattern transfer using poly(styrene-block-methyl methacrylate) copolymer films and reactive ion etching *J. Vac. Sci. Technol. B* **25** 1963–8

[11] Teik B, Tahara S, Parnell D, Rincon P A, Gronheid R, Marneffe J De, Xu K, Nishimura E and Boullart W 2014 Microelectronic Engineering 28 nm pitch of line / space pattern transfer into silicon substrates with chemo-epitaxy Directed Self-Assembly (DSA) process flow *Microelectron. Eng.* **123** 180–6

[12] Yamamoto H, Imamura T, Omura M, Sakai I and Hayashi H 2014 Selective etch of poly (methyl methacrylate) in block copolymer based on control of ion energy and design of gas chemistry for directed self assembly lithography *Jpn. J. Appl. Phys.* **53** 03DD03-1-4

[13] Farrell R A, Petkov N, Shaw M T, Djara V, Holmes J D and Morris M A 2010 Monitoring PMMA elimination by reactive ion etching from a lamellar PS-b-PMMA thin film by ex situ TEM methods *Macromolecules* **43** 8651–5

[14] Tseng Y, Peng Q, Ocola L E, Elam W and Darling S B 2011 Enhanced Block Copolymer Lithography Using Sequential Infiltration Synthesis *J. Phys. Chem. C* **115** 17725–9

[15] Peng Q, Tseng Y C, Darling S B and Elam J W 2011 A route to nanoscopic materials via sequential infiltration synthesis on block copolymer templates *ACS Nano* **5** 4600–6

[16] Elam J W, Biswas M, Darling S, Yanguas-Gil A, Emery J D, Martinson A B F, Nealey P F, Segal-Peretz T, Peng Q, Winterstein J, Liddle J A and Tseng Y-C 2015 New Insights into Sequential Infiltration Synthesis *ECS Trans.* **69** 147–57

[17] Ruiz R, Wan L, Lille J, Patel K C, Dobisz E, Johnston D E, Kisslinger K and Black C T 2012 Image quality and pattern transfer in directed self assembly with block-selective atomic layer deposition *J. Vac. Sci. Technol. B* **30** 06F202-1-6

[18] Henry M D 2010 *ICP etching of silicon for micro and nanodevices (PhD Thesis)* (California Institute of Technology)

[19] Kyoung Ryu Y, Aitor Postigo P, Garcia F and Garcia R 2014 Fabrication of sub-12 nm thick silicon nanowires by processing scanning probe lithography masks *Appl. Phys. Lett.* **104** 223112-1–4

[20] Stoffels W W, Stoffels E and Tachibana K 1998 Polymerization of fluorocarbons in reactive ion etching plasmas *J. Vac. Sci. Technol. A Vacuum, Surfaces, Film.*

16 87–95

[21] Borah D, Shaw M T, Rasappa S, Farrell R a, O'Mahony C, Faulkner C M, Bosea M, Gleeson P, Holmes J D and Morris M a 2011 Plasma etch technologies for the development of ultra-small feature size transistor devices *J. Phys. D. Appl. Phys.* **44** 174012-1–12

[22] Bates C 2013 *Advanced Materials for Block Copolymer Lithography (PhD Thesis)* (University of Texaas at Austin)

[23] IEEE 2016 *International Roadmap for Devices and Systems 2016 Edition*

[24] Helfand E and Tagami Y 1971 Theory of the interface between immiscible polymers *Polym. Lett.* **9** 741–6

[25] Evangelio Araujo L 2017 *Directed self-assembly of block copolymers on chemically nano-patterned surfaces (PhD thesis)* (Universitat Autònoma de Barcelona)

[26] Biswas M, Libera J A and Darling S B 2014 New Insight into the Mechanism of Sequential In fi ltration Synthesis from Infrared Spectroscopy *Chem. Mater.* **26** 6135–41

[27] Tseng Y C, Mane A U, Elam J W and Darling S B 2012 Enhanced lithographic imaging layer meets semiconductor manufacturing specification a decade early *Adv. Mater.* **24** 2608–13

List of abbreviations

AFM	Atomic Force Microscopy
AI	Artificial Intelligence
ALD	Atomic Layer Deposition
BCP	Block Copolymer
CLL	Closed-Loop Lithography
DSA	Directed Self-Assembly
DUV	Deep-Ultraviolet Lithography
e-beam DW	Electron Beam Direct Writing
EUV	Extreme- Ultraviolet
EUV-IL	Extreme- Ultraviolet Interference Lithography
FEBIP	Focused Electron Beam Induced Processing
FET	Field Effect Transistor
FP7	Seventh Framework Program
FWHM	Full-Width at Half Maximum
GISAXS	Grazing-Incidence Small-Angle X-Ray-Scattering
GP	Guiding Pattern
GTR	Grating Truncation Rod
H2020	Horizon 2020
HSQ	Hydrogen Silsesquioxane
HVM	High-Volume Manufacturing
ICP	Inductively Coupled Plasma
IEEE	Institute of Electrical and Electronic Engineers
IMDS	Inter-Materials Dividing Surface
Ions4SET	Ion-irradiation-induced Si Nanodot Self-Assembly for Hybrid SET-CMOS Technology
IoT	Internet of Things
IRDS	International Roadmap of Devices and Systems
ITRS	International Technology Roadmap for Semiconductors
JRA	Joint Research Activity
LAO	Local Anodic Oxidation
LER	Line-Edge-Roughness
LWR	Line-Width-Roughness
m-AFM	Mechanical Atomic Force Microscopy
MIBK	Methyl Isobutyl Ketone
ML2	Maskless Lithography
MMA	Methyl Methacrylate
NFFA	Nanscience Foundries and Fine Analysis

NGL	Next-Generation Lithography
NIL	Nanoimprint Lithography
PDI	Polydispersity Index
PGMEA	Propylene Glycol Monomethyle Ether Acetate
PMMA	Poly(Methyl Methacrylate)
PPA	Poly(Phthalaldehyde)
PS	Polystyrene
PS-b-PLA	Polystyrene-block-polylactic acid
PS-b-PMMA	Polystyrene-block- Poly(Methyl Methacrylate)
PS-OH	Oxygen-terminated Polystyrene
PS-r-PMMA	Polystyrene-random- Poly(Methyl Methacrylate)
RIE	Reactive Ion Etching
RT	Room Temperature
SAXS	Small-Angle X-Ray Scattering
SEM	Scanning Electron Microscopy
SIS	Sequential Infiltration Synthesis
SNM	Single Nanometer Manufacturing
SNR	Signal-to-Noise-Ratio
SPL	Scanning Probe Lithography
TMA	Trimethyl Aluminum
t-SPL	Thermal Scanning Probe Lithography
UV-NIL	Ultraviolet Nanoimprint Lithography

Scientific contributions

Publications in scientific journals

1. Gottlieb S, Lorenzoni M, Evangelio L, Fernández-Regúlez M, Ryu Y K, Rawlings C, Spieser M, Knoll A W and Perez-Murano F 2017 Thermal scanning probe lithography for the directed self-assembly of block copolymers *Nanotechnology* **28** 1–9

2. Gottlieb S, Kazazis D, Mochi I, Evangelio L, Fernández-Regúlez M, Ekinci Y and Perez-Murano F 2018 Nano-confinement of block copolymers in high-accuracy topographical guiding patterns: Modelling the emergence of defectivity due to incommensurability *Soft Matter* **14** 6799-808

3. Gottlieb S, Rösner B, Evangelio L, Fernández-Regúlez M, Nogales A, García-Gutiérrez M-C, Keller T F, Fraxedas J, Ezquerra T A, David C and Perez-Murano F Directed self-assembly of block copolymers in sub-10 nm topographical guiding patterns *Accepted for publication in Molecular Systems Design & Engineering*

Submitted articles and articles in preparation

4. Gottlieb S, Evangelio L, Lorenzoni M, Fernández-Regúlez M and Perez-Murano F Using grain boundaries to direct the self-assembly of block copolymer thin films *In preparation*

5. Gottlieb S, Ryu Cho Y K, Lorenzoni M, Evangelio L, Fernández-Regúlez M, Rawlings C, Spieser M, Knoll A W and Perez-Murano F Sub-10 nm resolution thermal imaging of block copolymers *In preparation*

Contributions to conferences and presentations

6. Conde-Rubio A, Evangelio L and Gottlieb S 2016 A brief introduction to the nanoworld (Oral) *Jorn. d'Investigadors Predoctorals Interdiscip. Barcelona, Spain*

7. Gottlieb S, Evangelio L, Lorenzoni M, Fernández-Regúlez M, Ryu Cho Y K, Knoll A W and Pérez-Murano F 2016 The fabrication of high resolution guiding patterns for the directed self-assembly of block co-polymers (Oral) *2nd Sci. Meet. BNC-b Students, Barcelona, Spain*

8. Gottlieb S, Lorenzoni M, Evangelio L, Fernandez-Regulez M, Ryu Cho Y K, Rawlings C, Spieser M, Knoll A W and Perez-Murano F 2017 The use of thermal scanning probe lithography for the directed self-assembly of block copolymers (Poster) *SPIE Adv. Lithogr. San Jose, USA*

9. Gottlieb S, Kazazis D, Mochi I, Evangelio L, Fernandez-Regulez M, Ekinci Y and Perez-Murano F 2017 Directed self-assembly of single block copolymer lines in graphoepitaxial guiding patterns made by EUV-IL (Poster) *SPIE Adv. Lithogr. San Jose, USA*

10. Gottlieb S, Lorenzoni M, Evangelio L, Fernández-Regúlez M, Ryu Cho Y K, Rawlings C, Spieser M, Knoll A W and Perez-Murano F 2017 The use of t-SPL for the directed self-assembly of block copolymers (Oral) *4th Therm. Probe Work. Zurich, Switz.*

11. Gottlieb S, Lorenzoni M, Evangelio L, Fernández-Regúlez M, Ryu Cho Y K, Rawlings C, Spieser M, Kazazis D, Ekinci Y, Knoll A W and Perez-Murano F 2017 Guiding Pattern Options to Direct the Self-Assembly of Block Copolymers (Oral) *3rd Sci. Meet. BNC-b Students, Barcelona, Spain*

12. Gottlieb S 2017 Breaking the Wall of Gordon Moore (Oral) *Falling Walls Lab, Barcelona, Spain*

13. Gottlieb S, Evangelio L, Lorenzoni M, Fernández-Regúlez M and Perez-Murano F 2017 Directed self-assembly of block copolymer thin films by the controlled introduction of grain boundaries (Poster) *MNE, Braga, Port.*

14. Grazyk M, Cattoni A, Rösner B, Löfstand A, Seniutinas G, Kvennefors A, Mailly D, David C, Gottlieb S, Perez-Murano F and Maximov I 2017 Ultra-high resolution nanoimprint stamps: optimal fabrication techniques (Oral) *MNE, Braga, Port.*

15. Gottlieb S, Kazazis D, Rösner B, Mochi I, Evangelio L, Fernández-Regúlez M, David C, Ekinci Y and Perez-Murano F 2017 The fabrication of high-resolution topographical guiding patterns for the directed self-assembly of block copolymers (Oral) *MNE, Braga, Port.*

16. Grazyk M, Cattoni A, Rösner B, Löfstand A, Seniutinas G, Kvennefors A, Mailly D, David C, Gottlieb S, Perez-Murano F and Maximov I 2017 Ultra-high resolution nanoimprint stamps: optimal fabrication techniques (Poster) *MNE, Braga, Port.*

17. Lorenzoni M, Perez-Murano F, Evangelio L, Gottlieb S and Llobet J 2017 Atomic force microscopy as a tool for nanoscience, top-down fabrication and nanomechanical characterization (Oral) *MNE, Braga, Port.*

18. Fraxedas J, Evangelio L, Fernández-Regúlez M, Gottlieb S, Rius G, Perez-Murano F, Amenitsch H, Gutiérrez E, Nogales A, García-Gutiérrez M-C,

Ezquerra T A 2017 Self-assembly of block copolymer thin films as revealed by GISAXS (Oral) *VII AUSE Congress / III ALBA User's Meeting, Madrid, Spain*

19. Gharbi A, Pimenta-Barros P, Saouaf O, Navarro C, Nicolet C, Cayrefourcq I, Perego M, Gottlieb S, Amat E, Fernández-Regúlez M, Perez-Murano F and Tiron R 2018 Pillars fabrication by DSA lithography: material and process options (Oral) *SPIE Adv. Lithogr. San Jose, USA*

20. Gottlieb S, Rösner B, Evangelio L, Fernández-Regúlez M, Nogales A, García-Gutiérrez M-C, Keller T F, Ezquerra T A, David C and Perez-Murano F 2018 Self-assembly morphology of block copolymers in sub-10 nm wide topographical guiding patterns (Poster) *EMRS Spring Meet. Strasbourg, Fr.*

21. Fernández-Regúlez M, Evangelio L, Pinto-Gómez C, Gottlieb S, Bausells J and Perez-Murano F 2018 Nanowire device fabrication by optical lithography and directed self-assembly of block copolymers (Poster) *EMRS Spring Meet. Strasbourg, Fr.*

22. Fernández-Regúlez M, Evangelio L, Gottlieb S, Rius G, Fraxedas J, Perez-Murano F, Amenitsch H, Gutiérrez E, Nogales A, García-Gutiérrez M-C and Ezquerra T A 2018 In situ real-time characterization of block copolymer self-assembly processes by GISAXS (Oral) *EMRS Spring Meet. Strasbourg, Fr.*

23. Gottlieb S, Kazazis D, Mochi I, Evangelio L, Fernández-Regúlez M, Ekinci Y and Perez-Murano F 2018 Studying the confinement of block copolymers in topographical guiding patterns fabricated by EUV-IL with nanometer precision (Oral) *EMRS Spring Meet. Strasbourg, Fr.*

24. Gottlieb S, Ryu Cho Y K, Lorenzoni M, Evangelio L, Fernández-Regúlez M, Rawlings C, Spieser M, Knoll A W and Perez-Murano F 2018 Thermal imaging of block copolymers with sub-10 nm resolution (Poster) *EMRS Spring Meet. Strasbourg, Fr.*

Acknowledgements

Writing this PhD thesis in the IMB-CNM was a very pleasant and gratifying experience. Obviously, it would have been impossible to obtain results without the help of a many people. I would like to thank at this point each and everybody who has helped me in one way or the other, whether it was in my private life or in the professional environment.

In the very beginning I would like to express my sincere gratitude to my supervisor Francesc Perez-Murano, whom I cannot thank enough for his advice, his calmness, all the doors he has opened for me and the tireless effort he has put into coaching me. I will not forget all the visible and invisible things he has done for me. In the very improbable case that I decide to write another PhD thesis at some point in my life, I sincerely hope you would supervise me again.

I extend my thanks to the past and present members of office E1-12 (Albert, Angelos, Christian, Genís, Javi, Jordi, Laura, Marcos, Marta, Olga) and those members of the NanoNEMS group that were not lucky enough to have a desk in our office (Esteve, Gemma, Joan and Matteo). You have played an important role in my personal well-being during the entire time I spent in the institute. Moreover, I am proud of having had the opportunity to serve you as OCC (Official Coffee Coordinator).

Thank you to the football team “Amigos de Cristobal y Jesus”, that I was allowed to form part of. It was a pleasure!

I would also like to express my gratitude to the personnel of the CNM Clean Room, in particular to the staff of the Nano Area, the RIE Area and the Microsystems Lab, who were always prepared to support my work whenever and wherever they could.

Furthermore, I would like to thank Armin Knoll and the members of his group, who hosted me excellently during my two scientifically and personally very fruitful stays at IBM Research Zurich. I would like to thank them for the training I received on the thermal scanning probe tool and acknowledge the finite element simulations they have done to model the resolution of the thermal conductivity measurements.

I owe all the participants of the NFFA JRA 2, and particularly the members of the Laboratory of Micro and Nanolaboratory at PSI a debt of gratitude. Thank you for the great collaboration. Particularly, I would like to acknowledge Benedikt Rösner for the e-beam exposures, Dimitrios Kazazis for EUV-IL exposures and Iacopo Mochi for the LWR/LER analysis.

Moreover, I would like to thank all the members of the Soft and Polymeric Matter Group at the IEM that I spent various nights together with in synchrotrons in Germany, Spain and Italy, and Heinz Amenitsch for the scientifically interesting discussions.

Last but not least, this work would, of course, not have been possible without the help of my family. My thanks go to my parents for their confidence and their encouragement during the time of the PhD, and especially towards the end of the thesis, but also during my whole life, when they have always been there for me. I would especially like to express my gratitude to María who has always supported me and helped me to overcome the daily difficulties with her positivity.

A great part of the presented research has been funded by the European projects NFFA under grant agreement no. 654360, SNM under grant agreement no. 318804 and IONS4SET under grant agreement no. 688072, for which I would like to acknowledge the European Commission. This research has, furthermore, been funded by the Spanish MINECO project Nanointegra, grant reference TEC2015-69864-R.

CSIC
Consejo Superior de Investigaciones Científicas

UAB
Universitat Autònoma
de Barcelona

CNM
Centro Nacional de Microelectrónica
IMSE